

# Measurement of quartic boson couplings at the international linear collider and study of novel particle flow algorithms

Dissertation  
zur Erlangung des Doktorgrades  
des Fachbereichs Physik  
der Universität Hamburg

vorgelegt von  
Predrag Krstonosic

Hamburg  
Februar 2008

Gutachter der Dissertation : Prof. Dr. R.-D. Heuer  
Prof. Dr. P. Schleper

Gutachter der Disputation : Prof. Dr. R.-D. Heuer  
Prof. Dr. P. Schleper

Datum der Disputation : 22.02.2008

Vorsitzender des Prüfungsausschusses : Dr. K. Petermann

Vorsitzender des Promotionsausschusses : Prof. Dr. G. Huber

MIN-Dekan des Department Physik : Prof. Dr. A. Frühwald

*“Reality has to take precedence over Public Relations, for Nature cannot be fooled!”*

Richard Feynman

*“We don’t want most beautiful and most abstract software, but one that works!”*

Ties Behnke

## Acknowledgments

First of all I want to thank to Klaus Mönig for providing plesent atmosphere from my first day in the Deutschen Electronen-Synchrotron (DESY) and for years of fruitfull work together.

Also, I would like to thank Wolfgang Kilian and Jurgen Reuter for relieble guidance through the dungines of theory. Special thank to Vasily Morgunov for refreshing and usefull discussions that have deepen my insigt in many subjects.

Thank to all the unmentioned peopele that have succeded to improove my mood on coloudy days. At the end my sincere condolence to all those forced to read this text, since I'm much better at calculating then writing.

## Abstract

In the absence of the Standard Model Higgs boson the interaction among the gauge bosons becomes strong at high energies ( $\sim 1\text{TeV}$ ) and influences couplings between them. Trilinear and quartic gauge boson vertices are characterized by set of couplings that are expected to deviate from Standard Model at energies significantly lower than the energy scale of New Physics. Estimation of the precision with which we can measure quartic couplings at International Linear Collider (ILC) is one of two topics covered by this thesis. There are several measurement scenarios for quartic couplings. One that we have chosen is weak boson scattering. Since taking of the real data is, unfortunately, still far in the future running options for the machine were also investigated with their impact on the results. Analysis was done in model independent way and precision limits were extracted. Interpretation of the results in terms of possible scenarios beyond Standard Model is then performed by combining accumulated knowledge about all signal processes. One of the key requirements for achieving the results of the measurement in the form that is presented is to reach the detector performance goals. This is possible only with “Particle Flow” reconstruction approach. Performance limit of such approach and various contribution to it will be discussed in detail. Novel reconstruction algorithm for photon reconstruction is developed, and performance comparison of such concept with more traditional approaches is done.

## Zusammenfassung

Ohne das Higgs Boson des Standardmodells wird die Wechselwirkung der Eichbosonen bei Energien um 1 TeV stark und beeinflusst die Kopplung zwischen ihnen. Trilineare und biquadratische Eichbosonvertices werden durch einen Satz Kopplungen charakterisiert. Von diesem wird erwartet, dass er von dem des Standardmodells, bei Energien die deutlich unterhalb der Skala neuer Physik liegen, abweicht. Eines der beiden Themen dieser Doktorarbeit ist die Abschätzung der Präzision, mit der biquadratische Kopplungen am Internationalen Linearbeschleuniger (ILC) gemessen werden können. Es gibt mehrere mögliche Szenarien, in deren Rahmen biquadratische Kopplungen gemessen werden können. Es wurde das Szenario mit schwacher Boson Streuung gewählt. Da die tatsächliche Datennahme noch weit in der Zukunft liegt, wird auch der Einfluss verschiedener Betriebsmöglichkeiten des Beschleunigers auf dieses Ergebnis getestet. Die Analyse wurde Modellunabhängig ausgeführt, und die Grenzen der Präzision wurden bestimmt. Bei der Deutung der Ergebnisse in Hinblick auf mögliche Physik jenseits des Standardmodells wurden alle Signalprozesse berücksichtigt. Um die Messergebnisse in der dargestellten Form zu erreichen, muss die angestrebte Detektorleistung erfüllt werden. Dies ist nur unter Verwendung des Particle Flow Ansatzes machbar. Die Grenzen eines solchen Ansatzes, sowie verschiedene Einfüsse auf diese, werden im Detail untersucht. Ein neuer Rekonstruktionsalgorithmus für Photonen wird entwickelt und mit konventionelleren Ansätzen verglichen.



# Contents

<b>1</b>	<b>Introduction</b>	<b>1</b>
1.0.1	Outline of the theses . . . . .	2
<b>2</b>	<b>International Linear Collider (ILC)</b>	<b>3</b>
2.0.2	Accelerator . . . . .	3
2.1	Detector . . . . .	4
2.1.1	Tracking system . . . . .	5
2.1.2	Electromagnetic calorimeter . . . . .	9
2.1.3	Hadronic calorimeter . . . . .	10
2.1.4	Muon system . . . . .	11
2.1.5	Forward region . . . . .	11
2.1.6	Detector design evolution . . . . .	12
<b>3</b>	<b>Quartic couplings</b>	<b>15</b>
3.1	Standard Model . . . . .	15
3.1.1	Electroweak sector . . . . .	19
3.1.2	Symmetry breaking sector . . . . .	21
3.2	Effective Lagrangian . . . . .	24
3.3	Measurement strategy . . . . .	26
3.4	Resonances . . . . .	28
3.4.1	Scalar singlet . . . . .	28
3.4.2	Scalar triplet . . . . .	29
3.4.3	Scalar quintet . . . . .	29
3.4.4	Vector singlet . . . . .	30
3.4.5	Vector triplet . . . . .	31
3.4.6	Tensor singlet . . . . .	32
3.4.7	Tensor triplet . . . . .	32
3.4.8	Tensor quintet . . . . .	33
<b>4</b>	<b>Analysis and Results</b>	<b>35</b>
4.1	Direct measurement of quartic couplings . . . . .	35
4.1.1	Processes . . . . .	35
4.1.2	Observable . . . . .	36
4.2	Event selection . . . . .	37
4.2.1	Jet pairing . . . . .	37
4.2.2	B tagging . . . . .	41
4.2.3	Forward region . . . . .	42
4.2.4	Overview of selection criteria . . . . .	44
4.3	Quartic couplings extraction . . . . .	48

4.4	Quartic coupling limits . . . . .	51
4.4.1	Combined results . . . . .	52
4.4.2	Running options . . . . .	54
4.5	Model dependent limits on new physics . . . . .	56
4.5.1	Combination of measurements . . . . .	57
4.5.2	Mass limit extraction . . . . .	57
4.6	Mass limit results . . . . .	58
4.6.1	Scalar singlet . . . . .	58
4.6.2	Scalar triplet . . . . .	61
4.6.3	Scalar quintet . . . . .	62
4.6.4	Vector singlet . . . . .	65
4.6.5	Vector triplet . . . . .	66
4.6.6	Tensor singlet . . . . .	70
4.6.7	Tensor triplet . . . . .	72
4.6.8	Tensor quintet . . . . .	73
4.7	Summary . . . . .	77
<b>5</b>	<b>Particle flow</b>	<b>79</b>
5.1	The concept of particle flow . . . . .	79
5.1.1	Hardware parameters and Eflow reaches of LEP experiments . . . . .	81
5.1.2	Jet energy resolution . . . . .	82
5.1.3	Contributions to the jet energy resolution . . . . .	84
5.2	Magnetic field effects . . . . .	87
5.2.1	Effects on calibration . . . . .	87
5.2.2	Effects on shower size . . . . .	89
5.2.3	Effects on full reconstruction . . . . .	91
5.3	Conclusion . . . . .	93
<b>6</b>	<b>Particle Reconstruction in ILC Detector</b>	<b>95</b>
6.1	Approach to Reconstruction . . . . .	95
6.1.1	Reconstruction framework . . . . .	95
6.1.2	Requirements for the electromagnetic shower reconstruction . . . . .	96
6.2	Electromagnetic Shower . . . . .	98
6.2.1	Longitudinal development . . . . .	99
6.2.2	Transverse development . . . . .	100
6.3	Photon finding algorithm . . . . .	102
6.3.1	Algorithm steps . . . . .	102
6.3.2	Summary of steering parameters . . . . .	112
6.3.3	Algorithm performance . . . . .	113
6.3.4	Conclusion . . . . .	122
<b>7</b>	<b>Summary and conclusions</b>	<b>125</b>
<b>A</b>	<b>Theory addons</b>	<b>126</b>
A.0.5	groups . . . . .	127
A.0.6	Goldston theorem . . . . .	128
<b>B</b>	<b>Pflow factorization</b>	<b>130</b>

<b>C</b>	<b>Summary of the formulae for photon shower parameterization</b>	<b>133</b>
C.1	Homogeneous media . . . . .	133
C.1.1	Average longitudinal profiles . . . . .	133
C.1.2	Average radial profiles . . . . .	133
C.2	Sampling calorimeter . . . . .	134
C.2.1	Material and geometry parameters . . . . .	134
C.2.2	Average longitudinal profiles . . . . .	134
C.2.3	Average radial profiles . . . . .	134
	<b>Bibliography</b>	<b>134</b>



# Chapter 1

## Introduction

How it all began? All started on not so sunny day almost five years ago on the bus stop in front of the army base. I have accidentally <sup>1</sup> met acquaintance of my, physicist understandably, and we have started a small talk. Just by the way I was informed about possibility for a job at Institute for Nuclear Sciences Vinca in Belgrade. I have applied for the position and got it. The job implied leaving the real world of nuclear and medical physics and adjusting to the to be world of future and beyond experiments, discoveries and theories. It was in the beginning “cultural shock” seeing and listening to the people that are talking “fairy tails”. In mean while I have to some part also become a story teller but with, I hope, good dose of skepticism that should be noticeable through the theses. In the center of tail, we will tell, there is as high energy  $e^+e^-$  collider. Under the Olympic motto (“Faster, Higher, Stronger”), it should lead us to the new stage of particle physics beyond the present day theory ( Standard Model (SM)). Electrons and positrons will be *faster* then ever before, it will provide *higher* precision of the measurement and lead to the *stronger* constrains on the theory. Major objection to SM it is that the nature of mass, that is fundamental quantity in our system of units, is unknown. By *Deus ex machina* approach, solution for the masses within the theory is introduced and search for the holy grail of particle physics, Higgs particle, that this solution postulates has begun, so far without any success. In opinion on this subject one can aline himself with the believers expecting that the missing part will be observed, and non-believers that usually have interesting explanation of their own. As always when main hero becomes too arrogant and narcistic story could have a turnover and the nature will have its final word. We will try to follow the middle way starting with that what we know today and try to infer how our knowledge would be expanded by measurement making as few assumption as possible. Thus instead of rigid solution we can assume that the interactions that we observe are only low-energy approximations to the true mechanisms that work as some higher energy scale. This approach is formalized in the Effective Lagrangian - low energy expansion of the true theory. Since one knows the expected values for the parameters of the Effective Lagrangian in case of SM, any experimentally significant deviation from these values can give insight into underlying theory. One such subset of parameters are quartic couplings. There are several classes of physics processes in which such deviation could be observed. One chosen here is, so called, weak boson scattering. After measurement of the parameters one needs to make a consistent set of their values and then it is possible to discuss their meaning in terms of particular theory model. Trivially, but true, if you want to measure something you need the detector. All easy measurable things are already determined rather precisely and in order to make another step one needs to increase the precision even further. This puts rather strict constrains on

---

<sup>1</sup>if such things exist at all

the needed luminosity and detector performance. Detector performance goal can be reached with new reconstruction method called Particle Flow, that is at the same time detector design guideline. Understanding the limitations of the method and essential contributions to the overall performance is of great importance for the proper detector design and final physics output. As even the best car is worth nothing without gasoline, so is the excellent detector without matching reconstruction software. New detector concept requires development of new reconstruction methods that are of equal importance as underlying hardware. Unfortunately support for the two branches that will lead us to the goal was highly disproportional, leaning sometimes to the, false, conclusion “that will not work”. Part of this story will be thus dedicated to shattering this doubts. Since it is already rather late, lets start.

### 1.0.1 Outline of the theses

Theses has two, apparently, disconnected parts measurement of quartic coupling and evaluation and development of new reconstruction methods. It starts with introduction to the International Linear Collider (ILC), both accelerator and its detector in Chapter 2. Since detector used in the first part differs form the up to date design both detectors will be presented in parallel stressing their differences. In Chapter 3 we shortly remind reader about standard model as a gauge theory, introduce Effective Lagrangian, introduce quartic couplings. In the same chapter measurement strategy for the quartic couplings is presented as well as their relation to possible new resonances at TeV scale. In Chapter 4 we will cover analiss part in terms of event selection and correct interpretation of the results. Essential steps in data treatment are fully explained. Sensitivity limits for measurement are extracted and interpretation of the results is done in terms of to be resonances. In Chapters 5 Particle Flow approach is discussed in some detail with clarification of most common misunderstandings. Personal contribution to reaching the detector design performance in form of photon reconstruction algorithm is presented in Chapter 6 together with comparison of it’s performance with respect to other tools on the market. Finally, the results presented in this theses are summarized in Chapter 7. Any material that might be useful for understanding of the text and has not fitted on other place is in appendix.

## Chapter 2

# International Linear Collider (ILC)

It is hard to escape from the historical approach in the introduction to the project that spans over so many years, but we will try to restrict ourself to the time span during which this theses was done, for larger scope see [1]. During this time one was able to observe organization <sup>1</sup> of the global effort for the linear collider. Abrevation have changed from 3 letter ones to 4 and more and International Linear Collider Steering Committee (ILCSC) subgroup on parameters has made two documents about project scope, one in 2003 [2] and in 2006 [3]. On the bases of these two documents we can say the following. The ILC baseline is an  $e^+e^-$  collider that should be able to reach a center of mass energy of 500GeV, and allow physics measurements in the range of 200-500GeV. The Luminosity should be  $2 \times 10^{34} cm^{-2} s^{-1}$  at 500GeV and the electron beam polarization of at least 80% within whole energy range used for physics running. This would allow the collection of approximately  $\mathcal{L}_{eq} = 500 fb^{-1}$  in the first four years of running. Beam energy stability should be below  $10^{-3}$  level. There are tiny and not essential differences between the two documents. One of them is that in 2003, “Two interaction regions should be planned, with space and infrastructure for two experiments, with explanation. Two experiments are desired to allow independent measurement of critical parameters and to provide better use of the beams thereby maximizing physics output. At least one of them should allow crossing angle with  $\gamma\gamma$  interaction region”. That has changed to “The interaction region (IR) should allow for two experiments” with, interestingly, same explanation. Second is that “The maximum luminosity is not needed at the top energy (500GeV)...” , unfortunately without a reference, since this implies that one knows where the maximum is needed thus what physics scenario is realized in nature. All other possible parameters of the project are considered as options beyond baseline. Those are energy upgrade up to 1TeV, positron polarization at or above 50% as well as the running in the  $e^-e^-$  mode. On the bases of these requirements there is a design that is supposed to fulfill them explained in detail in ILC Reference Design Report [5]. We will just flash the accelerator with few remarks here and there and discuss detector in some detail, specially those elements that are of interest for quartic boson couplings analysis and reconstruction.

### 2.0.2 Accelerator

The accelerator is based on a superconducting RF cavities on the recommendation of International Technical Recommendation Panel (ITRP) [4]. The average accelerating gradient in cavities is supposed to be 31.5 MV/m. The current layout of the machine is in Fig.2.1. An electron source feeds the electron arm of the accelerator. A damping ring for electrons and

---

<sup>1</sup>reed biocratization

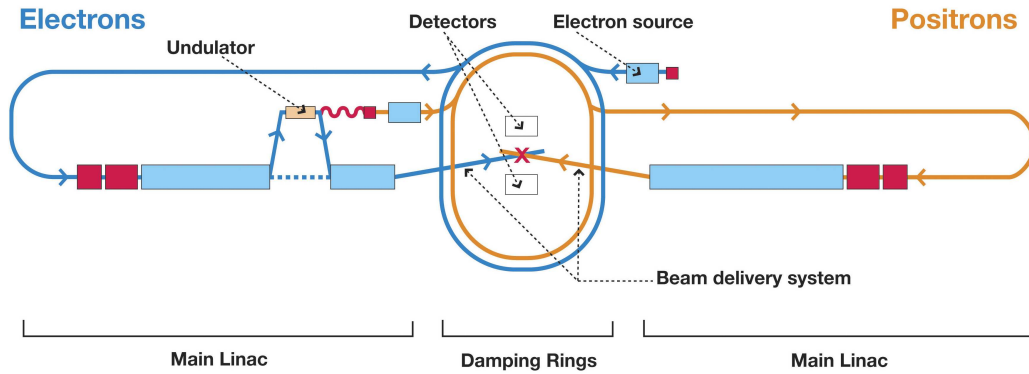


Figure 2.1: Layout of the ILC design.

positrons is placed centrally. The positrons source is undulator based and thus integrated in the electron arm of the main linac. One can note strange positioning of the detectors in the middle of the layout. This is due to the fact that the proposal contains two detectors<sup>2</sup> but only one beam delivery system and interaction point (IP). The detectors will have time sharing of the beam by positioning one or another at the IP (push-pull design). As indicated on the layout beams are not colliding head on but with the 14mrad crossing angle. Although sometimes neglected detail constructional and operating parameters of the accelerator will have a significant impact on the detector-measurement performance beyond usually considered parameters as center of mass energy and integrated luminosity. Due to this fact there is a nominal set of beam and IP parameters containing variables like repetition rate of beam pulses (5Hz), number of bunches per puls (2625), number of particles per bunch ( $2 \times 10^{10}$ ), average beam current (9.0mA), beam size at IP ( $639nm \times 5.7nm \times 300\mu m$ ) and so on, that are leading to the desired luminosity. In addition to the nominal set there are several alternative sets with parameters changed in a consistent way so that design luminosity is recovered. They are equivalent only in the resulting luminosity but affecting background and timing constrains on the detector. Only once a particular set is chosen it would be correct to discuss detector design but we will do so nevertheless. Just keep in mind that the layout of the innermost detectors will change with the beam parameters. Will this change be favorable for the physics measurement or not is an open issue.

## 2.1 Detector

With evolution of the TESLA [6] project to the ILC not only the accelerator suffered changes but also the design of the detector went through the diversification. Three regionally based detector concepts emerged. Although essentially designed on the same “Particle Flow” philosophy (see Chapter 5) designs differ in what particular sub-detector combination was considered favorable to reach the goal. Three designs are Global Large Detector GLD[11], Large Detector Concept LDC[8] and Silicon Detector SiD[10], an overview is also available in the detector part of the RDR[5]. In Table. 2.1 a comparison of major detector components in three detector proposals is shown.

All of them are trying to reach the detector design goals that are:

<sup>2</sup>for the moment

Table 2.1: Comparison of vital detector components in GLD, LDC and SiD.

	GLD	LDC	SiD
Main tracker	TPC/Si	TPC/Si	Si
N of points TPC	2000	200	-
N of Si points barrel	4	2	5
N of Si points endcap	7	7	4
ECAL	Scint.-W	Si-W	Si-W
total $X_0$	27	23	29
HCAL	Scint.-Fe	Scint.-Fe	RPC-W
total $\lambda$	5.8	4.6	4.0
Magnetic Field [T]	3	4	5
detector radius [cm]	720	600	645
detector half-length [cm]	750	620	589

- jet energy resolution  $\delta E/E = 30\% \sqrt{E}$  , needed for W and Z separation
- impact parameter resolution of  $5\mu m \oplus \frac{10\text{GeV}/c}{p \sin^{3/2}\theta} \mu m$  , needed for flavor tagging
- transverse momentum resolution of  $\delta(1/p_t) < 5 \times 10^{-5} (\text{GeV})^{-1}$  , needed for Higgs physics
- hermeticity down to 5mrad, for veto of the  $\gamma\gamma$  background and luminosity measurement

In order to achieve the detector performance needed all detectors must be inside the coil <sup>3</sup> that is limiting the detector size. So all proposed detectors have same the layout, from inside to outside vertex detector, main tracker, electromagnetic calorimeter (ECAL), and hadronic calorimeter (HCAL). We will thus explain only the LDC detector in detail. The evolution of the design from the TESLA TDR detector [6, 7] (in Figure.2.2) to the LDC detector [8, 9](in Figure.2.3) is of particular interest since the analysis (in Chapter 4) was done for the TESLA detector design. For this reason we will put special emphasis on the differences between the two detectors.

### 2.1.1 Tracking system

The tracking system consist of five sub-detectors (Fig.2.4): a time projecting chamber (TPC), a micro-vertex detector (VTX), two additional detectors that support tracking between VTX and TPC (silicon intermediate tracker SIT, and forward tracking discs FTD), and finally a tracking detector behind TPC (endplate) called forward chamber FCH (different name for the same detector in LDC design is endcap tracking device ETD).

The vertex detector consist of 5 cylinders of silicon pixel sensors positioned from 16 to 60mm from the beam axes and is responsible for excellent b and c tagging capability of the detector with polar angle coverage till  $|\cos\theta| = 0.9$ . (with three innermost layers covering up to  $|\cos\theta| = 0.96$ ). It is expected to provide independent track elements. The already mentioned impact parameter resolution implies single point resolution of not more then  $3\mu m$ . Additionally constrains on the design are: minimization of material budget (0.1% of  $X_0$  per layer) to minimize multiple scattering and possible interactions before the calorimeter, radiation hardness to the electromagnetic and neutron background, high readout speed , good signal to noise ratio, possible operation without too robust cooling, tolerance to the beam

<sup>3</sup>except muon system understandably

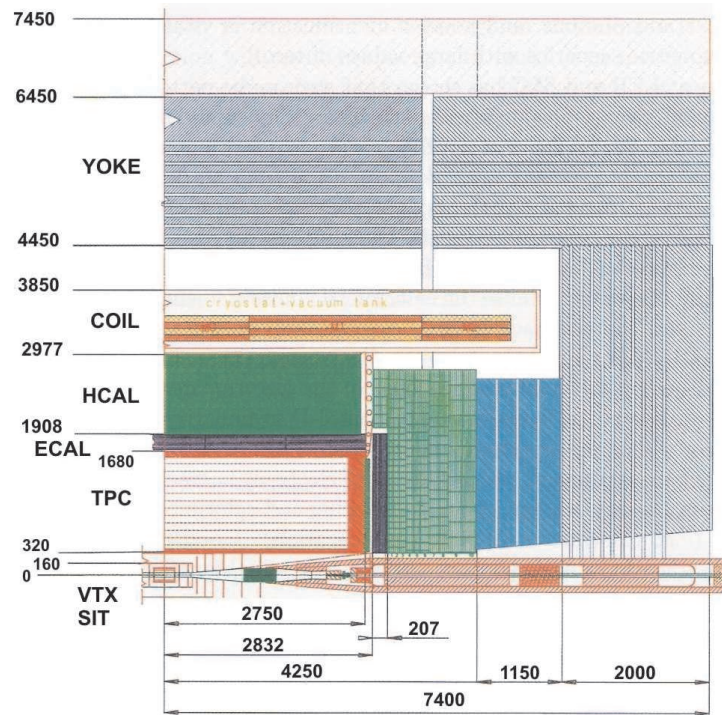


Figure 2.2: Quadrant view of the TESLA detector, dimensions are in mm.

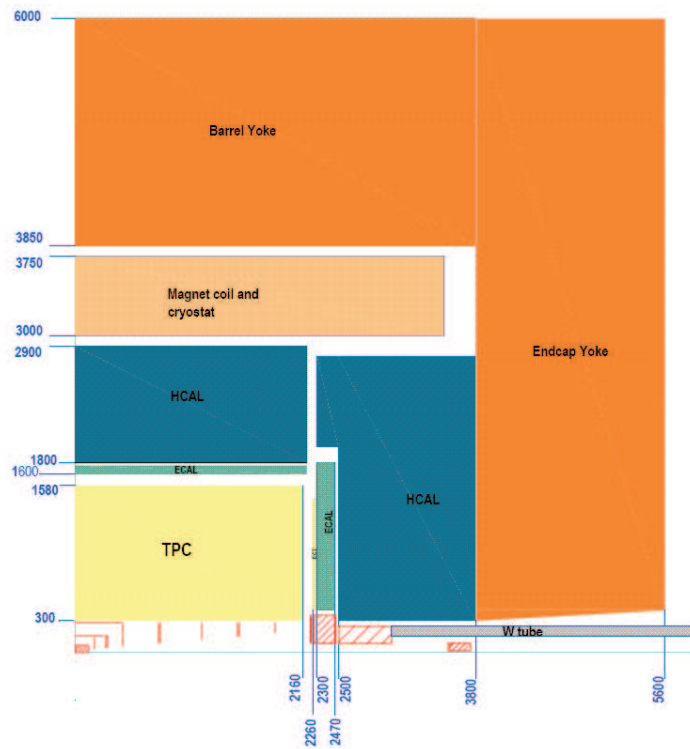


Figure 2.3: Quadrant view of the LDC detector, dimensions are in mm.

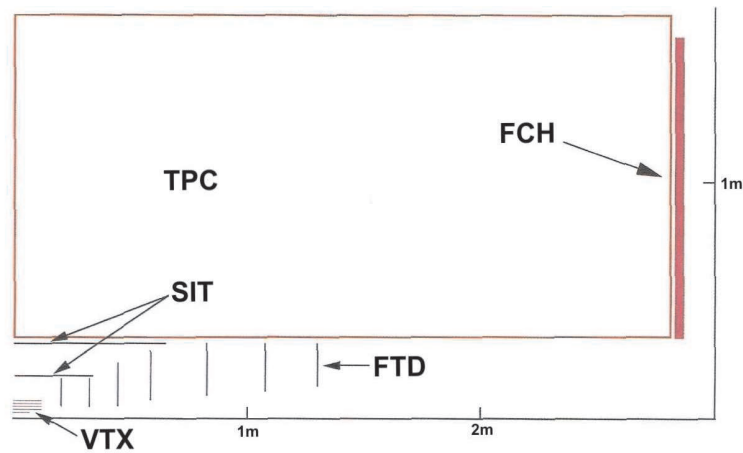


Figure 2.4: Layout of the tracking system in TESLA TDR detector

Table 2.2: SIT position and sizes in TESLA and LDC detector design.

Detector	radius [mm]	half length in z [mm]
TESLA	160	360
	300	640
LDC	150	180
	290	450

induced electromagnetic interference ... The list of the wishes is long as always. Several technologies (DEPFET, CCD) are under consideration hoping that development will bring one of them close to the requirements without the significant penalty on any of the issues. There were no changes in the detector layout between TESLA and the LDC detector.

SIT detector serves as a bridge between the vertex and the TPC for merging of the track segments and provides additional points for low  $p_t$  tracks that do not reach the TPC. The SIT consist of two layers of silicon strip detectors. Radial positions and lengths of the layers have changed between TESLA and LDC detector and are summarized in Table.2.2. The design goal for the point resolution is unchanged and equals  $10\mu m$ .

The FTD has the same connecting role as the SIT with the addition that it should improve accuracy of tracking at low angles. Although with the same role as the SIT forward disc are operation at background conditions that are much closer to the vertex detector thus putting larger constrains on the applied technology. It consists of 7 silicon detector discs where the first 3 are pixel detector and the remaining 4 are double sided strip detectors. An additional disc is proposed in the LDC detector to be in front of the LumiCAL. There were significant reshuffling of the positions and sizes of the FTD discs. Changes are summarized in Table.2.3.

The TPC is main part of the tracking system. The performance goals for the TPC are a momentum resolution of  $\delta(1/p_t) \sim \times 10^{-4} (GeV)^{-1}$  and  $dE/dx$  measurement better then 5%. The main advantage of the TPC, with respect to silicon, is that tracks are measured with large number of space point that will provide the highly efficient tracking needed. The measurement is realized with minimal additional material since it will operate at atmospheric pressure with significant amount of additional material only in the endplate region. The relatively moderate single point precision of  $100\mu$  in  $r - \phi$  and 2mm in z is more then compensated with the ability to localize interactions and decays within its volume and provide  $dE/dx$  measurement

Table 2.3: FTD disks layout. Comparison for TESLA and LDC detector (numbers in brackets).

	inner radius [mm]	z position[mm]	min angle [ $^\circ$ ]
disc 1	29(40)	200(180)	8.25(12.0)
disc 2	32(47.5)	320(300)	5.71(9.0)
disc 3	35(57.5)	440(450)	4.55(11.6)
disc 4	51(87.5)	550(800)	5.30(10.9)
disc 5	72(122.5)	800(1200)	5.14(5.83)
disc 6	93(157.5)	1050(1550)	5.06(5.8)
disc 7	113(187.5)	1300(1900)	4.96(5.6)

Table 2.4: TPC dimensions in TESLA and LDC detector design.

Detector	inner r [mm]	outer r [mm]	TPC $L_{z/2}$ [mm]	Endplate $L_{z/2}$ [mm]
TESLA	320	1700	2730	230
LDC	300	1580	2160	160

to support particle identification. Special attention is needed for the choice of the gas. It should give sufficiently large primary ionization, have small transverse diffusion and fast drift  $> 5 \sim cm/\mu s$ . In addition it should have as small as possible crosssection for interaction with thermal neutron background. Signal amplification is realized with Gas Electron Multipliers (GEM)[12] or Micromegas[13] that are able to provide the needed amplification with minimizing ion back-drift at the same time. One of the essentials for application of TPC is not only strength of the magnetic field but also its uniformity. The homogeneity condition can be expressed as integral of radial field component  $B_\phi$  divided by the longitudinal component  $B_z$  over the drift length.

$$\int_{drift} B_\phi/B_z dz < 2mm \quad (2.1)$$

The overall size (thus angular coverage) and the total material budget are of special interest for reconstruction. The inner radius is limited with design of the forward region and background conditions. The outer radius is, driven by the needed number of measurement points with a given resolution and in addition is limited by the coil radius and the space requirements for the calorimeters. There was a significant size change from the initial design as shown in Table.2.4. Note that the length of active volume has changed by 0.5m! The endplate thickness has changed the physical length by keeping the material budget in radiation lengths the same ( $0.3X_0$ ).

The FCH (ETD) has the role of supporting the TPC in the low angle region and to allow accurate extrapolation into the calorimeter. Except of the name this detector has suffered a technology change from straw tubes to silicon planes. This leads to the reduction in sub-detector thickness from 70 to 20mm and to a smaller material budget. Even with this changes the fate of the sub-detector depends on what considerations will prevail between the minimization of material in front of the calorimeter or advantage of two precise points after the endplate. The overall tracking system performance goal is  $\delta(1/p_t) < 5 \times 10^{-5}(GeV)^{-1}$  but this number, although impressive, is reached only in the high energy limit and for the majority of physics processes irrelevant since it is driven mostly by Higgs mass measurement. What counts is tracking system reconstruction efficiency over polar angle and energy. Unfortunately

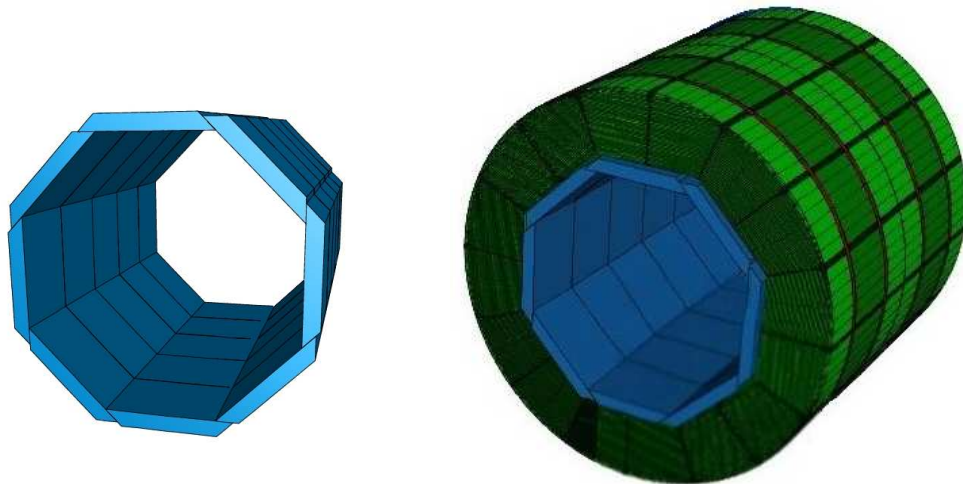


Figure 2.5: Barrel part of the ECAL on the left, barrel part of ECAL and HCAL on the right.

no results were presented for the new design as for the TESLA detector [14].

### 2.1.2 Electromagnetic calorimeter

Electromagnetic calorimeter (ECAL) as is Tungsten Silicon sampling calorimeter. The design is following some general considerations. Since we have separated calorimeters for electromagnetic and hadronic particles and we want to measure particles with “their” calorimeter the ECAL absorber must have large ratio of nuclear interaction length to the radiation length. At the same time we want calorimeter in which we can separate individual showers. This requirement prefers materials with small Molière radius, small radiation length as well as favorable ratio of the two and a large detector segmentation<sup>4</sup>. Active material should allow for the segmentation of the order of absorber Molière radius for the shower separation and precise determination of the photon direction. Compact design in terms of physical thickness is also strongly preferred due to the overall size constrains. These requirements have made tungsten absorber of a choice for electromagnetic calorimeter in all ILC designs. In LDC design detector are Silicon diodes with rectangular pads and 0.5mm thickness. Barrel part of the ECAL has octagonal symmetry consisting of identical modules arranged in the way to prevent projective cracks Fig.2.5. End cap part has same symmetry with quadratic hole in the middle for the beam pipe and low angle instrumentation. There were so far two proposals for the Si-W ECAL in terms of the sampling structure. In both proposals we have two different sampling structures with finer longitudinal segmentation in first half, and coarser in the second half. One of them follows the TESLA TDR and is implemented in the LDC00 MOKKA models, the second one is based on the DOD document and is implemented in LDC01 MOKKA models. In Table 2.5 the major characteristics of proposed designs are shown. Common for these two proposals is that total  $X_0$  thickness is kept constant as well as total interaction length of  $\sim 1\lambda$ . Reduction in number of layers reduces the cost and at the same time sampling thus resolution. There is a second source of proposed changes that is the change of the philosophy behind the design that has evolved from the “best possible resolution” approach to the “best possible segmentation” [15].

Resolution of the calorimeter is one of it’s major characteristics. Since ECAL is not

<sup>4</sup>will be discussed in Chapter 6.

Table 2.5: Comparison of existing ECAL designs.

Detector	Number of layers	W [mm]([ $X_0$ ])	cell size [ $mm \times mm$ ]	total absorber [ $X_0$ ]
LDC00	30	1.4 (0.4)	$10 \times 10$	24
	10	4.2 (1.2)	$10 \times 10$	
LDC01	20	2.1 (0.6)	$5 \times 5$	24
	10	4.2 (1.2)	$5 \times 5$	

monolith sub-detector but effectively consisting of two, or even three if one takes into the account ECALs tail catcher HCAL, energy dependence of the resolution will not be strictly in the form as in formulas 2.2 and 2.3 but very close to it. Resolution goal from the TESLA TDR calorimeter was<sup>5</sup>

$$\frac{\delta E}{E} = \frac{0.10}{\sqrt{E}} \oplus 0.01 \quad (2.2)$$

and for LDC version is

$$\frac{\delta E}{E} = \frac{0.144}{\sqrt{E}} \oplus 0.005 \quad (2.3)$$

Large longitudinal segmentation is mainly to reach the desired resolution. Transversal segmentation is driven by pattern recognition and separation constrains on the design have become more dominant that has reflected itself in to change of the baseline cell size from 10mm to 5mm together with more compact design of the calorimeter.

### 2.1.3 Hadronic calorimeter

Hadronic calorimeter is Iron Scintillator sampling calorimeter. It follows same considerations about segmentations as for the ECAL since it should be able to resolve close by hadronic showers as well as their subcomponents. Layers thickness is 26.5mm and it consists of 20mm of stainless steel and 5mm scintillator, making the longitudinal sampling 1.15 in  $X_0$  and 0.12 in  $\lambda$ . Resolution goal for the TESLA calorimeter was

$$\frac{\delta E}{E} = \frac{0.50}{\sqrt{E}} \oplus 0.01 \quad (2.4)$$

Granularity is 3 by 3cm through, and taking into account thickness of the absorber and the scintillator leading to almost cubic cell that is very convenient. Granularity was optimized from the point of the hadronic shower separation and possible detection of all of it's subcomponents. Segmentation is considerably smaller then the hadronic shower size as noticed in the [8], but of the order of Molière radius ( $\approx 23mm$  see Table.6.3) as it should be if one would like to resolve subcomponents of hadronic shower and thus not over segmented as one could conclude. Starting layers of HCAL serve also as a tail catcher for the ECAL, with electromagnetic resolution of around 20% it is doing excellent task. Only noticeable disadvantage of the current design is it's small thickness in interaction lengths (only  $4.6\lambda$ ) that could produce significant energy leakage and degrade reconstruction performance (if you still remember (Table.2.1) thickness of the GLD HCAL is  $5.8\lambda$ ).

<sup>5</sup>If we accept that detector is that what is implemented in simulation, resolution for the same calorimeter in G4 simulation is 12.5%

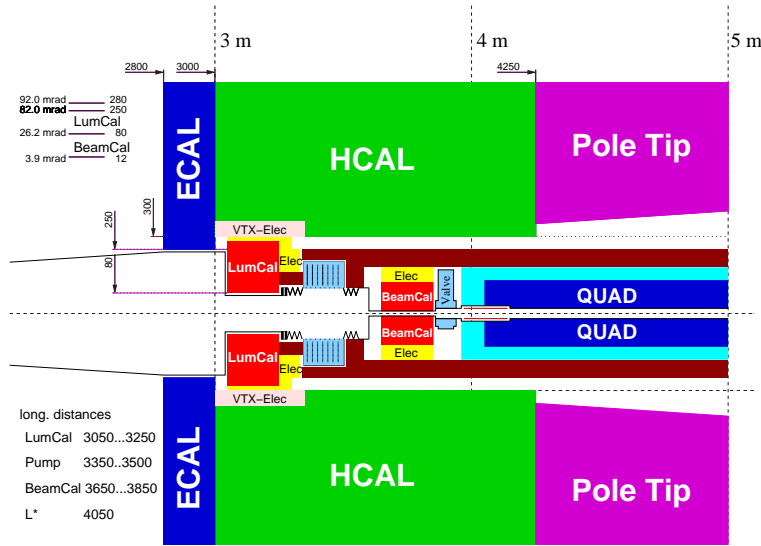


Figure 2.6: Modification of the TESLA forward region design

### 2.1.4 Muon system

Muon system is placed behind the magnet and the end-cap part of the hadronic calorimeter and is integrated in the iron yoke needed for the flux return and uniformity of the magnetic field. Yoke iron is segmented in layers of at least 10cm thickness with suitable detector in between. Performance challenges for this device are non existing due to the low event rates and no need for timing information for any kind of trigger. General requirements are that it should be reliable, inexpensive detector capable of covering area of around  $4000m^2$ . Segmentation is determined with the amount of multiple scattering that occurs in the calorimeters that amount to  $\approx 2cm$  at momentum of 20GeV. Thus position resolution of  $\approx 1cm$  is needed. Initially some ideas were expressed that this sub-detector could be used additionally as a tail catcher for the thin HCAL but  $1.6\lambda$  of the solenoid are making this impossible. Full simulation was without this sub-detector for years until it was finally implemented [16][17].

### 2.1.5 Forward region

Design of the forward region is one of the part that has suffered largest number of changes from the TESLA detector. The changes were introduced due to the careful study of the background absorption and emission from this region, changes in the machine design (from head on to crossing angle, and subsequent changes of the crossing angle size) and overall detector changes. In TESLA detector it consist of 2 detectors LumiCAL (initially called Low Angle Tagger) and BeamCal (former Low Angle Calorimeter LCAL). Overview of revisited original design one can see in Fig.2.6 [18]. Both sub-detectors are electromagnetic sampling calorimeters LumiCAL (W-Si) and BeamCal (W-Diamond). In addition to the hermeticity LumiCal can be used for luminosity measurement from Bhabha scattering, and BeamCal can serve as a fast feedback system for the beam delivery. Realizing importance of this region in the LDC detector third sub-detector is introduced LHCAL to cover missing hadron detection capability. Geometry of forward region in LDC is presented in Fig.2.7.

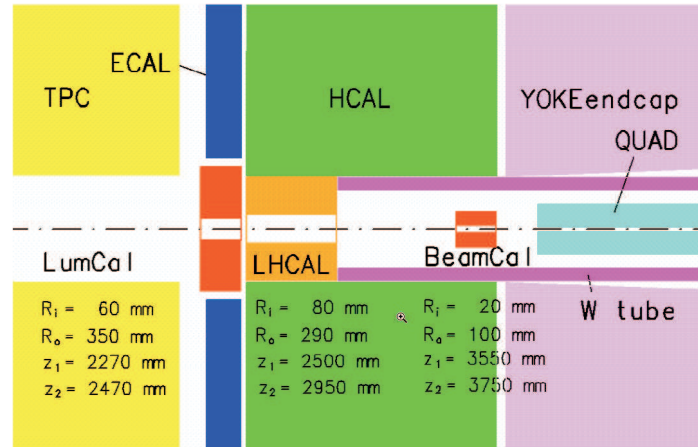


Figure 2.7: LDC design of the forward region

Table 2.6: Design changes between TESLA TDR and LDC DOD detector.

Sub-detector	TESLA detector	LDC detector	rating
Tracking volume	1600x2160mm	1700x2750mm	negative
TPC inner radius	320mm	300mm	positive
Endplate thickness	230mm	160mm	positive
ETD thickness	70mm	20mm	positive
Forward region	no hadr. cal.	added LHCAL	positive
ECAL sampling resolution	10+30 layers	10+20 layers	negative
cell size	10%	14%	negative
HCAL cell size	10x10mm	5x5 mm	positive
material change	changing through det. stainless steel	uniform 3x3cm iron in end-cap	positive

### 2.1.6 Detector design evolution

Five years has passed between TESLA TDR and LDC DOD document. At the moment these are two significantly different detectors. Some of the sub-detectors have changed some of them are still identical (Vertex and muon system). Here I will try to summarize these changes (Table.2.6) and make personal rating of each of them. Beautifully light motive for this can be: **“The idea was that some reshuffling of the detector could help making it easier to build, cheaper without sacrificing anything important in terms of performance”** [19].

Overall size of the detector has changed, detector has shrunk. This is done by reducing the length of the coil and removing the plug (ferromagnetic transition region between the HCAL and YOKE in the end cap needed for flux return). What are the consequences? Angular coverage of TPC has changed from 7.29 degrees<sup>6</sup> in the TDR design to 8.53 in the current one. Tiny reduction of the inner radius of the TPC cannot compensate drastic reduction in

<sup>6</sup>endpoint in sensitive volume

length. In addition to this there was significant redesign in the SIT and FTD layout. SIT is not covering same angular region till 25 degrees as the vertex detector but till 31.9. Also the lowest angles that are covered by the FTD discs were significantly raised (Table2.3) mostly by background consideration and in order to relax constrains on the hardware. But taking into account vertex coverage till 12 degrees and that closest FTD discs coverage till 9 degrees together with increased distance of of the discs with low angle coverage further from IP one would expect no tracking for low energy particles below 9 degrees and questionable one for others below this angle. Radial size reduction will not affect tracking performance significantly. ECAL has also suffered changes number of layers is reduced from 40 to 30, thus sampling is coarser and resolution has changed accordingly. The hope is that more dense calorimeter and finer transversal segmentation will compensate for worsen resolution by allowing to reduce amount of errors made by reconstruction . On the other hand keeping the same magnetic field and bringing the calorimeter face closer to the IP means that average distance between the particles on the face of the calorimeter will also decrease reducing part of the promised gain (if any). Since the plug is removed in order to fulfill requirements of field homogeneity needed for the tracking (eq.2.1 ) HCAL now needs to be changed also. Absorber in the end cap part must be ferromagnetic. This will increase amount of dead material in HCAL since support should now cope not only with calorimeters own weight but also with magnetic forces. Additionally corner part of the HCAL end-cap is now close to the edge of the coil thus in the region of highly inhomogeneous field that will add complications to the calibration<sup>7</sup>.

Angular coverage of the the tracking system is reduced roughly by 2 degrees, resolution of the ECAL is reduced with unclear gain in reconstruction performance, amount of dead material in the HCAL is increased but the detector is cheaper,easier to build and we have not sacrificed anything important. By the way if one looks at Reference Design Report [20] LDC is still only detector that has single sub-detector more expensive then the coil. Why is not possible to accept that superior detector has its price is beyond my ability to comprehend.

What was the intention of such accelerator and detector introduction? First of all to make it clear that scope of the project is changing together with the detector designs, and that things that are assumed realistic and for granted at one point in time may look different at another. Second, altho people tend to mix TESLA and LDC detector these are two different detectors and should be treated as such.

---

<sup>7</sup>to be discussed in Chapter 5



# Chapter 3

## Quartic couplings

Unfortunately before we can jump to the measurement of quartic couplings and interpretation of the result we need a bit longer theoretical introduction in order to make the text readable to non-expert. We will start from the Standard Model (SM) as a basic theory of elementary particles and their interactions as we know them today, explain how the electroweak sector is realized within SM and what is the solution to the mass generation within the SM. After that Effective Lagrangian will be introduced as a general framework within which we will discuss quartic couplings. At the end we will introduce relations between the possible new resonances and quartic couplings. Together with the proposed approach to the measurement of quartic couplings this will provide us with the understanding needed for the next chapter. If someone does not like my style or amount of detail dedicated to particular issue you can find in books [21],[21] and reviews and lectures [23], [24],[25] additional quotations will be within the text on the specific issues. There is absolutely no personal contribution to the content of this chapter except the errors in typing. Basic notation is explained in appendix A.

### 3.1 Standard Model

Standard Model [26] is a re-normalizable quantum field theory that describes electroweak and strong interactions of quarks and leptons which are the most elementary components of matter known at present. One of the essential features of the model is that both the electroweak and the strong force are introduced as gauge interactions. In this description it is possible to define three separate parts: First the matter sector which is made of fermionic fields; second there are vector boson gauge fields and finally the symmetry breaking sector. This sector is needed in order to provide masses for fermions and weak bosons. Simplest realization of the symmetry breaking sector is a doublet of self interacting scalar fields - famous Higgs boson. The matter part of the SM consist of fermions organized in three generations as shown in Table.3.1. Each generation is made of two quark flavors (u and d like) and two leptons (neutrino and electron like). All these particles are accompanied by their corresponding anti particles with same mass and opposite charges.

In the SM there are two types of gauge interactions. Strong interaction among the quarks modeled by the quantum chromo dynamics - gauge theory based on the  $SU(3)$  symmetry group. Electroweak theory describes the electromagnetic and weak interaction on the basis of  $SU(2)_L \times U(1)_Y$  group. Particles are arranged in the multiplets that transform according to the symmetry of interaction.

Neutrinos occur only in the left-handed (negative helicity ) state and anti neutrinos only in the right-handed state. This implies that only  $\psi_L$  and  $\psi_L^\dagger$  can be present in the field theory

Table 3.1: Elementary particles and their interactions.

	Quarks		Leptons	
first generation	u	d	$\nu_e$	e
second generation	c	s	$\nu_\mu$	$\mu$
third generation	t	b	$\nu_\tau$	$\tau$
strong interaction	yes	yes	no	no
strong interaction	color triplet		color singlet	
electromagnetic int.	yes	yes	no	yes
electromagnetic int.	$Q = 2/3$	$Q = -1/3$	$Q = 0$	$Q = -1$
weak interaction	yes	yes	yes	yes

for the neutrinos. Theory can be formulated with two spinor  $\begin{pmatrix} 1 \\ 0 \end{pmatrix}$  and  $\begin{pmatrix} 0 \\ 1 \end{pmatrix}$ .

We could introduce the theory in at least two ways formal, mathematical one and more historical. Second approach is more useful to demonstrate how the theory was developed and subsequently patched, and updated to accommodate experimental facts.

### Fermi theory

After Pauli [30, 31] introduced neutrino to explain continuous spectrum of  $\beta$  decay, Fermi [32] proposed field theory for  $\beta$  decay, assuming existence of neutrino. In analogy to "the theory of radiation that describes the emission of a quantum of light from an excited atom" Fermi proposed a current-current Lagrangian to describe  $\beta$  decay.

$$\mathcal{L} = \frac{G_F}{\sqrt{2}} (\bar{\psi}_p \gamma_\mu \psi_n) (\bar{\psi}_e \gamma^\mu \psi_\nu) \quad (3.1)$$

This is effectively start of the electroweak theory. Gammov and Teller [33] proposed an extension to Fermi theory to describe also transitions with  $\Delta J \neq 0$ . Pontecorvo [34] first idea about universality of weak interactions i.e. decay and capture have same origin. Thus in general

$$\mathcal{M}_{fi} \approx \sum_i C_i (\bar{u}_p O_i u_n) (\bar{u}_e O_i u_\nu) \quad (3.2)$$

where the sum is over the possible form of the bilinear covariants  $i=S,V,T,A,P$ .

$$S = 1, P = \gamma_5, V = \gamma_\mu, A = \gamma_\mu \gamma_5, T = \sigma_{\mu\nu} \quad (3.3)$$

Nuclear transition with  $\Delta J = 0$  are described by the interaction of SS and/or VV type, while  $\Delta J = 0, \pm 1$  can be take into account by AA and or TT interactions ( $P \rightarrow 0$  in non-relativistic limit). Interference between them are proportional to  $m_e/E_e$  and should increase the emission of low energy electrons. Since this is not observed the weak Lagrangian should contain *SS or VV and AA or TT* terms. From four possible combinations ST,SA,VT and VA two (SA and VT could be discarded on the basis of energy spectrum). In order to accommodate parity-violating effects one must add terms to the matrix elements which are pseudo-scalars, obtained by contracting two covariants which have the opposite behavior under parity transformation. Most general pseudo-scalar is thus

$$\mathcal{M}_{fi} \approx \sum_i C'_i (\bar{u}_p O_i u_n) (\bar{u}_e O_i \gamma_5 u_\nu) \quad (3.4)$$

with different coefficients  $C'_i$  for parity-violating terms. From experiment beta decay is time reversal invariant thus the coefficients  $C_i$  and  $C'_i$  must be real. Neutrino and antineutrino have definite handedness -parity violation is maximal - and this implies  $C'_i = \pm C_i$

$$\mathcal{M}_{fi} = \frac{G}{\sqrt{2}} \sum_i C_i (\bar{u}_p O_i u_n) (\bar{u}_e O_i (1 \pm \gamma_5) u_\nu) \quad (3.5)$$

Precise measurement of energy spectrum, and angular correlations lead to determination of V-A nature for beta decay. Problem of the Fermi theory was energy behavior of scattering processes. Point like neutrino electron scattering cross section (ignoring the spin effects) is:

$$\sigma(\nu_e e \rightarrow \nu_e e) = \frac{G^2 s}{\pi} \quad (3.6)$$

On the other hand maximum elastic cross section allowed by unitarity for point like or S wave scattering is:

$$\sigma_{el}^{max} = \frac{4\pi}{k^2} (2l + 1) = \frac{4\pi}{k^2} \quad (3.7)$$

And now we have clear contradiction of eq.3.6 and eq.3.7, that allows to estimate energy at which the theory breaches unitarity that is around 300GeV. This implied that Fermi theory, could not be final theory for the weak interactions but, **is effective low energy theory**.

### Gauge principle

There are in general two types of symmetries global (space time independent) and local (functions of space and time coordinate). Let us now try other way around we will ask for the theory to be invariant under local transformation and look what interaction it implies. Best example for this is the Quantum Electrodynamics (QED) that has become a prototype of quantum field theory. Thus we will start from the Dirac free Lagrangian

$$\mathcal{L}_\psi = \bar{\psi} (i\gamma^\mu \partial_\mu - m) \psi \quad (3.8)$$

and investigate its behavior under global and local transformations. It is obvious that A.26 is invariant under transformation

$$\psi \rightarrow \psi' = \exp[-i\alpha] \psi \quad (3.9)$$

were  $\alpha$  is scalar constant (space-time independent). Under local transformation

$$\psi \rightarrow \psi' = \exp[-i\alpha(x)] \psi \quad (3.10)$$

The phase transformation is local one dimensional transformation that additionally satisfies the unitarity condition i.e. it is a representation of the U(1) group. Lagrangian transforms to

$$\mathcal{L} \rightarrow \mathcal{L}' = \mathcal{L} + \bar{\psi} \gamma_\mu \psi (\partial^\mu \alpha) \quad (3.11)$$

and is not invariant. However if we introduce the gauge field  $A_\mu$  through the minimal coupling

$$\partial_\mu \rightarrow D_\mu \equiv \partial_\mu + ieA_\mu \quad (3.12)$$

and at the same time require that  $A_\mu$  transforms as

$$A_\mu \rightarrow A'_\mu = A_\mu + \frac{1}{e} \partial_\mu \alpha. \quad (3.13)$$

we get

$$\mathcal{L} \rightarrow \mathcal{L}' = \mathcal{L} - e\bar{\psi}\gamma_\mu\psi A^\mu \quad (3.14)$$

Thus invariance is kept under simultaneous transformations 3.10 and 3.13 and replacement  $\partial_\mu \rightarrow D_\mu$  that together form a gauge transformation. Important to mention is that derivatives of the field are transforming in the same way as the field itself making any Lagrangian that consist of fields and their derivatives manifestly invariant.

$$D'_\mu\psi' = \exp[-i\alpha(x)]D_\mu\psi \quad (3.15)$$

Thus coupling between the matter field and the gauge field arises naturally when we require the invariance under local gauge transformation of the kinetic energy terms in free fermion Lagrangian. Since the electromagnetic strength tensor is invariant under the gauge transformation

$$F_{\mu\nu} \equiv \partial_\mu A_\nu - \partial_\nu A_\mu \quad (3.16)$$

so is the Lagrangian for the free gauge field.

$$\mathcal{L}_A = -\frac{1}{4}F_{\mu\nu}F^{\mu\nu} \quad (3.17)$$

making together with 3.14 Lagrangian of the QED.

$$\mathcal{L} = \mathcal{L}_\psi - e\bar{\psi}\gamma_\mu\psi A^\mu - \frac{1}{4}F_{\mu\nu}F^{\mu\nu} \quad (3.18)$$

Direct mass term  $-1/2 m^2 A_\mu A^\mu$  violates gauge invariance thus gauge boson is massless, and one needs another mechanism if one would like to have massive gauge boson field. Since the transformation is commutative QED is an example of Abelian gauge theory.

### Yang-Mills theories

As suggested by Heisenberg [35] in 1932 under nuclear transitions proton and neutron can be regarded as degenerated since their masses are similar and electromagnetic interaction is negligible. Therefore arbitrary combination of their wave functions would be

$$\psi \equiv \begin{pmatrix} \psi_p \\ \psi_n \end{pmatrix} \quad (3.19)$$

Lagrangian should be invariant under matter field transformation

$$\psi \rightarrow \psi' = U\psi \quad (3.20)$$

where U is unitary transformation ( $U^\dagger U = U U^\dagger = 1$ ) to preserve normalization. If  $\det|U| = 1$ , U represents Lie group [53] SU(2)

$$U \equiv \exp[-i\frac{\tau^a}{2}\alpha^a(x)] \simeq 1 - i\frac{\tau^a}{2}\alpha^a(x) \quad (3.21)$$

where  $\tau^a$ , a=1,2,3 are Pauli matrices. Important difference to the example of QED is that generators of SU(2) do not commute giving the name to the theories as non Abelian. Result was generalized by Utiyama [36] for any non-Abelian group satisfying Lie algebra. Lagrangian should be invariant under matter field transformation 3.20 with

$$U \equiv \exp[-iT^a\alpha^a(x)] \quad (3.22)$$

where  $T^a$  is convenient representation of the generators  $t^a$ . Introducing one gauge field for each generator and defining the covariant derivative by

$$D_\mu \equiv \partial_\mu - igT^a A_\mu^a \quad (3.23)$$

this assures the invariance under local non-Abelian gauge transformation for the terms containing the fields and its gradients as long as the gauge field transformation is

$$T^a A_\mu^a \rightarrow U(T^a A_\mu^a + \frac{i}{g}\partial_\mu)U^{-1} \quad (3.24)$$

or in infinitesimal form i.e for  $U \simeq 1 - iT^a \alpha^a(x)$

$$A_\mu^{a'} = A_\mu^a - \frac{1}{g}\partial_\mu \alpha^a + C_{abc}\alpha^b A_\mu^c \quad (3.25)$$

Generalized form of the strength tensor for a non Abelian Lie group

$$F_{\mu\nu}^a \equiv \partial_\mu A_\nu^a - \partial_\nu A_\mu^a + gC_{abc}A_\mu^b A_\nu^c \quad (3.26)$$

where  $C_{abc}$  is structure constant of the group (sec.A.0.5, eq.A.14). However a direct mass term for the gauge bosons is again not invariant:

$$A_\mu^a A^{a\mu} \rightarrow \left(A_\mu^a - \frac{1}{g}\partial_\mu \alpha^a + C_{abc}\alpha^b A_\mu^c\right) \left(A^{a\mu} - \frac{1}{g}\partial_\mu \alpha^a + C_{ade}\alpha^d A^{e\mu}\right) \quad (3.27)$$

Form of the strength tensor 3.26 produces important feature of non-Abelian theory, since

$$F \propto (\partial A - \partial A) + gAA \quad (3.28)$$

gauge part of the Lagrangian is:

$$\mathcal{L} \propto (\partial A - \partial A)^2 + g(\partial A - \partial A)AA + g^2AAAA \quad (3.29)$$

thus we now have additional self interaction of the gauge fields, where second term describes triple and third quartic couplings. Triple and quartic couplings arise naturally in non-Abelian gauge theory.

### 3.1.1 Electroweak sector

From the introduction of the Fermi theory to late 50-ties large amount of experimental facts about weak interactions were collected that allowed attempts to construct a gauge theory. Lepton number conservation ( pion decay  $\pi^+ \rightarrow \mu^+ \nu_\mu$  and consequent reaction  $\nu_\mu + n \rightarrow p + \mu^-$  but no  $\nu_\mu + n \rightarrow p + e^-$ ). Also no muon decay channels of the kind  $\mu^\pm \rightarrow e^\pm + \gamma$  or  $\mu^\pm \rightarrow e^\pm + e^+ + e^-$  i.e. no flavor-changing neutral currents. Confirmation of parity violation in weak processes by Wu et al. [47] in 1957. Measurement of the neutrino helicity [48] in 1958, and decay chain of pions  $\pi^+ \rightarrow \mu^+ \nu_\mu, \mu^+ \rightarrow e^+ + \nu_e + \bar{\nu}_\mu$  [49] in 1957. Antineutrino helicity measured in decay of polarized neutrons [50] in 1958.

Several attempts to construct a gauge theory of weak interactions. In 1957, Schwinger [37] suggested a model based on the group  $O(3)$  with triplet gauge fields ( $V^+, V^-, V^0$ ), where charged gauge bosons were associated to weak bosons and the neutral was identified as photon. This was before the V-A structure of the weak current was established [38, 39, 40]. First attempts to incorporate V-A structure in gauge theory was made by Bludman [41] and Lopes [42] in 1958. Gashow [43] in 1961, and Salam and Ward [26] in 1964 proposed a model

based on  $SU(2) \otimes U(1)$  group, where  $U(1)$  is associated to the leptonic hypercharge ( $Y$ ) that is related to the weak isospin ( $T$ ) through the Gell-Mann-Nishijima formula  $Q = T_3 + Y/2$ . Theory required four gauge bosons a triplet associated to  $SU(2)$  generators and a neutral field related to  $U(1)$ . Mass terms were put by hand! Weinberg [44], Salam [45] employed the idea of spontaneous symmetry breaking and the Higgs mechanism to give mass to the weak bosons and preserve gauge invariance. Renormalizability of the theory was finally proven by 't Hooft [46]. We require local gauge invariance under both  $SU(2)_L$  and independently  $U(1)_Y$  this will introduce interactions in the free-field Lagrangian. In order to incorporate experimental facts fermions are organized in left handed doublets and right handed singlets.

$$L = \begin{pmatrix} \nu_l \\ l^- \end{pmatrix}_L, R = l_R^- \quad (3.30)$$

where  $l = e, \mu, \tau$ . Theory does not necessarily involve right-handed neutrinos, and their inclusion in spectrum is allowed but not required. We start as usual from free fermion Lagrangian:

$$\mathcal{L} = \bar{L}i\gamma^5\partial L + \bar{R}i\gamma^5\partial R \quad (3.31)$$

Under local gauge transformations the fermion fields transform as below:

$$\begin{array}{ll} SU(2)_L & U(1)_Y \\ L \rightarrow \exp[-i(g/2)\vec{\Lambda}(x)\vec{\tau}]L & L \rightarrow \exp[-i(g'/2)\lambda(x)Y]L \\ R \rightarrow R & R \rightarrow \exp[-i(g'/2)\lambda(x)Y]R \end{array} \quad (3.32)$$

where  $\lambda(x), \vec{\Lambda}(x)$  are arbitrary coordinate functions,  $\tau$  are Pauli matrices (eq.A.9). Since we have now introduced transformation we can construct the covariance derivative

$$D_\mu = \partial_\mu + \frac{1}{2}ig\vec{\tau}\vec{W}_\mu + \frac{1}{2}ig'YB_\mu \quad (3.33)$$

i.e. for left handed doublets

$$D_{L\mu} = \partial_\mu + \frac{1}{2}ig\vec{\tau}\vec{W}_\mu + \frac{1}{2}ig'Y_L B_\mu \quad (3.34)$$

and for right handed singlets

$$D_{R\mu} = \partial_\mu + \frac{1}{2}ig'Y_R B_\mu \quad (3.35)$$

and defining the strength tensor for the gauge fields

$$\begin{aligned} W_{\mu\nu}^i &\equiv \partial_\mu W_\nu^i - \partial_\nu W_\mu^i + g\epsilon^{ijk}W_\mu^j W_\nu^k \\ B_{\mu\nu} &\equiv \partial_\mu B_\nu - \partial_\nu B_\mu \end{aligned} \quad (3.36)$$

we can write the free Lagrangian for the gauge fields.

$$\mathcal{L}_{gauge} = -\frac{1}{4}W_{\mu\nu}^i W^{i\mu\nu} - \frac{1}{4}B_{\mu\nu} B^{\mu\nu} \quad (3.37)$$

Now we can look at the fermion boson part of the Lagrangian, again replacing the covariant derivatives in the free Lagrangian.

$$\mathcal{L}' \rightarrow \mathcal{L} + \bar{L}i\gamma^\mu \left( i\frac{g}{2}\vec{\tau}^i W_\mu^i + i\frac{g'}{2}Y B_\mu \right) L + \bar{R}i\gamma^\mu i\frac{g'}{2}B_\mu R \quad (3.38)$$

and separate the “charged” part of the Lagrangian:

$$-g\bar{L}\gamma^\mu\left(\frac{\tau^1}{2}W_\mu^1 + \frac{\tau^2}{2}W_\mu^2\right)L \quad (3.39)$$

and compare it with the charged current leads to the definition of the physical charged gauge bosons.

$$W^\pm = \frac{1}{\sqrt{2}}(W_\mu^1 \mp iW_\mu^2) \quad (3.40)$$

Sorting the terms in the “neutral” part of eq.3.38 we get:

$$\begin{aligned} & -\frac{g}{2}\bar{L}\gamma^\mu\tau^3LW_\mu^2 - \frac{g'}{2}(\bar{L}\gamma^\mu YL + \bar{R}\gamma^\mu YR)B_\mu \\ & = -\frac{g}{2}(\bar{\nu}_L\gamma^\mu - \bar{l}_L\gamma^\mu l_L)W_\mu^3 + \frac{g'}{2}(\bar{\nu}_L\gamma^\mu + \bar{l}_L\gamma^\mu l_L + 2\bar{R}\gamma^\mu l_R)B_\mu \end{aligned} \quad (3.41)$$

that we want to assign to a neutral current, this can be achieved by rotation of the neutral fields to new fields A and Z

$$\begin{aligned} A_\mu &= B_\mu \cos \theta_W + W_\mu^3 \sin \theta_W \\ Z_\mu &= -B_\mu \sin \theta_W + W_\mu^3 \cos \theta_W \end{aligned} \quad (3.42)$$

where the weak mixing angle  $\theta_W$  (called Weinberg angle) is define as  $\tan \theta_W = g'/g$ , and electromagnetic coupling constant is then  $e = g \sin \theta_W = g' \cos \theta_W$ . Now we have full description of matter and fields part of theory. Note that all the particles are still massless. Introduction of mass terms by hand breaks down the gauge invariance. Since it was know that particles have masses long before development of theory meaningful explanation must exist.

### 3.1.2 Symmetry breaking sector

For incorporating the masses in the electroweak theory there were two essential additional ingredients needed first is Goldston theorem [28, 29] stating that whenever exact continuous global symmetry is spontaneously broken, i.e. it is not the symmetry of physical vacuum, the theory contains one massless scalar particle for each broken generator of original symmetry group. This seems not to help since it can only generate massless particles and we already have too much of them. Symmetry requirements came to the rescue again. If we require that the Lagrangian which exhibits spontaneous symmetry breaking is also invariant under **local**, rather than global transformation we get the Higgs mechanism [56, 57, 58]. We will consider spontaneous breaking of a local gauge symmetry, namely  $SU(2)_L \times U(1)_Y$ . We introduce a scalar doublet of complex fields:

$$\phi = \begin{pmatrix} \phi^+ \\ \phi^0 \end{pmatrix} = \frac{1}{\sqrt{2}} \begin{pmatrix} \phi_1 + i\phi_2 \\ \phi_3 + i\phi_4 \end{pmatrix} \quad (3.43)$$

and its Lagrangian

$$\mathcal{L} = (\partial_\mu \phi)^\dagger (\partial^\mu \phi) - \mu^2 \phi^\dagger \phi - \lambda (\phi^\dagger \phi)^2 \quad (3.44)$$

The Lagrangian is manifestly invariant under global  $SU(2)$  transformations. In order to make it locally invariant we replace.

$$\mathcal{D}_\mu = \partial_\mu + ig \frac{\tau_i}{2} W_\mu^i + ig' \frac{Y}{2} B_\mu \quad (3.45)$$

and the gauge invariant Lagrangian is

$$\mathcal{L} = \left(\mathcal{D}_\mu\phi\right)^\dagger\left(\mathcal{D}^\mu\phi\right) - V(\phi) - \frac{1}{4}\vec{W}_{\mu\nu}\vec{W}^{\mu\nu} - \frac{1}{4}B_{\mu\nu}B^{\mu\nu} \quad (3.46)$$

minimum of the potential part is at

$$\phi^\dagger\phi = \frac{1}{2}(\phi_1^2 + \phi_2^2 + \phi_3^2 + \phi_4^2) = -\frac{\mu^2}{2\lambda} = \frac{v^2}{2} \quad (3.47)$$

an by making a specific choice for the minimum i.e. breaking the symmetry

$$\phi_1 = \phi_2 = \phi_4 = 0 \quad \phi_3^2 = v^2 \quad (3.48)$$

now we expand around chosen ground state of the vacuum.

$$\phi(x) = \frac{1}{\sqrt{2}} \begin{pmatrix} 0 \\ v + H(x) \end{pmatrix} \quad (3.49)$$

thus arbitrary field can be parameterized in the form

$$\phi(x) = \frac{1}{\sqrt{2}} \begin{pmatrix} 0 \\ v + H(x) \end{pmatrix} \exp\left[\frac{i\vec{\alpha}(x)\vec{\tau}}{2v}\right] \quad (3.50)$$

takin into account gauge transformation of the field

$$\phi(x) \rightarrow \phi'(x) = \phi(x) \exp\left[\frac{i\vec{\Lambda}(x)\vec{\tau}}{2}\right] \quad (3.51)$$

we can choose a gauge parameter to cancel exponential terms so that

$$\phi'(x) = \frac{1}{\sqrt{2}} \begin{pmatrix} 0 \\ v + H(x) \end{pmatrix} \quad (3.52)$$

Since only one component gets the vacuum expectation value the SU(2) symmetry is broken, with hypercharge  $Y \neq 0$  also U(1) is broken. Although choice of the vacuum may seem arbitrary it is not. If  $\phi^+$  would have a vacuum expectation value charge would not be conserved contrary to observations. Vacuum is invariant under  $\phi_0 \rightarrow \phi'_0 = \exp[-i(x)Q]\phi_0 = \phi_0$  that is a U(1) transformation of electromagnetism thus we say that  $SU(2)_L \times U(1)_Y$  is broken to  $U(1)_{em}$ . taking together eq.3.46 and eq.3.49 and expanding, usual mass terms appear with:

$$M_W = \frac{1}{2}gv, M_Z = \frac{1}{2}\sqrt{g^2 + g'^2} \text{ and } M_\gamma = 0 \quad (3.53)$$

As for the bosons, direct mass terms are breaking gauge invariance for the fermions:

$$-m\bar{e}e = -m\bar{e}(P_L + P_R)e = -m(\bar{e}_R e_L + \bar{e}_L e_R) \quad (3.54)$$

Adding the gauge invariant part to the Lagrangian

$$\mathcal{L} = -g_e[\bar{L}\phi e_R + \bar{e}_R\phi L] \quad (3.55)$$

substituting L and  $\phi$  we get

$$\mathcal{L} = \frac{-g_e v}{\sqrt{2}}(\bar{e}_R e_L + \bar{e}_L e_R) - \frac{g_e}{\sqrt{2}}(\bar{e}_R e_L + \bar{e}_L e_R)H \quad (3.56)$$

First term has the form of an electron mass term with mass:

$$m_e = \frac{g_e v}{\sqrt{2}} \quad (3.57)$$

where  $g_e$  is the Yukawa coupling. A similar solution is applied for the generation of masses for the quarks. At this stage we have a theory that incorporates masses of all known particles but this solution to the mass problem is part of the problem itself. A first objection is an esthetic one, we have postulated a field with just the right quantum numbers to patch the theory and why should the nature obey this. The Higgs boson is still not observed. Since  $\lambda$  and  $\mu$  are free parameters as well as all the Yukawa couplings the predictivity of the theory with respect of the mass spectrum is zero thus leaving no explanation for the observed mass spectrum. A vacuum expectation value of  $v \sim 250 GeV$  is incompatible with the present cosmological models. The Higgs mass is affected by quadratic radiative corrections that would make it of the order of the scale of the new physics phenomena. If we want to be in the experimentally allowed range we have to ask for extremely fine and unnatural cancellation of divergences. The Higgs mass  $m_h = v\sqrt{2\lambda}$  is also a free parameter leaving open questions about weak or strong nature of symmetry breaking sector.

### Anomalous couplings

General form of the Lagrangian for the triple gauge couplings (TGC) sector is:

$$\begin{aligned} \mathcal{L}_{TGC} = & ie [g_1^\gamma A_\mu (W_\nu^- W^{+\mu\nu} - W_\mu^+ W^{-\mu\nu}) + \kappa^\gamma W_\mu^- W_\nu^+ A^{\mu\nu} + \frac{\lambda^\gamma}{M_W^2} W_\mu^{-\nu} W_{\mu\rho}^+ A^{\rho\mu}] \\ & + ie \frac{c_W}{s_W} [g_1^Z Z_\mu (W_\nu^- W^{+\mu\nu} - W_\nu^+ W^{-\mu\nu}) \\ & + \kappa^Z W_\mu^- W_\nu^+ Z^{\mu\nu} + \frac{\lambda^Z}{M_W^2} W_\mu^{-\nu} W_{\nu\rho}^+ Z^{\rho\mu}] \end{aligned} \quad (3.58)$$

The CP conserving couplings are related to the charge  $q_W$ , the magnetic dipole moment  $\mu_W$  and electric quadrupole moment  $Q_W^e$  of the W boson.

$$\begin{aligned} q_W &= eg_1^\gamma \\ \mu_W &= \frac{e}{2M_W} (g_1^\gamma + \kappa_\gamma + \lambda_\gamma) \\ Q_W^e &= -\frac{e}{M_W^2} (\kappa_\gamma - \lambda_\gamma) \end{aligned} \quad (3.59)$$

The behavior under charge (C) and parity (P) conjugation can be used to divide them into several groups. Couplings  $g_1^V, \kappa_V$  and  $\lambda_V$  conserve C and P. Electromagnetic gauge invariance requires  $g_1^\gamma = 1$  and  $g_5^\gamma = 0$  and reduces overall number of C and P conserving couplings to 5.  $SU(2)$  gauge invariance requires

$$\begin{aligned} \Delta\kappa_Z &= \Delta g_1^Z - \Delta\kappa_\gamma \tan^2 \theta_W \\ \lambda_Z &= \lambda_\gamma \end{aligned} \quad (3.60)$$

reducing number of free couplings to three. General form of the Lagrangian covering quartic

couplings sector is:

$$\begin{aligned}
\mathcal{L}_{QGC} = & e^2[g_1^{\gamma\gamma} A^\mu A^\nu W_\mu^- W_\nu^+ - g_2^{\gamma\gamma} A^\mu A_\mu W^{-\nu} W_\nu^+] \\
& + e^2 \frac{c_W}{s_W} [g_1^{\gamma Z} A^\mu Z^\nu (W_\mu^- W_\nu^+ + W_\mu^+ W_\nu^-) - 2g_2^{\gamma Z} A^\mu Z_\mu W^{-\nu} W_\nu^+] \\
& + e^2 \frac{c_W^2}{s_W^2} [g_1^{ZZ} Z^\mu Z^\nu W_\mu^- W_\nu^+ - g_2^{ZZ} Z^\mu Z_\mu W^{-\nu} W_\nu^+] \\
& + \frac{e^2}{2s_W^2} [g_1^{WW} W^{-\mu} W^{+\nu} W_\mu^- W_\nu^+ - g_2^{WW} (W^{-\mu} W_\mu^+)^2] \\
& + \frac{e^2}{4s_W^2 c_W^4} h^{ZZ} (Z^\mu Z_\mu)^2
\end{aligned} \tag{3.61}$$

### 3.2 Effective Lagrangian

A theory based only on the observed degrees of freedom (without Higgs) is non-renormalizable. At high energies there is a cutoff scale at which this theory stops to be predictive. In the case of the  $e^+e^- \rightarrow \nu^+W^-$  in the absence of the Higgs unitarity is violated around  $\sim 1.2TeV$ . Together with objections made to the SM we are almost in the same situation as in the early days of the Fermi theory. In this analogy and following historical development one is tempted to make the same conclusion that we are dealing with low energy effective theory and that one should collect enough experimental facts to conclude about the “true” theory. The way to do this is using the Effective Lagrangian [54, 55]. The lowest order Lagrangian is invariant under  $SU(2)_L \times SU(2)_R$  that is broken to  $SU(2)_C$  although  $SU(2)_C$  is broken by  $U(1)_Y$  and it is affected by correction to the  $\rho$  parameters ( $\rho \approx 1 + \mathcal{O}(g^2)$ )

$$\mathbf{W}_{\mu\nu} = \partial_\mu \mathbf{W}_\nu - \partial_\nu \mathbf{W}_\mu + ig[\mathbf{W}_\mu, \mathbf{W}_\nu] \tag{3.62}$$

$$\mathbf{B}_{\mu\nu} = \Sigma(\partial_\mu \mathbf{B}_\nu - \partial_\nu \mathbf{B}_\mu) \frac{\tau^3}{2} \Sigma^\dagger \tag{3.63}$$

Where the usual fields are  $W_\mu^a$  and  $B_\mu$  with abbreviation

$$\mathbf{W}_\mu = W_\mu^a \frac{\tau^a}{2} \quad \text{and} \quad \mathbf{B}_\mu = B_\mu \frac{\tau^3}{2} \tag{3.64}$$

and additional field  $\Sigma$  with suitable transformation law. The field  $\Sigma(x)$  is  $2 \times 2$  matrix which transforms under local  $SU(2)_L$  transformation  $U(x) = \exp[-i\alpha^a(x) \frac{\tau^a}{2}]$  and  $U(1)_Y$  transformation  $V = \exp(i\beta(x) \frac{\tau^3}{2})$  in the form

$$\Sigma(x) \rightarrow U(x)\Sigma(x)V^\dagger(x) \tag{3.65}$$

Introducing further abbreviations

$$\mathbf{V}_\mu = \Sigma(\mathbf{D}_\mu \Sigma)^\dagger \quad \text{and} \quad \mathbf{T} = \Sigma \tau^3 \Sigma^\dagger \tag{3.66}$$

where  $\mathbf{D}$  is a covariant derivative, allows to rewrite the direct mass terms and introduce the possibility to add an invariant potential term

$$\mathcal{L}_\Sigma = -\frac{\mu^2 v^2}{4} \text{tr}[\Sigma^\dagger \Sigma] + \frac{\lambda v^4}{16} \text{tr}[\Sigma^\dagger \Sigma]^2 + \dots \tag{3.67}$$

$$\Sigma = \exp\left(-\frac{i}{v}\mathbf{w}\right) \quad (3.68)$$

Goldston bosons  $\mathbf{w} \equiv w^a \tau^a$  The Scalars  $w^a$  are the Goldston bosons associated with spontaneous symmetry breaking. All together leading to the lowest order chiral Lagrangian:

$$\mathcal{L}_0 = -\frac{1}{2}\text{tr}[\mathbf{W}_{\mu\nu}\mathbf{W}^{\mu\nu}] - \frac{1}{2}\text{tr}[\mathbf{B}_{\mu\nu}\mathbf{B}^{\mu\nu}] - \frac{v^2}{4}\text{tr}[\mathbf{V}_\mu\mathbf{V}^\mu] + \beta'\mathcal{L}'_0 + \sum_i \alpha_i \mathcal{L}_i \quad (3.69)$$

$$\mathcal{L}'_0 = \frac{v^2}{4}\text{tr}[\mathbf{TV}_\mu]\text{tr}[\mathbf{TV}^\mu] \quad (3.70)$$

Imposing CP-invariance on the effective Lagrangian the complete list of dimension-four operators not contained in :

$$\begin{aligned} \mathcal{L}_1 &= gg' \text{tr}[\Sigma\mathbf{B}_{\mu\nu}\Sigma^\dagger\mathbf{W}^{\mu\nu}] \\ \mathcal{L}_2 &= ig' \text{tr}[\Sigma\mathbf{B}_{\mu\nu}\Sigma^\dagger[\mathbf{V}^\mu, \mathbf{V}^\nu]] \\ \mathcal{L}_3 &= ig \text{tr}[\mathbf{W}_{\mu\nu}[\mathbf{V}^\mu, \mathbf{V}^\nu]] \\ \mathcal{L}_4 &= (\text{tr}[\mathbf{V}_\mu\mathbf{V}_\nu])^2 \\ \mathcal{L}_5 &= (\text{tr}[\mathbf{V}_\mu\mathbf{V}^\mu])^2 \\ \mathcal{L}_6 &= \text{tr}[\mathbf{V}_\mu\mathbf{V}_\nu]\text{tr}[\mathbf{TV}^\mu]\text{tr}[\mathbf{TV}^\nu] \\ \mathcal{L}_7 &= \text{tr}[\mathbf{V}_\mu\mathbf{V}^\mu]\text{tr}[\mathbf{TV}_\nu]\text{tr}[\mathbf{TV}^\nu] \\ \mathcal{L}_8 &= \frac{1}{4}g^2 (\text{tr}[\mathbf{TW}_{\mu\nu}])^2 \\ \mathcal{L}_9 &= \frac{i}{2}g \text{tr}[\mathbf{TW}_{\mu\nu}]\text{tr}[\mathbf{T}[\mathbf{V}^\mu, \mathbf{V}^\mu]] \\ \mathcal{L}_{10} &= \frac{1}{2} (\text{tr}[\mathbf{TV}_\mu]\text{tr}[\mathbf{TV}_\nu])^2 \end{aligned} \quad (3.71)$$

And additional restricted set of dimension 6 operators :

$$\begin{aligned} \mathcal{L}_1^\lambda &= i\frac{g^3}{3M_W^2}\text{tr}(\mathbf{W}^{\mu\nu}\mathbf{W}_\nu^\rho\mathbf{W}_{\rho\mu}) \\ \mathcal{L}_2^\lambda &= i\frac{g^2g'}{M_W^2}\text{tr}(\mathbf{B}^{\mu\nu}\mathbf{W}_\nu^\rho\mathbf{W}_{\rho\mu}) \\ \mathcal{L}_3^\lambda &= i\frac{g^2}{M_W^2}\text{tr}([\mathbf{V}^\mu, \mathbf{V}^\nu]\mathbf{W}_\nu^\rho\mathbf{W}_{\rho\mu}) \\ \mathcal{L}_4^\lambda &= i\frac{g^2}{M_W^2}\text{tr}([\mathbf{V}^\mu, \mathbf{V}^\nu]\mathbf{B}_\nu^\rho\mathbf{W}_{\rho\mu}) \\ \mathcal{L}_5^\lambda &= i\frac{gg'}{2M_W^2}\text{tr}(\mathbf{T}[\mathbf{V}^\mu, \mathbf{V}^\nu])\text{tr}(\mathbf{TW}_\nu^\rho\mathbf{W}_{\rho\mu}) \end{aligned} \quad (3.72)$$

In case of nonlinear symmetry representation the Lagrangian contains terms of arbitrary high dimension. At each new order of perturbation new terms are introduced with the dimension of  $\Sigma$ -dependent term increased by two. In the SM quartic couplings sector can be then written:

Standard model values for the TGC are

$$g_1^\gamma = g_1^Z = \kappa_\gamma = \kappa_Z = 1 \quad \text{and} \quad \lambda_\gamma = \lambda_Z = 0 \quad (3.73)$$

with deviations

$$\begin{aligned} \Delta g_1^\gamma &= 0 \\ \Delta g_1^Z &= \delta_Z + \alpha_3 \frac{g^2}{c_W^2} \\ \Delta \kappa_\gamma &= g^2(\alpha_2 - \alpha_1) + g^2 \alpha_3 + g^2(\alpha_9 - \alpha_8) \\ \Delta \kappa_Z &= \delta_Z - g'^2(\alpha_2 - \alpha_1) + g^2 \alpha_3 + g^2(\alpha_9 - \alpha_8) \end{aligned} \quad (3.74)$$

$$\begin{aligned} \lambda_\gamma &= -\frac{g^2}{2}(\alpha_1^\lambda + \alpha_2^\lambda) \\ \lambda_Z &= -\frac{g^2}{2}\left(\alpha_1^\lambda - \frac{s_W^2}{c_W^2}\alpha_2^\lambda\right) \end{aligned} \quad (3.75)$$

for the QGC standard model values are

$$g_1^{VV'} = g_2^{VV'} = 1 \quad \text{and} \quad h^{ZZ} = 0 \quad (3.76)$$

where  $VV' = \gamma\gamma, \gamma Z, ZZ, WW$ . And deviations from SM values are:

$$\begin{aligned} \Delta g_1^{\gamma\gamma} &= \Delta g_2^{\gamma\gamma} = 0 \\ \Delta g_1^{\gamma Z} &= \Delta g_2^{\gamma Z} = \delta_Z + \frac{g^2}{c_W^2}\alpha_3 \\ \Delta g_1^{ZZ} &= 2\Delta g_1^{\gamma Z} + \frac{g^2}{c_W^4}(\alpha_4 + \alpha_6) \\ \Delta g_2^{ZZ} &= 2\Delta g_1^{\gamma Z} - \frac{g^2}{c_W^4}(\alpha_5 + \alpha_7) \\ \Delta g_1^{WW} &= 2c_W^2\Delta g_1^{\gamma Z} + 2g^2(\alpha_9 - \alpha_8) + g^2\alpha_4 \\ \Delta g_2^{WW} &= 2c_W^2\Delta g_1^{\gamma Z} + 2g^2(\alpha_9 - \alpha_8) - g^2(\alpha_4 + 2\alpha_5) \\ h^{ZZ} &= 2g^2[\alpha_4 + \alpha_5 + 2(\alpha_6 + \alpha_7 + \alpha_{10})] \end{aligned} \quad (3.77)$$

where (oblique corrections )

$$\delta_Z = \frac{\beta_1 + g'^2\alpha_1}{c_W^2 - s_W^2} \quad (3.78)$$

### 3.3 Measurement strategy

The measurement strategy is at the same time straight forward and challenging. One should start with parameters that are already existing within the standard model and that are well measured. After that natural way of proceeding is to measurement of triple gauge couplings and in the final step one could perform the analysis of quartic couplings. As always things are not so straight forward as expected due to the shifts of the triple couplings from the quartic ones there is a need of simulations fit to all parameter of the effective Lagrangian in order to get a consistent set of numbers. The non separability of this procedure can be demonstrated through the Table.3.2 where the contribution of particular coupling to the given

vertex is labeled. Vertices  $WW\gamma$  and  $WWZ$  are exploited in processes  $e^+e^- \rightarrow W^+W^-$  and  $e^+e^- \rightarrow e^\pm\nu W^\mp$  for measurement of triple couplings. For the remaining vertices we can see that there is also contribution of  $\alpha_1$  and  $\alpha_3$  that contribute the triple gauge couplings. Thus it is essential to know the triple coupling with the precision that will allow correct calculation of the matrix elements for the sensitive processes and in the same time correct extraction of the limits to the quartic couplings.

One should cover all the parameters of the chiral Lagrangian. Radiative correction to the masses and couplings of the gauge bosons can be absorbed into tree parameters. The relations of the S,T,U parameterization and coupling constants of the effective Lagrangian are:

$$\Delta S = -16\pi\alpha_1 \quad \Delta T = 2\beta_1/\alpha_{QED} \quad \Delta U = -16\pi\alpha_8 \quad (3.79)$$

S,T,U are defined with the SM expectation subtracted so that  $S=T=U=0$  in the SM per definition. Values are well constrained by LEP, SLD and Tevatron experiments.

Next set of parameters are  $\alpha_2, \alpha_3, \alpha_9$  that contribute to the trilinear couplings. Measurement of this couplings is favorable due to the vertices appearing in the processes of the highest cross section (single W and W and Z pair production) almost without SM background diagrams, and the coupling can be determined with excellent precision from W-pair production.

After that one can proceed to the analysis of the remaining parameters  $\alpha_4, \alpha_5, \alpha_6, \alpha_7, \alpha_{10}$ . Where first two  $\alpha_4, \alpha_5$  conserve isospin symmetry, and other three violate. Thus In the analysis we assumed that the parameters except ones we are interested are determined with precision well beyond one that will interfere with quartic coupling determination.

Extraction of the quartic coupling based the direct measurement can rely on three

- vector boson scattering - that is favorable due to cross section rising with energy, but the effective scattering energy is significantly smaller due to the large fraction of energy carried away by  $e$  or  $\nu$ . Disadvantage is also relatively small ( $\sim fb$ ) cross section that is requiring large integrated luminosity and excellent detector performance to eliminate background and separate channels.
- triple vector boson production- cross section is falling with energy thus making it a preferred process for initial constraining of the coupling at first stage of the ILC (max 500GeV). It also suffers from  $\sim fb$  cross section and fact that only two processes  $e^+e^- \rightarrow WWZ, ZZZ$  contain quartic couplings through the linear combination making impossible simultaneous determination of all 5 couplings without additional information or assumptions.
- rescattering in vector boson pair production- computation of the effects is theoretically challenging and unfortunately only  $J=1$  amplitude is accessible.

In order to obtain consistent set of values for the couplings one should not consider mentioned items as separate measurement. Final word can be sad only after processing all sources of information and a combined fit like those done by LEP electroweak group.

After performing the analysis one most general way possible it is of interest to put the result into framework of possible physics scenario. Since it is expected that we see only "low energy" effects of the underlying physics Historically interpretation of the reachable sensitivities was in the value of the cutoff scale i.e. scale where our picture starts to be predictive and new phenomena sets one. Dangers of such approach and well known [52] and we will see on the example of this measurement can be significantly off leading to the wrong conclusions. Thus result will be interpreted within possible physics scenario of a to be resonance trying to demonstrate attempt of the combined fit by incorporating measurements of the quartic

Table 3.2: Chiral couplings involved in the triple and quartic gauge boson vertices. Sensitivity to a coupling is marked with ★.

vertex	$\alpha_1$	$\alpha_2$	$\alpha_3$	$\alpha_4$	$\alpha_5$	$\alpha_6$	$\alpha_7$	$\alpha_8$	$\alpha_9$	$\alpha_{10}$	$\alpha_{11}$	$\beta_1$
$WW\gamma$	★	★	★					★	★			
$WWZ$	★	★	★					★	★		★	★
$ZZWW$	★		★		★		★					★
$ZWZW$	★		★	★		★						★
$Z\gamma WW$	★		★									★
$ZZZZ$				★	★	★	★			★		

couplings from triple weak boson production [52] and measurement of triple gauge couplings [52]. Note that this is still to some way inconsistent choice since for authors (including me) have taken to some extent different and usually most favorable conditions for their measurement with total luminosity available only in optimistic experimental situation. Together with this one should take into account that only hadronic decay channels of the weak bosons were considered, leading to the reduction of the available data sample to  $\approx 0.5$  in weak boson scattering and W pair production and  $\approx 0.35$  in the triple weak boson production. This leaves the room for further improvements in the order of 1-1.4(1.7) just from the statistics assuming equivalent sensitivity and background suppression in the remaining channels.

### 3.4 Resonances

Notation remark (g couplings conserve isospin while h and k violate it by one and two units respectively.)

#### 3.4.1 Scalar singlet

The state is the generalization of a Higgs resonance. It case two independent linear couplings  $g_\sigma$  and  $h_\sigma$ . The latter violates isospin. Lagrangian is

$$\mathcal{L}_\sigma = -\frac{1}{2}[\sigma(M_\sigma^2 + \partial^2)\sigma + 2\sigma j] \quad (3.80)$$

where

$$j = -\frac{g_\sigma v}{2} \mathbf{tr} \mathbf{V}_\mu \mathbf{V}^\mu - \frac{h_\sigma v}{2} (\mathbf{tr} \mathbf{T} \mathbf{V}_\mu)^2 \quad (3.81)$$

Integrating out  $\sigma$  one gets :

$$\begin{aligned} \alpha_4 &= \alpha_6 = 0 \\ \alpha_5 &= g_\sigma^2 \left( \frac{v^2}{8M_\sigma^2} \right), \\ \alpha_7 &= 2g_\sigma h_\sigma \left( \frac{v^2}{8M_\sigma^2} \right), \\ \alpha_{10} &= h_\sigma^2 \left( \frac{v^2}{8M_\sigma^2} \right) \end{aligned} \quad (3.82)$$

and in the high-mass limit, the width of the resonance is

$$\Gamma_\sigma = \frac{g_\sigma^2 + \frac{1}{2}(g_\sigma + 2h_\sigma)^2}{16\pi} \left( \frac{M_\sigma^3}{v^2} \right) \quad (3.83)$$

that includes decay channels to WW and ZZ.

### 3.4.2 Scalar triplet

The Lagrangian is

$$\mathcal{L}_\pi = -\frac{1}{4}\text{tr}\{\pi(M_\pi^2 + \mathbf{D}^2)\pi + 2\pi\mathbf{j}\} \quad (3.84)$$

with

$$\mathbf{j} = \frac{h_\pi v}{2}\mathbf{V}_\mu\text{tr}\{\mathbf{T}\mathbf{V}^\mu\} + \frac{h'_\pi v}{2}\mathbf{T}\text{tr}\{\mathbf{V}_\mu\mathbf{V}^\mu\} + \frac{k_\pi v}{2}\mathbf{T}(\text{tr}\{\mathbf{T}\mathbf{V}_\mu\})^2 \quad (3.85)$$

that leads to

$$\begin{aligned} \alpha_4 &= 0 \\ \alpha_5 &= 2h'^2_\pi\left(\frac{v^2}{16M_\pi^2}\right) \\ \alpha_6 &= h^2_\pi\left(\frac{v^2}{16M_\pi^2}\right) \\ \alpha_7 &= 2h'_\pi(h_\pi + 2k_\pi)\left(\frac{v^2}{16M_\pi^2}\right) \\ \alpha_{10} &= 4k_\pi(h_\pi + k_\pi)\left(\frac{v^2}{16M_\pi^2}\right) \end{aligned} \quad (3.86)$$

Partial widths for the decay into vector boson pairs are different for charged and neutral pions.

$$\begin{aligned} \Gamma_{\pi^\pm} &= \frac{\frac{1}{4}h_\pi^2}{16\pi}\left(\frac{M_\pi^3}{v^2}\right) \\ \Gamma_{\pi^0} &= \frac{h'^2_\pi\frac{1}{4}(h_\pi + h'_\pi + 2k_\pi)^2}{16\pi}\left(\frac{M_\pi^3}{v^2}\right) \end{aligned} \quad (3.87)$$

### 3.4.3 Scalar quintet

The Lagrangian has the form

$$\mathcal{L}_\phi = -\frac{1}{4}\text{tr}\{\phi(M_\phi^2 + \mathbf{D}^2)\phi + 2\phi\mathbf{j}\} \quad (3.88)$$

with

$$\begin{aligned} \mathbf{j} &= -\frac{g_\phi v}{2}\mathbf{V}_\mu \otimes \mathbf{V}^\mu - \frac{h_\phi v}{2}(\mathbf{T} \otimes \mathbf{V}_\mu + \mathbf{V}_\mu \otimes \mathbf{T})\text{tr}\{\mathbf{T}\mathbf{V}^\mu\} \\ &\quad -\frac{h'_\phi v}{2}\mathbf{T} \otimes \mathbf{T}\text{tr}\{\mathbf{V}_\mu\mathbf{V}^\mu\} - \frac{k_\phi v}{2}\mathbf{T} \otimes \mathbf{T}(\text{tr}\{\mathbf{T}\mathbf{V}^\mu\})^2 \end{aligned} \quad (3.89)$$

and contributions to the coupling

$$\begin{aligned}
\alpha_4 &= g_\phi^2 \left( \frac{v^2}{16M_\phi^2} \right) \\
\alpha_5 &= 4h_\phi'^2 \left( \frac{v^2}{16M_\phi^2} \right) \\
\alpha_6 &= h_\phi^2 (2g_\phi + h_\phi) \left( \frac{v^2}{16M_\phi^2} \right) \\
\alpha_7 &= 2h_\phi' (g_\phi + 2h_\phi + 4k_\phi) \left( \frac{v^2}{16M_\phi^2} \right) \\
\alpha_{10} &= (h_\phi^2 + 4k_\phi (g_\phi + 2h_\phi + 2k_\phi)) \left( \frac{v^2}{16M_\phi^2} \right)
\end{aligned} \tag{3.90}$$

with resonance widths

$$\begin{aligned}
\Gamma_{\phi^{\pm\pm}} &= \frac{g_\phi^2}{64\phi} \left( \frac{M_\phi^3}{v^2} \right) \\
\Gamma_{\phi^\pm} &= \frac{(g_\phi + h_\phi)^2}{64\phi} \left( \frac{M_\phi^3}{v^2} \right) \\
\Gamma_{\phi^0} &= \frac{(g_\phi - 4h_\phi')^2 + 2(g_\phi + 2h_\phi + 2h_\phi' + 4k_\phi)^2}{3 \cdot 64\phi} \left( \frac{M_\phi^3}{v^2} \right)
\end{aligned} \tag{3.91}$$

#### 3.4.4 Vector singlet

$$\begin{aligned}
\beta_1 &= h_\omega^2 \left( \frac{v^2}{2M_\omega^2} \right)^2 \\
\alpha_1 = \alpha_2 = \alpha_4 = \alpha_7 &= h_\omega^2 \left( \frac{v^2}{2M_\omega^2} \right)^2 \\
\alpha_3 &= h_\omega k_\omega \left( \frac{v^2}{2M_\omega^2} \right)^2 \\
\alpha_5 = \alpha_6 = \alpha_8 &= -h_\omega^2 \left( \frac{v^2}{2M_\omega^2} \right)^2 \\
\alpha_9 &= -h_\omega (h_\omega + k_\omega) \left( \frac{v^2}{2M_\omega^2} \right)^2 \\
\alpha_{10} &= 0 \\
\alpha_1^\lambda &= -h_\omega l_\omega \left( \frac{v^2}{2M_\omega^2} \right)^2 \\
\alpha_2^\lambda = \alpha_5^\lambda &= h_\omega l_\omega \left( \frac{v^2}{2M_\omega^2} \right)^2 \\
\alpha_3^\lambda = \alpha_4^\lambda &= 0
\end{aligned} \tag{3.92}$$

$$\Gamma_\omega = \frac{h_\omega^2 + \frac{1}{2}l_\omega^2}{48\pi} M_\omega \tag{3.93}$$

### 3.4.5 Vector triplet

$$\begin{aligned}
\beta_1 &= 4h_\rho^2(g_\rho + h_\rho)\frac{v^2}{2M_\rho^2} - (g_\rho + 2h_\rho)^2\frac{v^2\Delta M_\rho^2}{2M_\rho^4} \\
\alpha_1 &= (g_\rho + 2h_\rho)^2\left(\frac{v^2}{2M_\rho^2}\right)^2 \\
\alpha_2 &= [-g_\rho(g_\rho(1 - \mu'_\rho) + 2k_\rho) + 4h_\rho^2]\left(\frac{v^2}{2M_\rho^2}\right)^2 \\
\alpha_3 &= (g_\rho + 2h_\rho)[g_\rho(1 + \mu_\rho) + k''_\rho]\left(\frac{v^2}{2M_\rho^2}\right)^2 \\
\alpha_4 &= -\alpha_5 = (g_\rho - 2h_\rho)^2\left(\frac{v^2}{2M_\rho^2}\right)^2 \\
\alpha_6 &= -\alpha_7 = 8g_\rho h_\rho\left(\frac{v^2}{2M_\rho^2}\right)^2 \\
\alpha_8 &= -4h_\rho(g_\rho + h_\rho)\left(\frac{v^2}{2M_\rho^2}\right)^2 \\
\alpha_9 &= -[(2h_\rho + k''_\rho)(g_\rho + 2h_\rho) + 2h_\rho(k'_\rho + g_\rho\mu_\rho)]\left(\frac{v^2}{2M_\rho^2}\right)^2 \\
\alpha_{10} &= 0
\end{aligned} \tag{3.94}$$

$$\begin{aligned}
\alpha_1^\lambda &= -[(g_\rho + 2h_\rho)(l_\rho + 2l''_\rho) + 2g_\rho l_\rho]\left(\frac{v^2}{2M_\rho^2}\right)^2 \\
\alpha_2^\lambda &= [(g_\rho + 2h_\rho)(l_\rho + 2l''_\rho) - \frac{c_W}{s_W}g_\rho l'_\rho]\left(\frac{v^2}{2M_\rho^2}\right)^2 \\
\alpha_3^\lambda &= -(g_\rho + 2h_\rho)l_\rho\left(\frac{v^2}{2M_\rho^2}\right)^2 \\
\alpha_4^\lambda &= -\frac{c_W}{s_W}(g_\rho + 2h_\rho)l'_\rho\left(\frac{v^2}{2M_\rho^2}\right)^2 \\
\alpha_5^\lambda &= -(g_\rho + 2h_\rho)l''_\rho\left(\frac{v^2}{2M_\rho^2}\right)^2
\end{aligned} \tag{3.95}$$

$$\begin{aligned}
\Gamma_{\rho^\pm} &= \frac{(g_\rho + 2h_\rho)^2 + 2l_\rho^2 + \frac{1}{2}l'^2_\rho}{48\pi}M_\rho \\
\Gamma_{\rho^0} &= \frac{(g_\rho - 2h_\rho)^2 + 2(l_\rho + 2l''_\rho)^2}{48\pi}M_\rho
\end{aligned} \tag{3.96}$$

### 3.4.6 Tensor singlet

$$\begin{aligned}
\alpha_4 &= g_f^2 \left( \frac{v^2}{8M_f^2} \right) \\
\alpha_5 &= -\frac{g_f^2}{4} \left( \frac{v^2}{8M_f^2} \right) \\
\alpha_6 &= 2g_f h_f \left( \frac{v^2}{8M_f^2} \right) \\
\alpha_7 &= -\frac{g_f h_f}{2} \left( \frac{v^2}{8M_f^2} \right), \\
\alpha_{10} &= \frac{3h_f^2}{2} \left( \frac{v^2}{8M_f^2} \right)
\end{aligned} \tag{3.97}$$

$$\Gamma_f = \frac{g_f^2 + \frac{1}{2}(g_f + 2h_f)^2}{16\pi} \left( \frac{M_f^3}{30v^2} \right) \tag{3.98}$$

where two terms in the numerator correspond to the partial widths to WW and ZZ, respectively.

### 3.4.7 Tensor triplet

$$\begin{aligned}
\alpha_4 &= h_a'^2 \left( \frac{v^2}{8M_a^2} \right) \\
\alpha_5 &= -\frac{h_a^2}{4} \left( \frac{v^2}{8M_a^2} \right) \\
\alpha_6 &= \frac{1}{4} \left( \frac{1}{2}h_a^2 + 4h'_a(h_a + 2k_a) \right) \left( \frac{v^2}{8M_a^2} \right) \\
\alpha_7 &= \frac{1}{4} (h_a^2 - h'_a(h_a + 2k_a)) \left( \frac{v^2}{8M_a^2} \right) \\
\alpha_{10} &= \frac{3k_a(h_a + k_a)}{2} \left( \frac{v^2}{8M_a^2} \right)
\end{aligned} \tag{3.99}$$

and for the widths

$$\begin{aligned}
\Gamma_{a^\pm} &= \frac{h_a^2}{64\pi} \left( \frac{M_a^3}{30v^2} \right) \\
\Gamma_{a^0} &= \frac{h_a'^2 \frac{1}{2} (h_a + h'_a + 2k_a)^2}{16\pi} \left( \frac{M_a^3}{30v^2} \right)
\end{aligned} \tag{3.100}$$

### 3.4.8 Tensor quintet

$$\begin{aligned}
\alpha_4 &= \left(\frac{1}{4}g_t^2 + 4h_t'^2\right) \left(\frac{v^2}{16M_t^2}\right) \\
\alpha_5 &= \left(\frac{1}{2}g_t^2 - h_t'^2\right) \left(\frac{v^2}{16M_t^2}\right) \\
\alpha_6 &= \left(\frac{1}{2}h_t^2(g_t + \frac{1}{2}h_t) + 4h_t'(g_t + h_t + 2k_t)\right) \left(\frac{v^2}{16M_t^2}\right) \\
\alpha_7 &= \left(h_t^2(g_t + \frac{1}{2}h_t) - h_t'(g_t + h_t + 2k_t)\right) \left(\frac{v^2}{16M_t^2}\right) \\
\alpha_{10} &= 3\left(\frac{1}{4}h_t^2 + k_t(g_t + h_t + 2k_t)\right) \left(\frac{v^2}{16M_t^2}\right)
\end{aligned} \tag{3.101}$$

where widths are

$$\begin{aligned}
\Gamma_{t^{\pm\pm}} &= \frac{g_t^2}{64\pi} \left(\frac{M_t^3}{30v^2}\right) \\
\Gamma_{t^\pm} &= \frac{(g_t + h_t)^2}{64\pi} \left(\frac{M_t^3}{30v^2}\right) \\
\Gamma_{t^0} &= \frac{1}{3} \frac{(g_t - 4h_t')^2 + 2(g_t + 2h_t + 2h_t' + 4k_t)^2}{64\pi} \left(\frac{M_t^3}{30v^2}\right)
\end{aligned} \tag{3.102}$$



# Chapter 4

## Analysis and Results

### 4.1 Direct measurement of quartic couplings

#### 4.1.1 Processes

In order to estimate sensitivity to quartic couplings we will consider all possible scattering processes as they are shown in Table. 4.1. There are four such processes in  $e^+e^-$  collisions and three when machine is running in  $e^-e^-$  mode. We will consider  $e^-e^-$  channels also this mode is not in the baseline in order to test possible impact of different physics program i.e. if need to run  $e^-e^-$  mode was established in first phase of the project.  $e^+e^-$  channels are favored not only because of larger luminosity per unit of time but because of existence of  $W^+W^- \rightarrow ZZ$  process, that is essential for simultaneous measurement of isospin conserving ( $\alpha_4, \alpha_5$ ) and isospin braking couplings ( $\alpha_6, \alpha_7$ ). For this role  $WZ$  channels are not suitable due to the low sensitivity. Only channel that can reach  $\alpha_{10}$  is  $ZZ \rightarrow ZZ$  that appears in both machine running modes but with a tiny cross section measurement is very challenging. Role of the polarization is extensively discussed at several places [59], and we are assuming that electron beam has 80% left polarization and positron beam 40% right polarization. Although positron polarization is not guaranteed in the baseline design we consider 40% as an conservative estimate that should be reachable at this energy without penalty in available luminosity.

In order to preserve internal consistency of analysis both the signal and the background processes were generated with Wizard [61] using O'Mega [62] matrix elements calculation. Initial state radiation is taken into account as implemented in the generator (in collinear approximation). Obtained cross-section for hadronic final states are shown in Table.4.2 **for the head on** collisions at center of mass energy 1TeV. Additional generation cuts were introduces for some background processes in order to keep number of events within technically feasible number and at the same time do not disturb physics. The cuts are: for  $e^-\nu W^-$  and  $e^-e^-Z$  channels  $M(q\bar{q}) > 130GeV$  and for the same channel in  $e^+e^-$  plus continuum production

Table 4.1: Sensitivity to quartic anomalous couplings for all possible scattering processes. Sensitivity is marked with +.

$e^+e^- \rightarrow$	$e^-e^- \rightarrow$	$\alpha_4$	$\alpha_5$	$\alpha_6$	$\alpha_7$	$\alpha_{10}$
$W^+W^- \rightarrow W^+W^-$	$W^-W^- \rightarrow W^-W^-$	+	+			
$W^+W^- \rightarrow ZZ$		+	+	+	+	
$W^\pm Z \rightarrow W^\pm Z$	$W^-Z \rightarrow W^-Z$	+	+	+	+	
$ZZ \rightarrow ZZ$	$ZZ \rightarrow ZZ$	+	+	+	+	+

Table 4.2: Generated processes and cross sections of signal and background for  $\sqrt{s} = 1\text{TeV}$ , polarization 80% left for electron and 40% right for positron beam

Channel	$\sigma[fb]$	Channel	$\sigma[fb]$
$e^+e^- \rightarrow \nu_e\bar{\nu}_e W^+W^- \rightarrow \nu_e\bar{\nu}_e q\bar{q}q\bar{q}$	23.19	$e^-e^- \rightarrow \nu_e\bar{\nu}_e W^-W^- \rightarrow \nu_e\bar{\nu}_e q\bar{q}q\bar{q}$	27.964
$e^+e^- \rightarrow \nu_e\bar{\nu}_e ZZ \rightarrow \nu_e\bar{\nu}_e q\bar{q}q\bar{q}$	7.624	$e^-e^- \rightarrow e^-e^- W^-Z \rightarrow e^-e^- q\bar{q}q\bar{q}$	80.2
$e^+e^- \rightarrow \nu\bar{\nu} q\bar{q}q\bar{q}$ (3V contribution)	9.344	$e^-e^- \rightarrow e^-e^- ZZ \rightarrow e^-e^- q\bar{q}q\bar{q}$	3.16
$e^+e^- \rightarrow \nu_e WZ \rightarrow \nu_e q\bar{q}q\bar{q}$	132.3	$e^-e^- \rightarrow e^-e^- W^+W^- \rightarrow e^-e^- q\bar{q}q\bar{q}$	443.9
$e^+e^- \rightarrow e^+e^- ZZ \rightarrow e^+e^- q\bar{q}q\bar{q}$	2.09	$e^-e^- \rightarrow e^-e^- t\bar{t} \rightarrow e^-e^- X$	0.774
$e^+e^- \rightarrow e^+e^- W^+W^- \rightarrow e^+e^- q\bar{q}q\bar{q}$	414.6	$e^-e^- \rightarrow ZZ \rightarrow q\bar{q}q\bar{q}$	232.875
$e^+e^- \rightarrow t\bar{t} \rightarrow X$	331.768	$e^-e^- \rightarrow e^-e^- W^- \rightarrow e^-e^- q\bar{q}$	235.283
$e^+e^- \rightarrow W^+W^- \rightarrow q\bar{q}q\bar{q}$	3560.108	$e^-e^- \rightarrow e^-e^- Z \rightarrow e^-e^- q\bar{q}$	125.59
$e^+e^- \rightarrow ZZ \rightarrow q\bar{q}q\bar{q}$	173.221		
$e^+e^- \rightarrow e\nu W \rightarrow e\nu q\bar{q}$	279.588		
$e^+e^- \rightarrow e^+e^- Z \rightarrow e^+e^- q\bar{q}$	134.935		
$e^+e^- \rightarrow q\bar{q} \rightarrow X$	1637.405		

$e^+e^- \rightarrow q\bar{q}$  of  $M(q\bar{q}) > 140\text{GeV}$ . All 2,4 and 6 fermion final states were generated directly (there is no on-shell production and subsequent decay) so natural width of the weak bosons is properly taken into account. Events were generated with SM values for the quartic coupling i.e.  $\alpha_i \equiv 0$ ,  $i \in \{4, 5, 6, 7, 10\}$ . Triple couplings were also set to SM values since we assume that even if the deviations to the SM value are observed they are measured with precision that is well above one that we can reach for the quartic ones so taking any well known number for value of triple couplings is equivalent.

Fragmentation and hadronization of quark final states was done by Pithya [71] before passing the event to the detector simulation. Detector response was simulated with Simdet [63], fast parametric Monte Carlo program based on the full detector simulation of TESLA detector [7].

### 4.1.2 Observable

There are several observable that are sensitive to the deviation of chiral coupling from their SM values. First is the total cross section. Example for that dependence are shown in Fig.4.1 for most important processes. From the low energy measurements values of the couplings are already constrained<sup>1</sup> to the level that total variation of the cross section is on the order of 1% asking for very good cross section calculation. Due to the dependence of all processes on at least two couplings cross section cannot be used as an exclusive variable since the solution of the problem  $\sigma(\alpha_i) = \sigma_{SM}$  is ellipse in the parameter plane (two dimensional case) or hypersurface in parameter space (three and more dimensional case). This point is important since it stresses the fact that **this is not a simple counting experiment!** Other variables are needed to brake the symmetry of the solution. Since expected new effects should manifest themselves on the scale well above direct reach of the collider and we are looking only at lower energy remnant of that mechanism the closer we are to that scale effects should be larger. Thus mass of the event is another sensitive variable. Unfortunate is that in all scattering processes we have two leptons that are carrying significant fraction of the momentum away and reducing the effective

<sup>1</sup>putting a side all more or less founded complains against those numbers

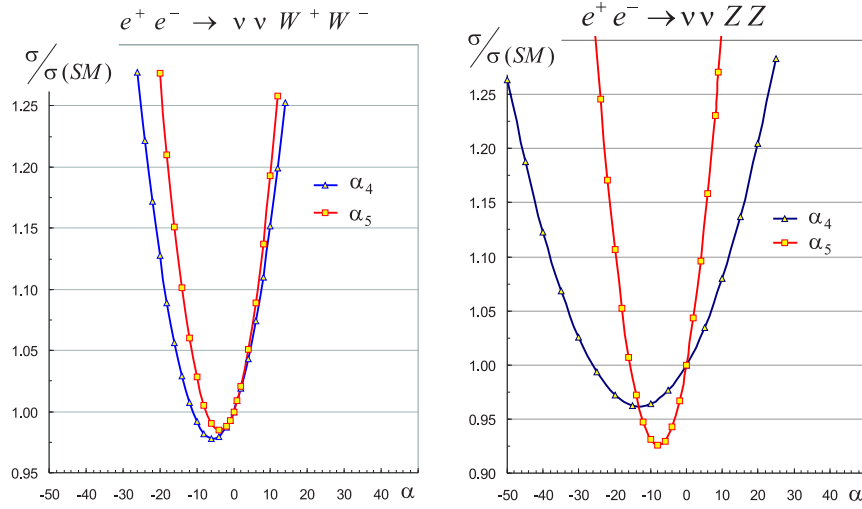


Figure 4.1: Cross section dependence on quartic couplings for  $\nu\nu W^+W^-$  process on the left, and  $\nu\nu ZZ$  on the right.

center of mass energy. Events with high mass should be more sensitive to the possible deviation in quartic couplings from SM values. Information about SBS should be carried primarily with longitudinally polarized weak bosons and their interaction thus production and decay angles are also sensitive variables. Since there is no distinction between weak bosons or quark anti quark these distributions are folded reducing the sensitivity to and extent. Sensitivity to mentioned variables is demonstrated on Fig.4.2 with the ratio of mentioned distributions for  $\alpha_4 = 4$  to the SM ones for  $\nu\nu W^+W^-$  process.

## 4.2 Event selection

Since we are dealing with several processes with significant similarities common analysis issues and essential steps for the analysis will be explained once for all the processes in question. Event selection was largely based on the previous analysis [83] that was done at 800GeV so there will be some referring to the 800GeV-1TeV differences, and all the selection criteria are revisited and changed if necessary. After that overview of applied selection criteria will be presented with summary of obtained results.

### 4.2.1 Jet pairing

During the second run of the LEP experiment significant problem for the analysis was the jet pairing. This problem has risen out of the several reasons running close to the threshold for the weak boson pair production leads to the jets with no or very small burst and then with jets with large opening angles ([65]) that are prone to the reassignment of particles with the jet algorithm. Appropriate complex procedures were developed for dealing with such effects [66]. At higher energies we are in much better situation since jets are more collimated due to the significant boost with almost no back flying particles making easier task for the jet finding algorithm. Second important change is the precision of the measurement of the momenta and the directions of the particles reducing the overall smearing of the topology.

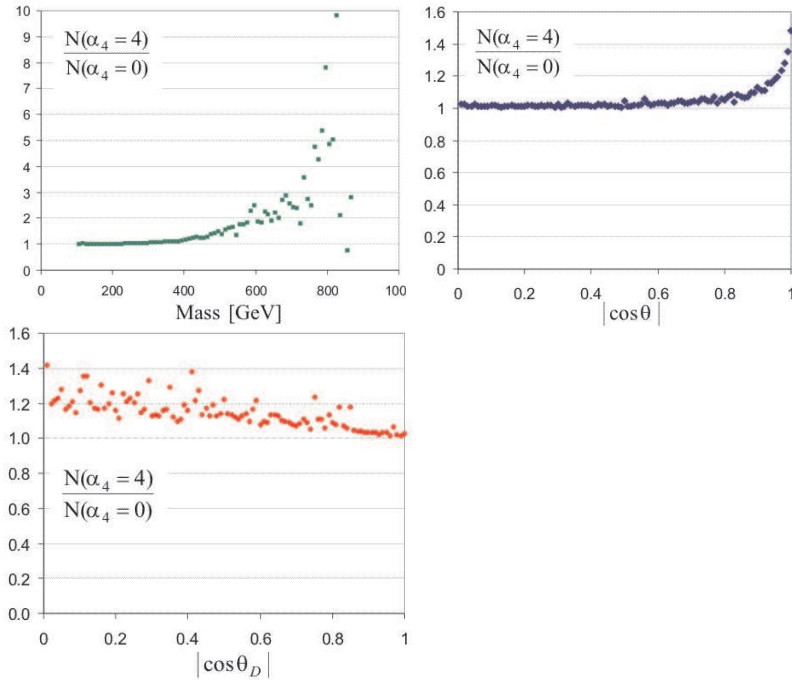


Figure 4.2: Ratio of event mass, production and decay angles distributions for  $\nu\nu W^+W^-$  process and  $\alpha_4 = 4$  to the SM ones.

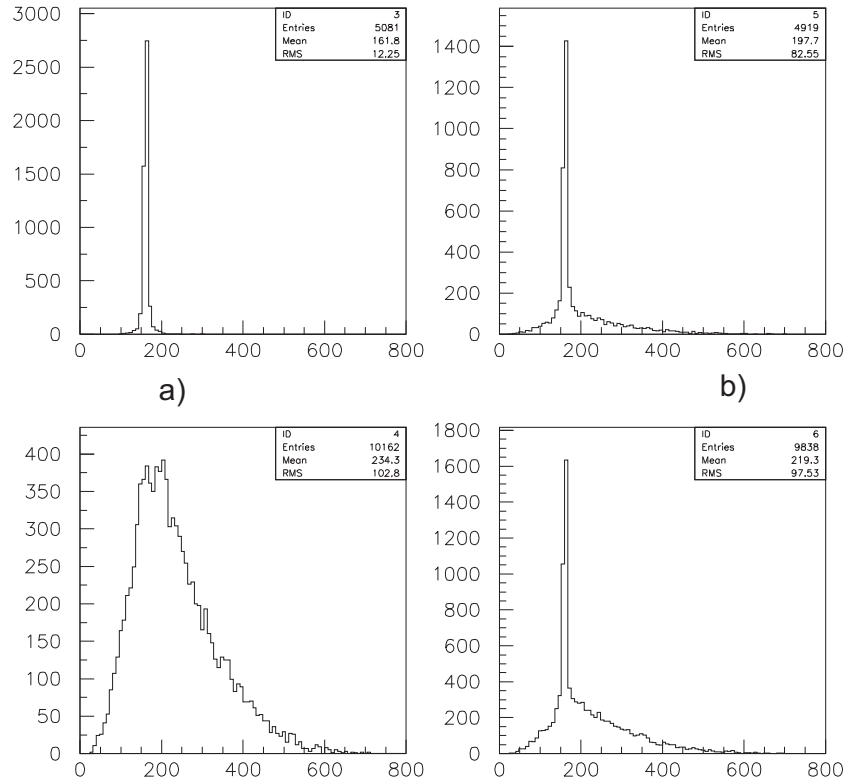


Figure 4.3: Distribution of masses for  $W^-$  pairs in case of quark final state without ambiguity a), and with b) in case of right combination up and wrong combination below.

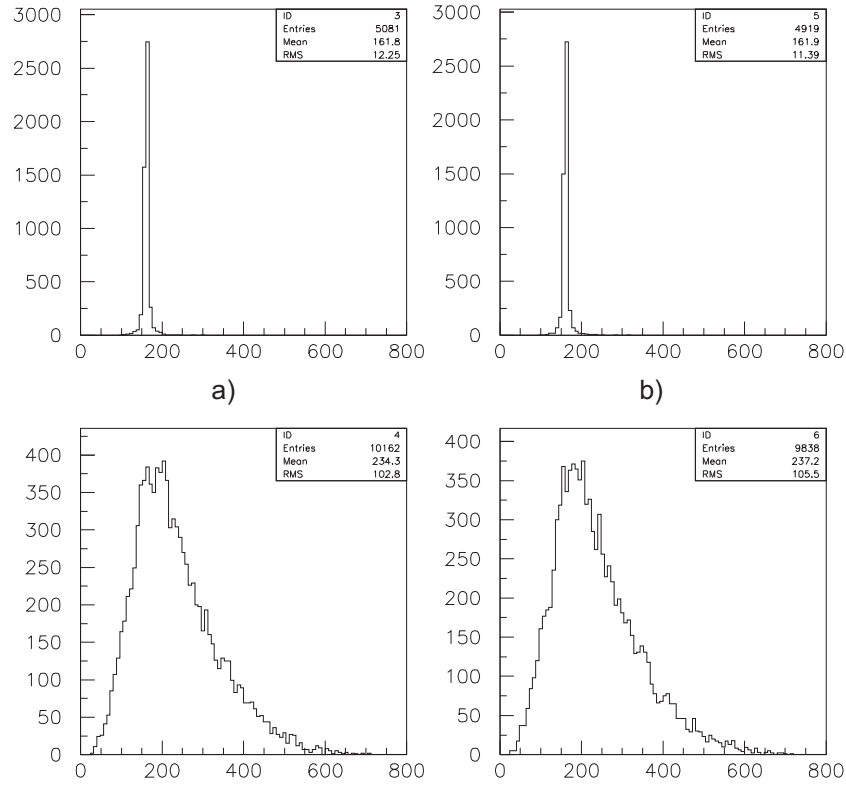


Figure 4.4: Distribution of masses for  $W^-$  pairs in case of quark final state without ambiguity a), and with b) in case of right combination up and wrong combination below after correction.

$$W^-W^- \rightarrow \begin{array}{cccc} q & \bar{q} & q & \bar{q} \\ 1 & 2 & 3 & 4 \end{array} \quad (4.1)$$

Optimal pairing is anyhow still a important step in any multi jet final state analysis. Way to the optimal pairing is to know the true right pairing and then to develop the procedure to maximize the right output. Since Whizard is N-fermion generator and due to the lack of the color information there were tiny issues about the knowledge of the right quark color singlet pairs at the output. At the output we have four quarks, and lets enumerate them from 1 to 4 as in eq.4.1. In some of the final states like for  $W^-$  pairs like dUsC the right pairing is dU and sC, in some case like dUdU there is possibility that singles are not expected combination 1-2 and 3-4 but 1-4 and 2-3. In order to test this mass distributions were made for both final cases, in the way that expected “right” pairing (1-2,3-4) was put in one histogram and other two “wrong” combinations in another. This procedure was repeated for final states were ambiguity does not exist and in those were it is possible. In the Fig.4.3 findings are summarized. Case a) shows no ambiguity case with correct combination on upper and two other combination on lower plot. Case b) shows final state with ambiguity and lower plot clearly indicates that in half of the combination right pairing is 1-4 2-3. Using the information about the natural width of the mass distribution and it’s shape i.e. Bright-Wiegner it was possible to correct for this effect. In Fig.4.4 are same distribution after correction. Now they look absolutely similar. Correction procedure was used in all situations were ambiguity could have existed due to the specific treatment of the events i.e. their fragmentation calling Pithya routine PY4FRM with

pairing	mass window	+abs diff.	full	N right	eff[%]	$\sigma[GeV]$
original	3367	3266	2798	2730	97.57	3.33(10)
$\chi^2$	3954	3837	3262	3167	97.09	3.34(10)
gauss	5007	4892	4328	4127	95.36	3.46(9)
IBW $\Gamma = 5GeV$	4992	4870	4322	4121	95.35	3.45(9)
IBW $\Gamma = 4GeV$	4989	4863	4317	4117	95.37	3.45(9)
IBW $\Gamma = 3GeV$	4926	4855	4312	4114	95.41	3.44(9)

Table 4.3: Pairing method optimization for  $\nu$  channel

the flag to stick to the user defined pairing since the routine would use ordinary WW and ZZ pair production matrix elements otherwise. At this stage we have assured that we know the right quark pairs at the start. Now we will revisit the pairing criteria used in the TDR analysis, initial pairing condition was to us eq. 4.2.

$$Min(|M_i - M_V| |M_j - M_V|) \quad (4.2)$$

where  $M_i$  and  $M_j$  are masses of the jet pairs and  $M_V$  is mass of the weak boson (eider W or Z). Noticed disadvantage of the chosen criteria is that due to the structure of the function it strongly prefers one pair exact or very close to the nominal mass and the second can be almost anything. Three addition possible measures were introduced trying to remedy this kind of behavior. One is usual  $\chi^2$  measure as in eq.4.3

$$Min\left(\frac{(M_i - M_V)^2}{\sigma^2} + \frac{(M_j - M_V)^2}{\sigma^2}\right) \quad (4.3)$$

and two principally new exploiting excellent performance of the ILC detector <sup>2</sup>.

$$Min\left(\exp\left(\frac{M_i - M_V}{\sigma}\right)^2 \exp\left(\frac{M_j - M_V}{\sigma}\right)^2\right) \quad (4.4)$$

$$Min\left(\frac{(M_V^2 - M_i^2)^2 + M_V^2 \Gamma^2}{\Gamma^2} \frac{(M_V^2 - M_j^2)^2 + M_V^2 \Gamma^2}{\Gamma^2}\right) \quad (4.5)$$

Both are base on the fact that initial mass distribution of the weak boson defined by Bright-Wiegner shape ( $\Gamma_W = 2.124GeV$  and  $\Gamma_Z = 2.2952GeV$ ) is preserved by the detector resolution leading to the same distribution for probability density function of reconstructed jet pairs around nominal mass, understandable with higher width. Since this distribution is in fact in the transition region between the gauss and BW (natural and detector contribution to the final width are comparable) both dependences were tested. Condition from eq.4.4 we will call simply Gauss, and from eq.4.5 inverse bright-wiegner (IBW). Note that due to the structure of the functions both  $\chi^2$  and Gauss do not depend on the used  $\sigma$ , formally value of the function is scaled but the position of the minimum is not moved. For the IBW distribution this is not the case since width is entering on both sides of the fraction thus it is possible, although for small fraction of the events, that with different used width different pairing combination has the minimum of the function.

Test sample contains the 10000 events for the WW process.

In Tab.4.2.1 we summarize pairing optimization. All other selection cuts are applied except the cuts on the mass of the single weak bosons and pairs. Additional cuts are mass of one

<sup>2</sup>By detector performance always assume combined hardware and reconstruction software performance

$P_t$ mass [GeV]	2.0	2.1	2.2	2.3	2.4	2.5	2.6	2.7	2.8	2.9
duuu (dudd)	3	3	3	3	3	2	2	2	2	2
sccc	29	23	23	22	20	19	19	18	16	16
dubb	392	384	371	351	339	332	323	317	308	290

Table 4.4: Number of events passing the condition at least one jet with vertex mass above. Samples of 500 events with specified final state.

candidate should be  $65\text{GeV} < M_i < 88\text{GeV}$  called mass window in the table, difference between candidate masses should be  $|M_i - M_j| < 20\text{GeV}$  called absolute difference this cut is applied additionally to the mass window cut. Finally third cut is applied  $148\text{GeV} < M_i + M_j < 172\text{GeV}$ , together with previous two, and passed number of events is in column full. Using the true information number of event with correct pairing is calculated and is in column N right. Efficiency of correct pairing after the selection cuts is then calculated and the distribution is fitted with Gauss function plus second order polynome (to account for possible combinatorial background). Both new pairing conditions give significantly higher yield with minimal drop of 2% in correct pairing efficiency. Obtained width is for all methods is consistent within the fit errors and exactly with the prediction. Results for the Gaussian and IBW approach are statistically equivalent after applied cuts further on eq.4.5 was used as a pairing condition. Durham algorithm was used as a jet algorithm of the choice as it has shown best performance, as already concluded in extensive studies [67]. Tuning of the algorithm can affect efficiency only on the 1% level.

### 4.2.2 B tagging

For same fraction of interesting processes final states as well for the background expected excellent b-tagging capability of ILC detector [68] is valuable additional information for the separation of the signal and the background. In the fast simulation integrated tools allowed usage of the ZVTOP algorithm [70] for the b-tagging. Originally the final b-tag was made using the neural network that was trained at Zpole [69]. We have tried to keep the analysis bias free as possible thus usage of such network was not an option, as well as retraining the network with  $\sim 10^7$  events needed (that is larger than our total event sample). Instead of network only transverse momentum corrected vertex mass was used for b-tag. Event has positive b-tag if contains at least one jet with vertex of mass above  $M_{cut}$ . In order to determine needed cut value final states of  $W^\pm Z$  were divided to subsamples containing only light quark combinations, charm and strange, and sample with  $Z \rightarrow b\bar{b}$  decay as in Table.4.2.2 and range of  $M_{cut}$  from 2.0-2.9GeV was tested. Following original SLD result (as on Fig.4.5) and our test value of  $M_{cut} = 2.1\text{GeV}$  was chosen as appropriate that is giving 77% efficiency for identification and less than  $< 2.5\%$  of fakes. Importance of suppression for  $Z \rightarrow b\bar{b}$  channel is large due to the fact that increased amount of neutrinos in decay chain is shifting reconstructed mass to lower values increasing contamination within W mass window in respect to the amount anticipated on the base of reconstruction performance alone. It also aoes to suppers contamination of same final state from different processes like in  $e\nu W b\bar{b}$  case where we can have two paths, one form  $e^\pm \nu W^\mp Z \rightarrow e^\pm \nu W^\mp b\bar{b}$  and second from  $t\bar{t} \rightarrow W^+ W^- b\bar{b}$  that with one decay  $W^\pm \rightarrow e^\pm \nu$  leads to the same final state. Identification of b jets allows additional mass cut on the right combination of jets and elimination of SM background.

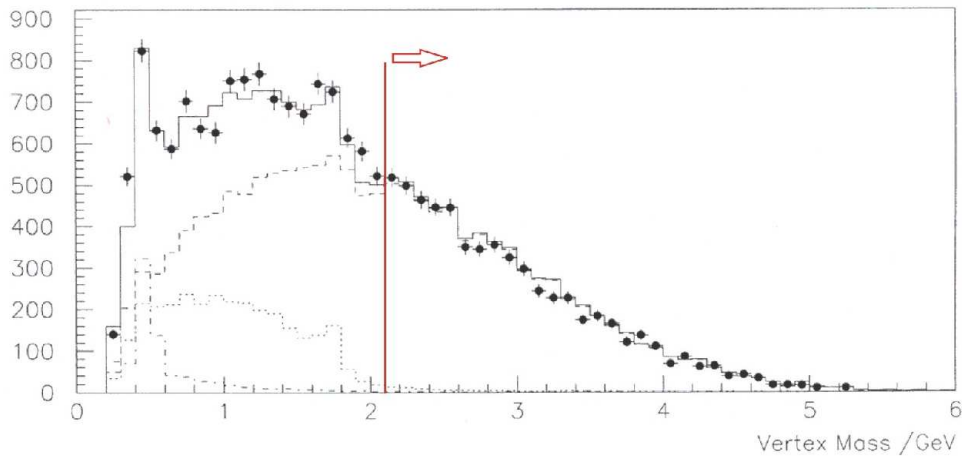


Figure 4.5:  $P_t$  corrected mass distribution, with the line and an error cut used in the analysis is marked.

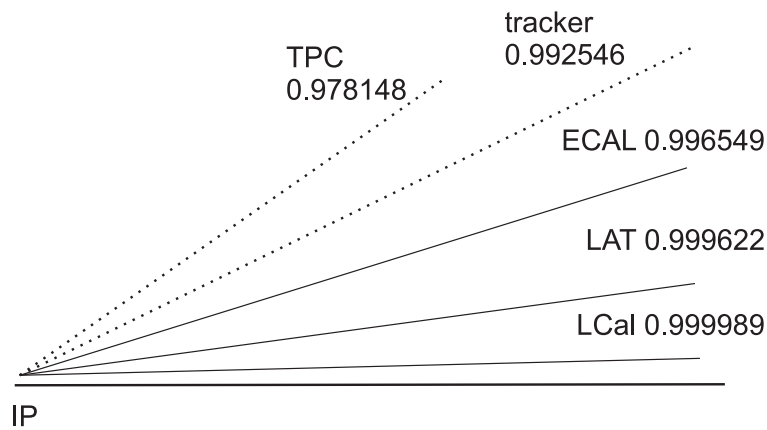


Figure 4.6: Angular coverage of detector elements as implemented in fast simulation. Numbers are cosines of the lowest angle covered by the region.

### 4.2.3 Forward region

All the processes under consideration can be splitted into two groups on the existence or nonexistence of lepton in the final state. This feature can be used to increase signal background separation and separation between signals. At high energies all distributions become increasingly forward peaked thus it is of significant importance to have reliable tag up to lowest possible angle. In Fig.4.6 we have a sketch of detector coverage in the forward region as implemented in fast simulation.

TPC edge was set to 12degrees that obviously assumes full vertex support. Tracking is assumed to work till 7 degrees. Below that we had part of the ECAL, LAT and LCal with their angular coverage as in TDR. So no charge information was available below 7 degrees plus below lower edge of the ECAL all measured particles were “identified” as photons (probably with raison that these are electromagnetic calorimeters). Detailed background studies done for that part of the detector at that time have shown that reconstruction thresholds for that

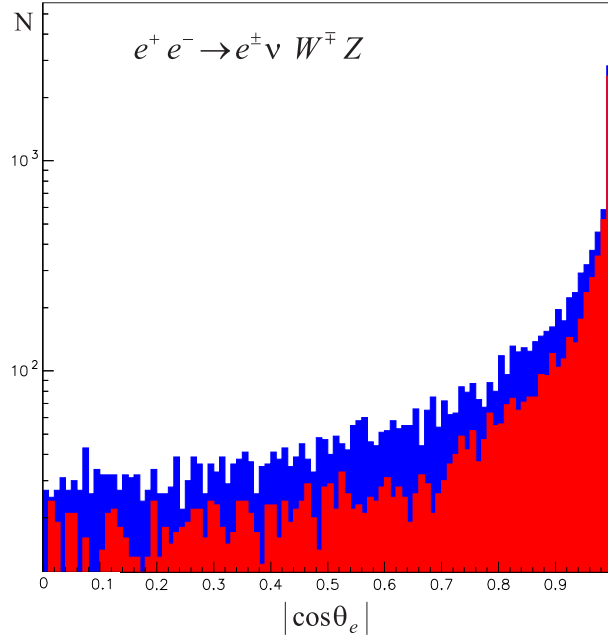


Figure 4.7: Angular dependence of tagged electrons (positrons) for  $e$  process at 800GeV (in blue) and 1TeV (in red).

region have been significantly higher [72] this was corrected by using more conservative cuts in the analysis. Due to the essential difference of information available in region covered by tracker and below two approaches were used in parallel. In the tracker high energy electrons were checked with cone isolation criterion. Cone with half opening angle  $\theta$  is constructed and energy within it is calculated  $E_{cone}$ . If the ratio of the energy in the cone  $E_{cone}/E_e$  is less than cut value this is assumed to be the isolated lepton we search for. For region below the tracker if measured energy is above some threshold detection of electron (positron) is assumed. Information on lepton existence was then used either for positive selection or background suppression. Increase in the center of mass energy increases sensitivity to the quartic couplings but at the same time reduces number of leptons that can be tagged even with such hermetic detector. This is demonstrated in Fig.4.7 where angular dependence for leptons in  $e^\pm\nu W^\mp Z$  process was shown in parallel for 800 GeV and 1TeV. One can notice depopulation of distribution in central region. And in fact there is 30% drop in number of tagged leptons even though total cross section rises.

There is an additional aspect of lepton identification. If this particle is not identified and continues to participate in the particle list passed to the jet finding algorithm it will distort jet creation and increase reconstruction width thus reduce overall selection efficiency. Not only that identification of the isolated leptons from the final state is helpful for the signal background separation. If this particle is reconstructed it is “hidden” between all other reconstructed particles. It is mandatory to find this particle, in cases when our signal contains it, and remove it from the list before we pass event to the jet finding algorithm. In case when signal does not contain lepton in the final state failure to remove it before jet finding will not be so important since such event will most probably be removed by other kinematic cuts. I hope that now it is understandable that changes in detector design as discussed before will have a negative impact on measurement of quartic couplings.

#### 4.2.4 Overview of selection criteria

$$e^-e^- \rightarrow \nu\nu W^-W^-$$

If one considers what distinct this from other signal channels that are two features . No leptons in final state and no b-quarks in the final state. Exactly from this general considerations selection starts. All reconstructed particles are checked for electrons (positrons) or highly energetic object in the region below the tracker. Some minimal electron energy must be taken as threshold for this consideration since existence of higher energy electrons within jets although not so probable is still possible. So lower energy for the electron cut is set to  $E_{ecut} > 18.0GeV$ . For tracker we construct a cone with half opening angle of 7.5 degrees and collect energy within it. Ratio of the energy in the cone  $E_{cone}$  and the energy of electron is made if

$$\frac{E_{cone}}{E_{e^\pm}} < 0.25 \quad (4.6)$$

we consider lepton isolated and reject the event. In low angle region that is not covered by tracker rejection was made only on the base of energy. If object is above 70GeV in LAT or corner region of ECAL, or above 100GeV in LCAL. If passed event is forced to 4 jets. B-tagging code is called and number of jets with vertex mass over 2.1GeV is counted. If any such found event is rejected. After weak preselection requiring that we have at least 7 charged tracks and 10 reconstructed objects kinematic variables are calculated. First the total visible momentum  $P$  of the event as usual vector sum

$$P_j = \sum p_j^i \quad j = x, y, z, E \quad (4.7)$$

from this we calculate transverse momentum and total mass

$$P_{tr} = \sqrt{P_1^2 + P_2^2} \quad , \quad M_{tot}^2 = P_4^2 - \sum_{i=1}^3 P_i^2 \quad (4.8)$$

missing energy simply by  $E_{miss} = 1TeV - P_4$   
and transverse energy and missing mass

$$E_{tr} = \sum E_i \sin \theta_i \quad , \quad M_{miss}^2 = E_{miss}^2 - \sum_{i=1}^3 P_i^2 \quad (4.9)$$

and absolute value for the cosine of missing momentum

$$\cos \theta_{miss} = \frac{Abs(P_3)}{|P|} \quad (4.10)$$

Following cuts values were used (if condition is satisfied event is accepted)  $P_{tr} > 35GeV$   $150 < E_{tr} < 600GeV$ ,  $M_{miss} > 200GeV$ ,  $E_{miss} > 200GeV$  and  $\cos \theta_{miss} < 0.99$ . For events that survived so far jet pairing is done using IBW function with  $\Gamma = 3GeV$  and final cuts on the mass variables were made. Mass window for W mass  $60 < M_W < 88GeV$ , cut on the sum of the two masses  $140 < M_{W1} + M_{W2} < 172GeV$  and constrain that reconstructed masses should not have large difference  $|M_{W1} - M_{W2}| < 20GeV$ . Numbers in the mass subscripts just label that there are two reconstructed W boson no ordering is done what so ever. For the events that have passed this final cuts sensitive variables were calculated and stored.

In Table.4.5 final numbers of events after explained selection is shown. Al the numbers in the table are estimates for  $1ab^{-1}$  although signal process is always processed with higher statistics (8x in this case). As one would expect the more similar background channel is to the signal the more we accept. One can wonder why have we accepted such numbers as final with signal to background of the order of 2 (2.08).

Table 4.5: Selection result for  $\nu\nu W^- W^-$ . Numbers are expected signal and background for luminosity of  $1ab^{-1}$

Channel	Number of events
$e^-e^- \rightarrow \nu_e\bar{\nu}_e W^- W^- \rightarrow \nu_e\bar{\nu}_e q\bar{q}q\bar{q}$	11937
$e^-e^- \rightarrow e^-\nu_e W^- Z \rightarrow e^-\nu_e q\bar{q}q\bar{q}$	4057
$e^-e^- \rightarrow e^-e^- ZZ \rightarrow e^-e^- q\bar{q}q\bar{q}$	0
$e^-e^- \rightarrow e^-e^- W^+ W^- \rightarrow e^-e^- q\bar{q}q\bar{q}$	255
$e^-e^- \rightarrow e^-e^- t\bar{t} \rightarrow e^-e^- X$	0
$e^-e^- \rightarrow e^-\nu_e W^- \rightarrow e^-\nu_e q\bar{q}$	1428
$e^-e^- \rightarrow e^-e^- Z \rightarrow e^-e^- q\bar{q}$	0

Table 4.6: Selection result for  $e^-\nu W^- Z$ . Numbers are expected signal and background for luminosity of  $1ab^{-1}$

Channel	Number of events
$e^-e^- \rightarrow \nu_e\bar{\nu}_e W^- W^- \rightarrow \nu_e\bar{\nu}_e q\bar{q}q\bar{q}$	8
$e^-e^- \rightarrow e^-\nu_e W^- Z \rightarrow e^-\nu_e q\bar{q}q\bar{q}$	16754
$e^-e^- \rightarrow e^-e^- ZZ \rightarrow e^-e^- q\bar{q}q\bar{q}$	8
$e^-e^- \rightarrow e^-e^- W^+ W^- \rightarrow e^-e^- q\bar{q}q\bar{q}$	631
$e^-e^- \rightarrow e^-e^- t\bar{t} \rightarrow e^-e^- X$	1
$e^-e^- \rightarrow e^-\nu_e W^- \rightarrow e^-\nu_e q\bar{q}$	881
$e^-e^- \rightarrow e^-e^- Z \rightarrow e^-e^- q\bar{q}$	4

$$e^-e^- \rightarrow e^-\nu W^- Z$$

In contrary to the previous channel here we are requesting that exactly one electron from the final state is detected by the detector. In the cone selection only minor change was made, threshold for electrons was lowered to  $16GeV$ . Following cuts values were used (if condition is satisfied event is accepted)  $P_{tr} > 30GeV$ ,  $M_{tot} > 185GeV$ ,  $E_{tr} < 450GeV$ ,  $\cos\theta_{miss} < 0.999$ . For events that survived so far jet pairing is done using Gauss function with  $\sigma_W = 3.3GeV$  and  $z = 3.6GeV$  and final cuts on the mass variables were made. Mass windows  $65 < M_W < 86GeV$  and  $82 < M_Z < 100GeV$ , cut on the sum of the two masses  $155 < M_W + M_Z < 186GeV$  and that fifth Fox-Wolfram moment is greater then  $FWmom(5) > 0.7$ . Resulting number of events are in the Table.4.6.

One can notice that all the background sources except eeWW and enuW channel are statistically insignificant. The ratio of signal to background is excellent but the channel is not too sensitive and only the events with electron within detector acceptance were used that significantly reduces effective cross section.

$$e^+e^- \rightarrow \nu\bar{\nu} W^+ W^-$$

Since this channel has same general characteristics as the equivalent in  $e^-e^-$  all selection criteria are kept the same. Only the value for required transverse momentum is increased in order to suppress larger amount of background  $P_t > 45GeV$ . Expected number of events after the selection are in Table.4.7. Major source of contamination is again  $e\nu WZ$  channel that has doubled starting cross section due to charge conjugate channel. In part of the sample with  $Z \rightarrow b\bar{b}$  separation is good. For the rest is slowly deteriorating when going to sub channels

Table 4.7: Selection result for  $\nu\bar{\nu}W^+W^-$ . Numbers are expected signal and background for luminosity of  $1ab^{-1}$

Channel	Number of events
$e^+e^- \rightarrow \nu_e\bar{\nu}_e W^+W^- \rightarrow \nu_e\bar{\nu}_e q\bar{q}q\bar{q}$	9279
$e^+e^- \rightarrow \nu_e\bar{\nu}_e ZZ \rightarrow \nu_e\bar{\nu}_e q\bar{q}q\bar{q}$	332
$e^+e^- \rightarrow \nu_e WZ \rightarrow \nu_e q\bar{q}q$	2878
$e^+e^- \rightarrow e^+e^- ZZ \rightarrow e^+e^- q\bar{q}q\bar{q}$	0
$e^+e^- \rightarrow e^+e^- W^+W^- \rightarrow e^+e^- q\bar{q}q\bar{q}$	0
$e^+e^- \rightarrow t\bar{t} \rightarrow X$	8
$e^+e^- \rightarrow W^+W^- \rightarrow q\bar{q}q\bar{q}$	1262
$e^+e^- \rightarrow ZZ \rightarrow q\bar{q}q\bar{q}$	29
$e^+e^- \rightarrow e\nu W \rightarrow e\nu q\bar{q}$	1374
$e^+e^- \rightarrow e^+e^- Z \rightarrow e^+e^- q\bar{q}$	0
$e^+e^- \rightarrow q\bar{q} \rightarrow X$	180

with heavier quark combination.

One can be surprised about the number of event accepted from single W production but you should not forget that only far off shell part of that process was generated anyhow and that this channel has total cross section orders of magnitude higher then the signal. The same situation is with WW process where from millions of events half permille still looks like signal. Since contamination over the final states rises to heavy quark combination emission of high energy neutrinos is probably responsible for the effect. All the remaining contribution are probably negligible. Again with tighter cuts it is possible to get better signal to background ratio but fit was telling us that it is more important to keep significant part of the signal then to have more pure sample.

$$e^+e^- \rightarrow e\nu WZ$$

All the parameters used in the selection are the same as for  $e^-e^-$  reaction with minor changes. Cut on the transverse momentum was adjusted to  $Pt > 25GeV$ . Difference in the tagging of the final state lepton is that here we cannot ask for the exact charge so electrons and positrons are treated equivalently. Difference is also that the final state of the form  $e\nu W^\pm b\bar{b}$  can be reached from the  $t\bar{t}$  state but as one can see in the Table.4.8 no significant contribution is observed.

$$e^+e^- \rightarrow \nu\bar{\nu}ZZ$$

Preselection in this channel contains only final state lepton suppression. Energy threshold for cone method is raised to 20GeV. For the pairing Gaussian condition is used with width of 3.6GeV. Remaining cuts on the kinematic variables are  $M_{miss} > 220GeV$ ,  $E_{tr} > 175GeV$ ,  $200 < E_{miss} < 750GeV$ ,  $\cos\theta_{miss} < 0.999$ . and thrust value of the event should be less than 0.91. Final mass cuts are  $85 < M_Z < 100GeV$ ,  $171 < M_{Z1} + M_{Z2}$ . After event selection estimated number of events is presented in Table.4.9.

As expected major backgrounds are  $\nu\nu WW$  and  $e\nu WZ$  channels. Separation is hard since mentioned channels have significantly larger cross sections. Effectively only variable that produces separation is the mass. But due to the low starting number of events tighter cut would reduce already low number of events. Several options with likelihood approach for

Table 4.8: Selection result for  $e^\pm\nu W^\mp Z$ . Numbers are expected signal and background for luminosity of  $1ab^{-1}$

Channel	Number of events
$e^+e^- \rightarrow \nu_e\bar{\nu}_e W^+W^- \rightarrow \nu_e\bar{\nu}_e q\bar{q}q\bar{q}$	30
$e^+e^- \rightarrow \nu_e\bar{\nu}_e ZZ \rightarrow \nu_e\bar{\nu}_e q\bar{q}q\bar{q}$	21
$e^+e^- \rightarrow \nu_e WZ \rightarrow \nu_e q\bar{q}q$	15022
$e^+e^- \rightarrow e^+e^- ZZ \rightarrow e^+e^- q\bar{q}q\bar{q}$	14
$e^+e^- \rightarrow e^+e^- W^+W^- \rightarrow e^+e^- q\bar{q}q\bar{q}$	629
$e^+e^- \rightarrow t\bar{t} \rightarrow X$	167
$e^+e^- \rightarrow W^+W^- \rightarrow q\bar{q}q\bar{q}$	440
$e^+e^- \rightarrow ZZ \rightarrow q\bar{q}q\bar{q}$	121
$e^+e^- \rightarrow e\nu W \rightarrow e\nu q\bar{q}$	1253
$e^+e^- \rightarrow e^+e^- Z \rightarrow e^+e^- q\bar{q}$	20
$e^+e^- \rightarrow q\bar{q} \rightarrow X$	85

Table 4.9: Selection result for  $\nu\bar{\nu}ZZ$ . Numbers are expected signal and background for luminosity of  $1ab^{-1}$

Channel	Number of events
$e^+e^- \rightarrow \nu_e\bar{\nu}_e W^+W^- \rightarrow \nu_e\bar{\nu}_e q\bar{q}q\bar{q}$	1505
$e^+e^- \rightarrow \nu_e\bar{\nu}_e ZZ \rightarrow \nu_e\bar{\nu}_e q\bar{q}q\bar{q}$	2485
$e^+e^- \rightarrow \nu_e WZ \rightarrow \nu_e q\bar{q}q$	4301
$e^+e^- \rightarrow e^+e^- ZZ \rightarrow e^+e^- q\bar{q}q\bar{q}$	0
$e^+e^- \rightarrow e^+e^- W^+W^- \rightarrow e^+e^- q\bar{q}q\bar{q}$	319
$e^+e^- \rightarrow t\bar{t} \rightarrow X$	49
$e^+e^- \rightarrow W^+W^- \rightarrow q\bar{q}q\bar{q}$	309
$e^+e^- \rightarrow ZZ \rightarrow q\bar{q}q\bar{q}$	68
$e^+e^- \rightarrow e\nu W \rightarrow e\nu q\bar{q}$	763
$e^+e^- \rightarrow e^+e^- Z \rightarrow e^+e^- q\bar{q}$	0
$e^+e^- \rightarrow q\bar{q} \rightarrow X$	85

separation were tested without significant improvement.

$$e^-e^- \rightarrow e^-e^-ZZ \quad \text{and} \quad e^+e^- \rightarrow e^+e^-ZZ$$

Both channels have one distinct feature in common that is two leptons in the final state. In addition they have smallest cross section of all signal processes. Since it is from the start clear that there will not be decent statistics for the signal event selection was made with different focus. We try to bring all the background to 0 level and see if there any signal event left. It is possible to suppress background fully, but for the  $e^-e^-ZZ$  process we have extracted 28 events from  $8ab^{-1}$ . For  $e^+e^-ZZ$  situation is similar (31 event in  $10ab^{-1}$ ). In addition that signal part of the  $e^+e^-ZZ$  we also have contribution from the triple weak boson production and since one is forced to put Z mass constrain on lepton pair no scattering events were extracted. In order to have any hope of separating this from  $eeWW$  channel b-tagging is must suppression of background required to restrain ourselves to at least  $ZZ \rightarrow xbb$ . Selection for  $e^-e^-$  requires two isolated leptons. Cut for the threshold energy for such consideration is raised to 20GeV. Pairing is one width Gaussian function with  $\sigma = 3.6GeV$ . Missing energy before tagged leptons removal should be  $E_{miss} < 240GeV$ , there should be at least two jets with b-tag. Total mass of the event  $M_{tot} > 200GeV$  and  $\cos\theta_{miss} < 0.996$  were also used. Final mass constraints are  $83 < M_Z < 100GeV$  and  $172 < M_{Z1} + M_{Z2} < 191GeV$ . For  $e^+e^-$  there is additional cut that  $|M_{ee} - M_Z| < 5GeV$ . Thus there are enough events to formally extract the value but one should be cautious with interpretation of the result. What is beyond any doubt that this channel is on the edge of detection.

### 4.3 Quartic couplings extraction

If quartic couplings deviate from the expected SM values we hope to see deviation in some of the distributions that are sensitive to them. Extracting of their values can proceed in at least two ways. One would be to generate another sample of events with  $\vec{\alpha} \neq \vec{\alpha}(SM)$  construct wanted distributions and then extract sensitivity. In case of only one free variable this would be fully acceptable, but we have multi parameter space with variables coming in linear combinations that makes such approach highly tedious. Second possibility is to assign weight to the event depending on the coupling and use re-weighted distributions for the fit. Since Whizard-O'Mega combination support recalculation of the matrix element for already generated events if one of the parameters is changed (in our case anomalous couplings) we will use this approach.

How should the weights look like? For the signal processes we have the part of the matrix element that is not dependent on the quartic couplings, in some sense SM background, and non SM part linear in  $\alpha_i$  in total:

$$M_{total} = M_{SM} + M_{\alpha} \quad (4.11)$$

leading to the quadratic dependence of squared matrix element on  $\alpha_i$ :

$$\begin{aligned} M_{total}M_{total}^* &= (M_{SM} + M_{\alpha})(M_{SM} + M_{\alpha})^* \\ &= M_{SM}M_{SM}^* + M_{SM}M_{\alpha}^* + M_{SM}^*M_{\alpha} + M_{\alpha}M_{\alpha}^* \\ &= 1 + \mathcal{O}(\alpha) + \mathcal{O}(\alpha^2) \end{aligned} \quad (4.12)$$

Taking this into account weight for the events were chosen to have following, quadratic, form:

$$R(\alpha_i, \alpha_j) = 1 + A\alpha_i + B\alpha_i^2 + C\alpha_j + D\alpha_j^2 + E\alpha_i\alpha_j \quad (4.13)$$

Table 4.10: Evaluation shema for extraction of weight coefficients.

<b>N</b>	$\alpha_i$	$\alpha_j$
$R_1$	$+a$	$0$
$R_2$	$-a$	$0$
$R_3$	$0$	$+a$
$R_4$	$0$	$-a$
$R_5$	$+a$	$+a$

where coefficients A to E should be determined on event by event basis and  $\alpha_i, \alpha_j$  stands for quartic couplings or their linear combinations. We need 5 point with different value for the coupling in order to extract weight coefficients A to E. The points were chosen according to the shema in Table. 4.10, where “a” i particular value of the coupling. Once we have weights  $R_1$  to  $R_5$  solving the system of linear equations gives the coefficients:

$$\begin{aligned}
A &= \frac{R_1 - R_2}{2a} \\
B &= \frac{R_1 + R_2 - 2}{2a^2} \\
C &= \frac{R_3 - R_4}{2a} \\
D &= \frac{R_3 + R_4 - 2}{2a^2} \\
E &= \frac{R_5 - R_1 - R_3 + 1}{a^2}
\end{aligned} \tag{4.14}$$

Choice of “a” is important since it must satisfy some conditions. Re-weighting method is based on the assumption that phase space for the generation of the events has not changed much (there are no peaks just scaling) so that the regeneration of the events is not needed thus large values of the parameter “a” must be avoided since they could correspond to the situation where this assumption is not valid any more. Extremely small values of the parameter “a” should be also avoided for precision raison since matrix element recalculation was limited to a double precision and we have differences of close by numbers in eq.4.14. As an optimal choice value of 1 i.e  $1/16\pi$  was taken for the calculation (increased to 3 for the low sensitivity channel like  $e^\pm\nu W^\mp Z$  to avoid mentioned problems). For all events of the signal processes coefficients were calculated and stored. After selection of the events coefficients for selected events are used in the fit.

Measurement sensitivity was evaluated using binned likelihood minimized using Minuit [64]. Particular care was taken with binning. Formally with increase of the number of bins the precision would rise, but it could lead to the situation when the number of events per bin is such that statistics assumed for construction of the likelihood is not valid any more and to the wrong results. Over binning shows itself in unstable results with respect to the small adjustment of the bin position and in the jumps of the global minima to the isolated local minima far form the SM expectation value. Number of bins was adjusted in such a way to maximize the sensitivity by keeping the constrain of min number of events in bin at the order of 10.

$$L(\alpha_p, \alpha_q) = - \sum_{i,j,k,l} N^{SM}(i, j, k, l) \ln (N^{\alpha_p, \alpha_q}(i, j, k, l)) + \sum_{i,j,k,l} N^{\alpha_p, \alpha_q}(i, j, k, l) \tag{4.15}$$

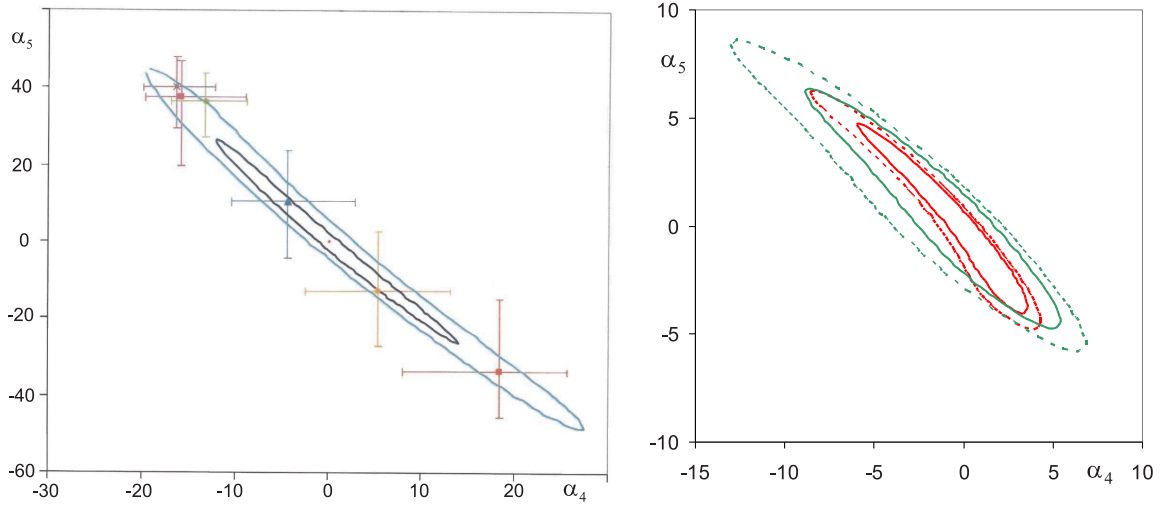


Figure 4.8: Stability of the quartic couplings extraction procedure for  $\nu\nu W^- W^-$  process. In dark blue 50% CL, in light blue 95% CL, six “measurements” with  $1\sigma$  errors on top of it on the left. Consistency of obtained result for  $\nu^+ W^-$  channel at 800 GeV in green, and 1 TeV red, 70% CL in full, 95% CL dotted.

where bins  $(i,j,k,l)$  are over mass of the event, production and two decay angles. Standard model expectation is plain sum of the number of events in the bin  $N^{SM}(i,j,k,l) = \sum R(0,0) = \sum 1$  and the  $N^{\alpha_p, \alpha_q}(i,j,k,l) = \sum R(\alpha_p, \alpha_q)$  is the sum of the re-weighted events in the same bin. Since we are interested in the sensitivity of the measurement and not the outcome for the particular dataset, signal events were generated with significantly larger statistics ( $\sim 10x$ ) than one expected. The likelihood was then appropriately scaled down to the nominal luminosity. Naturally this kind of procedure rises question of the result stability and possible systematic effects introduced by it. This doubt was eliminated by following test in the early stage of analysis. Large signal sample was first passed through the analysis chain and the limit for the couplings were extracted (by scaling down the likelihood to  $1ab^{-1}$ ). The sample was then splitted in subsamples with nominal luminosity  $1ab^{-1}$  in such a way that in the fitting this part of the sample is not participating thus removing the possible bias from usage of the same events. This was done for 6 subsamples. The result is in the Fig.4.8 for the  $e^-e^- \rightarrow \nu\nu W^- W^-$  process. We see that spread of “measurement” points fits well with the extracted confidence level contours and that the procedure is making reliable sensitivity limits prediction. Additional confirmation to the reliability of results is there is no intersection of confidence level contours obtained at different energies demonstrated on  $\nu\nu W^+ W^-$  process on the same figure. Never the less thing to remember is that procedure is not giving the result of a particular measurement but sensitivity limits for large number of such measurements!

Here we should also say few words about the structure of the solution i.e. shape of the confidence level contour. As for one event same behavior is for the total cross section. From eq.4.13 putting left side to one and taking some averaged coefficients A-E that are corresponding to the whole data set we have the condition for the cross section equal to the SM value

$$A\alpha_i + B\alpha_i^2 + C\alpha_j + D\alpha_j^2 + E\alpha_i\alpha_j \equiv 0 \quad (4.16)$$

that represents general form of second order curve in the plain i.e. ellipse. Due to the finite

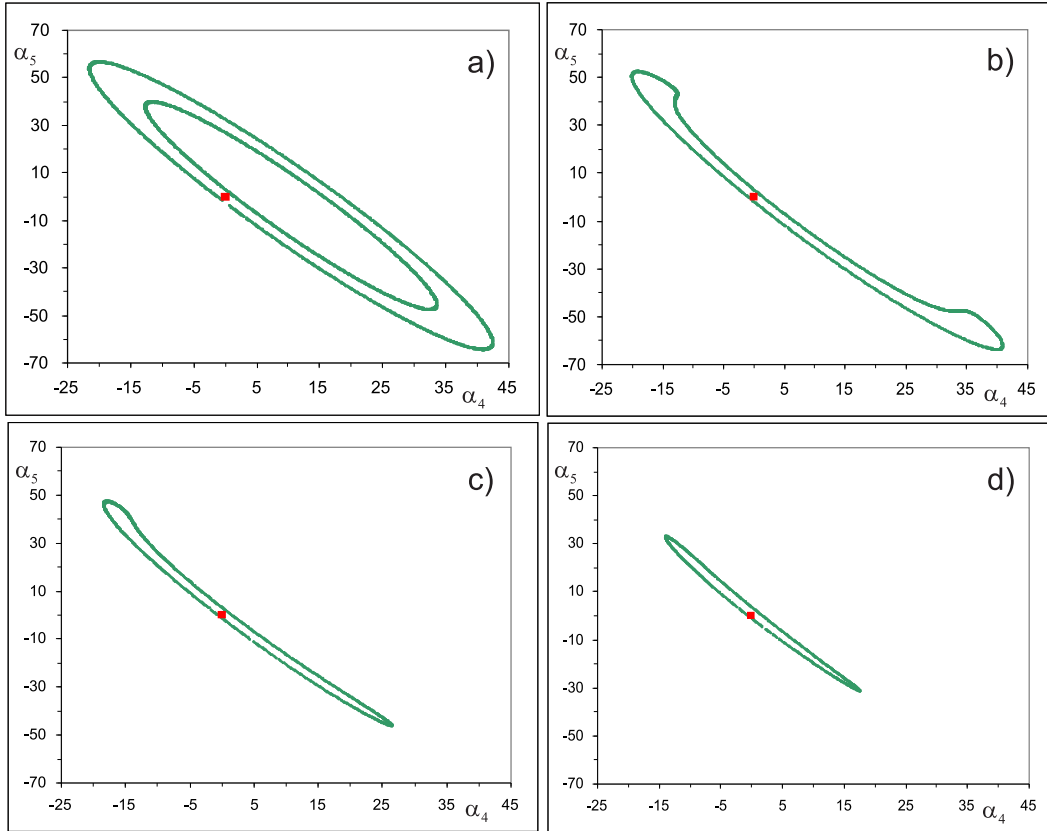


Figure 4.9: Impact of introduction of sensitive variables in the fit. a) only normalization, b) production angle added, c) decay angle added, d) all 4 variables.

precision to which cross section is measured instead of line we will get the band in around this curve with width defined with sensitivity of the process ( how steeply cross section changes with  $\alpha$ 's ) and statistical error of the cross section. The solution is thus symmetrical around the minimum of the cross section and passing through the SM point as on Fig.4.9a). With additional variables we are breaking the symmetry of the soliton and constraining the region of acceptable  $\alpha$ 's as on the Fig.4.9 b),c),d). Naturally question rises: Why only 4 “sensitive” variables lets introduce another and increase sensitivity even further? This naive idea is too good to be true. We have already exploited most sensitive variables thus introduction of lower sensitivity will increase correlations between the variables and problems with the stability of the fit. And in order to preserve bin statistic we cannot make significant increase in number of bins to exploit new variable fully. Just for fun additional fit distributions were introduced like .

#### 4.4 Quartic coupling limits

Limits obtained from the fit will be expressed in two ways, with  $1\sigma$  errors (due to the non parabolic nature of solution around minimum asymmetric errors are quoted) in the tables and

Table 4.11: Results for all scattering processes in  $e^+e^-$  collisions, assuming isospin conservation.

process	$\alpha_4$		$\alpha_5$	
	$\sigma_-$	$\sigma_+$	$\sigma_-$	$\sigma_+$
$\nu\nu W^+W^-$	-3.97	2.88	-3.11	3.33
$\nu\nu ZZ$	-3.76	3.50	-1.72	1.62
$e^\pm\nu W^\mp Z$	-3.01	4.31	-3.62	4.57
$e^+e^- ZZ$	-3.63	3.59	-	-

Table 4.12: Results for all weak boson scattering processes in  $e^-e^-$  collisions, assuming isospin conservation.

process	$\alpha_4$		$\alpha_5$	
	$\sigma_-$	$\sigma_+$	$\sigma_-$	$\sigma_+$
$\nu\nu W^+W^-$	-8.95	12.44	-22.63	19.23
$e^-\nu W^-Z$	-6.39	7.66	-6.17	9.93

with the 70% and 95% confidence level contours on the plots, when applicable. Error matrices and correlation coefficients are in appendix.

### Electron positron channels

For  $e^+e^-$  channel as already stated we assumed luminosity of  $1ab^{-1}$  at center of mass energy of 1TeV. Results are summarized in Table.4.11 and in Fig.4.10, for isospin conserving case. In  $\nu\nu W^+W^-$  channel there is only dependence to  $\alpha_4$  and  $\alpha_5$  so this is only possible solution. In case of  $\nu\nu ZZ$  and  $e^\pm\nu W^\mp Z$  processes dependence is on linear combinations ( $\alpha_4 + \alpha_6$ ) and ( $\alpha_5 + \alpha_7$ ) and solution is extracted by setting  $\alpha_6 = \alpha_7 = 0$ . For  $e^+e^- ZZ$  channel we have dependence on all couplings in the form ( $\alpha_4 + \alpha_5 + \frac{1}{2}(\alpha_6 + \alpha_7 + \alpha_{10})$ ) due to the low number of selected events no simultaneous extraction of  $\alpha_4$  and  $\alpha_5$  is possible thus results are extracted fro normalization only in form of  $\alpha_4$  setting other couplings to 0.

### Electron electron channels

Due to the anti pinch effects luminosity in  $e^-e^-$  collisions is significantly lower ( $\sim 1/3$  of  $e^+e^-$ ). Due to this facts we have taken luminosity that is equivalent to the same running time as in  $e^+e^-$  option for the reference one ( $3050fb^{-1}$ ). Result are summarized in Table.4.12 and Fig.4.11. Results for both stated channels are obtained under same conditions as in  $e^+e^-$ . Result for the  $e^-e^- ZZ$  channel is missing since ewen with significant effort significant separation of the signal was possible.

General conclusion that holds for all considered processes is that form single channel desired level of precision ( $\mathcal{O}(1)$ ) cannot be acheaved (with realistic luminosity) even with additional assumptions like isospin conservation. Thus we need combination of measurements to enhance overall knowledge about quartic couplings and underlying physics.

#### 4.4.1 Combined results

Since we have used likelihood for extraction of sensitivity technically obtaining combined result for several processes is technically straight forward. First of all on can consider combination

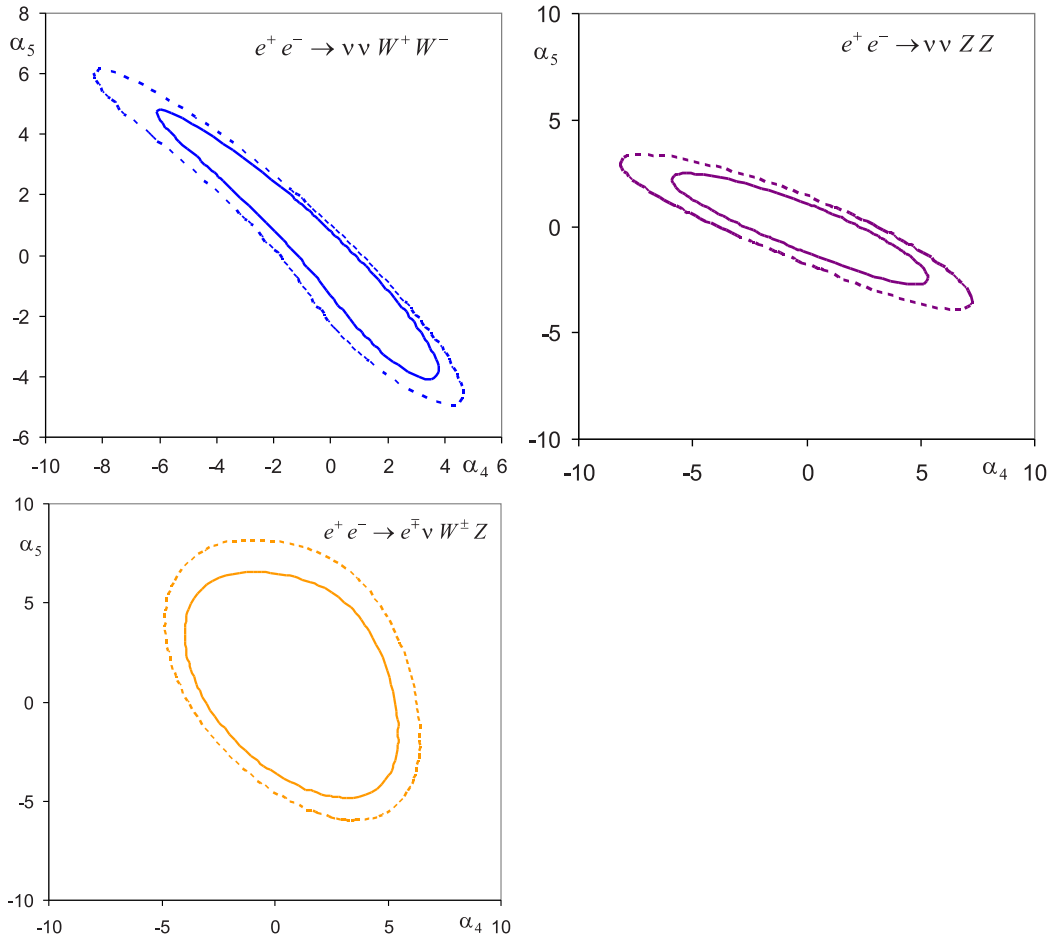


Figure 4.10: Sensitivity limits for weak boson scattering processes at 1TeV. Luminosity of  $1ab^{-1}$  is assumed. 70%CL in full line, 95%CL in dotted.

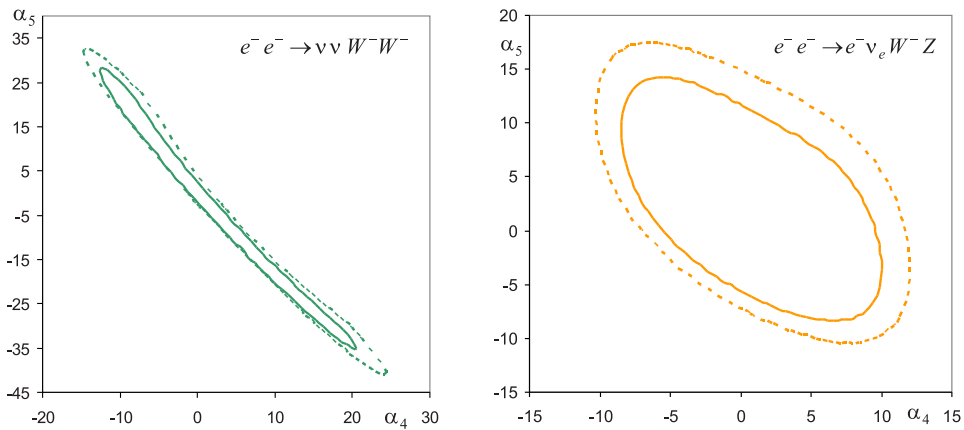


Figure 4.11: Sensitivity limits for  $\nu \nu W^- W^-$  channel and  $e^- e^- \rightarrow e^- \nu_e W^- Z$  on the right. Luminosity of  $350fb^{-1}$  is assumed. 70%CL in full line, 95%CL in dotted

Table 4.13: Combined limits in isospin conserving case for all  $e^+e^-$  sensitive processes and luminosity of  $1ab^{-1}$ .

coupling	$\sigma^-$	$\sigma^+$
$\alpha_4$	-1.41	1.38
$\alpha_5$	-1.16	1.09

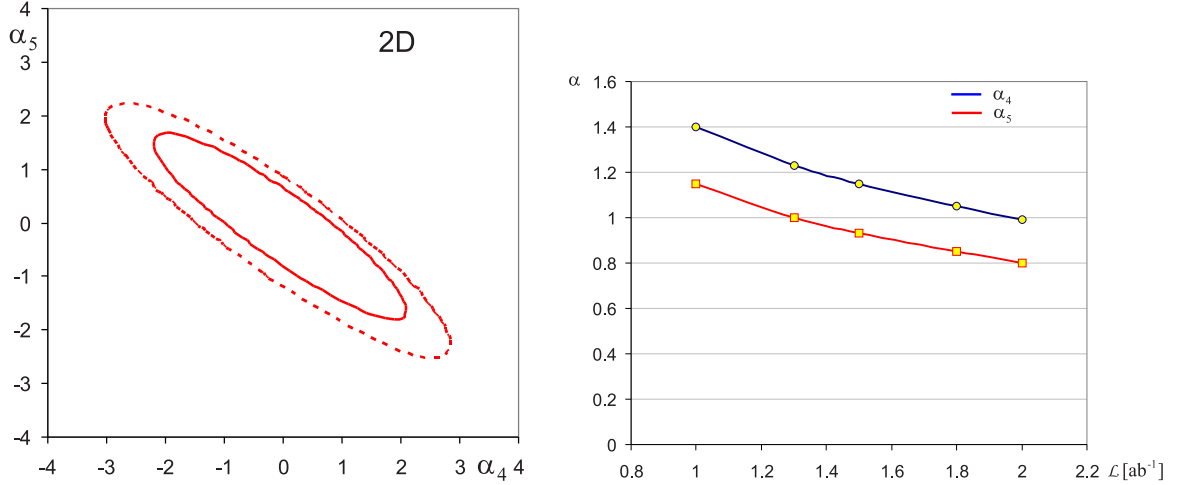


Figure 4.12: Combined limits for all  $e^+e^-$  in isospin conserving case on the left (Full line 70%CL , dotted 95%CL). Needed luminosity to reach  $\mathcal{O}(1)$  precision on the right.

of all measurements from  $e^+e^-$  collisions. Since there is no overwhelming amount of facts (except  $\rho \approx 1$ ) for the isospin conserving interaction we will consider both possibilities. For the isospin conserving case limits are in Table.4.13 and Fig.4.12. In isospin conserving case we are now much closer to the desired precision but still above. Naturally question rises: “What is needed luminosity to reach  $\mathcal{O}(1)$  precision. Scaling the likelihood to higher luminosity allows us to answer this question as shown in Fig.4.12, concluding that needed luminosity in this case is around  $2ab^{-1}$ .

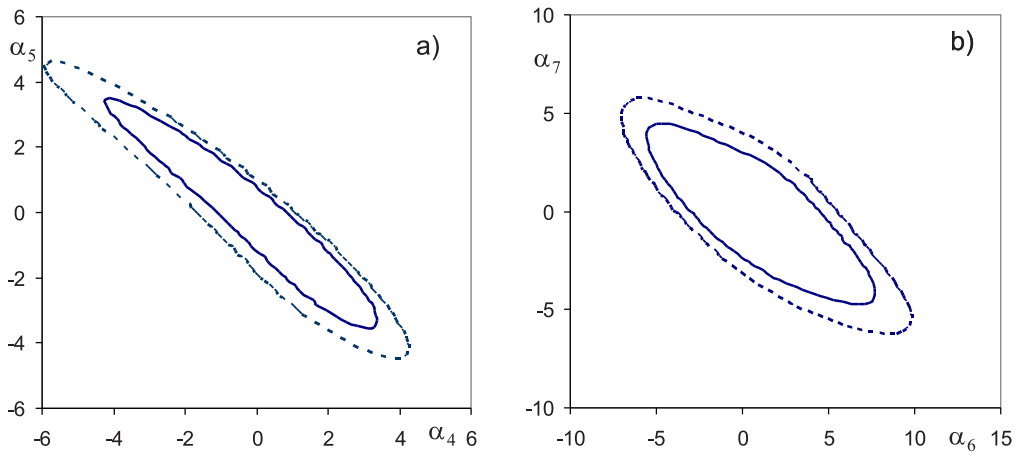
If we do not require isospin conservation we need the solution to five dimensional fit with, due to the linear combinations of couplings, rather high correlations between variables. This is not wanted but unavoidable. With significant care fit gives stable result. Limits are shown in Table4.14 and with two contours on the Fig.4.13 that represent projection of the solution hypersurface at given CL level to the plane in question ( $\alpha_4 - \alpha_5$  or  $\alpha_6 - \alpha_7$ ).

#### 4.4.2 Running options

Since  $e^-e^-$  is, surprisingly, still a possible option for the ILC we can check for some reason time for collecting luminosity is shared by two options how it could affect or conclusion about obtainable limits. Here we assume that luminosity for  $e^-e^-$  is 1/3 of that for  $e^+e^-$  in the same running time. Combined result for luminosity of  $2ab^{-1}$  is compared with combination of results from  $1ab^{-1}$  in  $e^+e^-$  and  $350fb^{-1}$  in  $e^-e^-$  mode. As one can see from Fig.4.14 and Table.4.15 two results are almost identical. From that we conclude that measurement

Table 4.14: Combined limits for all  $e^+e^-$  sensitive processes and luminosity of  $1ab^{-1}$ .

coupling	$\sigma^-$	$\sigma^+$
$\alpha_4$	-2.70	2.88
$\alpha_5$	-2.48	2.34
$\alpha_6$	-3.92	5.54
$\alpha_7$	-3.20	3.04
$\alpha_{10}$	-5.18	4.53

Figure 4.13: Combine limits for all  $e^+e^-$  processes. Confidence level contour in  $\alpha_4 - \alpha_5$  plain (a), and in  $\alpha_6 - \alpha_7$  plain (b). Full line 70%CL, dotted 95%CL.

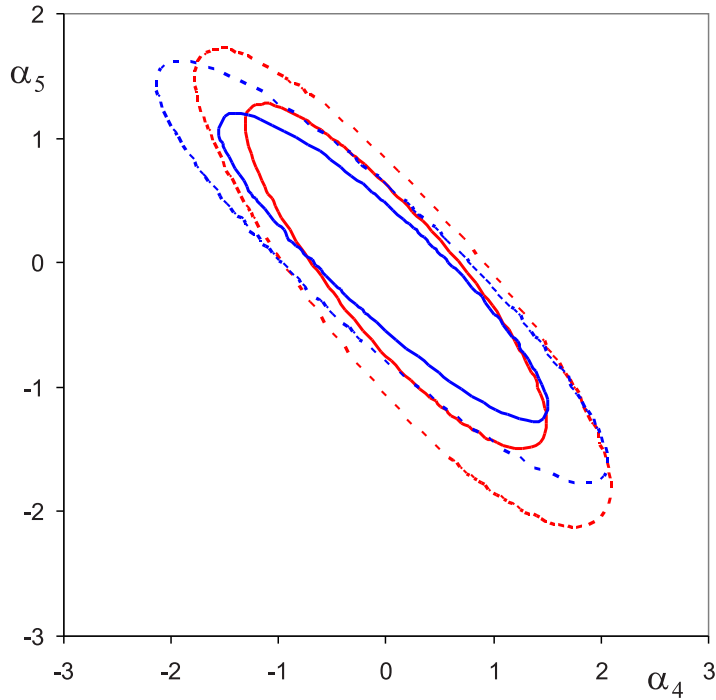


Figure 4.14: Limits in combination of collider running options. In blue only  $e^+e^-$  mode in red combination of  $e^+e^-$  and  $e^-e^-$  measurements. Full line 70%CL limit , dotted 95%CL.

Table 4.15: Comparison of running modes. for  $2ab^{-1}$  in  $e^+e^-$  collisions and combination of  $1ab^{-1}$  for  $e^+e^-$  channels with  $350fb^{-1}$  in  $e^-e^-$  under assumption of isospin conservation.

coupling	$e^+e^-$		$e^+e^-$ and $e^-e^-$	
	$\sigma-$	$\sigma+$	$\sigma-$	$\sigma+$
$\alpha_4$	-0.99	0.98	-0.87	0.94
$\alpha_5$	-0.82	0.78	-0.99	0.84

of quartic couplings does not restrict flexibility of physics program is case of the unexpected. There is a restriction to this flexibility. Part of the running time in the  $e^+e^-$  mode is must since only  $\nu$  that is to say  $WW \rightarrow ZZ$  channel possesses high enough sensitivity to restrict  $\alpha_5$  thus running only in  $e^-e^-$  is not desired by this measurement.

## 4.5 Model dependent limits on new physics

In any measurement the goal is not just to obtain the number but to understand what it means. Latest at this step there is a need to drop so far pursued goal of model independence and to interpret the results in particular scenario of new physics.

### 4.5.1 Combination of measurements

Any new physics scenario will not manifest itself in one and only one physics measurement. In order to describe the new phenomena usually several measurements are needed, on the other hand analysis results often neglect this natural synergy. But physics analysis are often done in such way that it is very difficult to combine their results in natural way either due to the way results are presented or due to the incompatibility of assumptions and(or) approximation that were made. As already explained measurement of the quartic couplings comes in later stage of the ILC operation not only due to the luminosity and center of mass energy needed but also due to requirements that other chiral couplings of lower order are measured with high precision. Final word on measurement prospects can be sad after covering all measurement that are prerequisite to ours, covering the all decay channels of the weak bosons (not only hadronic ones as in our case) and all sources of information (analysis based on rescattering to yet done), nevertheless an attempt to demonstrate this approach was made by combining analysis results of triple weak boson production (although with different positron polarization assumption) and weak boson scattering processes together with additional information from TGC measurement (center of mass energy 800GeV assumed). It is hard to estimate how total luminosity considered in mentioned analysis corresponds to the one finally available for the physics program at given energies, thus more precise estimate of available information for the evaluation of physics reach of such measurement can be sad only once such information exists. Possible impact of the inclusion of rescattering effects in the W pair production used for TGC measurement is also not considered. Even with these known uncertainties we will proceed in interpretation of the results keeping in mind that more consistent set of inputs is needed.

### 4.5.2 Mass limit extraction

We will interpret our results in terms of masses of would be resonances with given quantum numbers as already introduced in chapter 3. Each would be resonance on the bases of their Lagrangian establishes system of equations:

$$\alpha_i = f_i(k_1, \dots, k_j, M) \quad i \in \{4, 5, 6, 7, 10\} \quad (4.17)$$

where  $k_j$  are internal couplings in the resonance Lagrangian, and M is resonant mass. Since both  $k$ 's and M are unknown system cannot be solved. Additionally to this there is a relation of the resonance width to its mass and couplings:

$$\Gamma = F(k_1, \dots, k_j, M) \quad (4.18)$$

Addition of this equation does not change the nature of the system we still have more unknowns than the equations. At this step we need to make an assumption. Weakest one and most straight forward is to declare width as "known" parameterizing as a fraction of the mass:

$$\Gamma = f_w M \quad (4.19)$$

where  $f_w$  is coefficient set by hand. With this we have reduced number of unknowns by one making it possible to solve, getting :

$$M = G(f_w, \alpha_i) \quad (4.20)$$

mass as a function of alphas, and fraction  $f_w$ . Since  $f_w$  is postulated we will express results for different values of  $f_w$  considering broader and narrower resonances. Limits obtained in previous chapter for quartic couplings cannot be used directly in this procedure since alphas

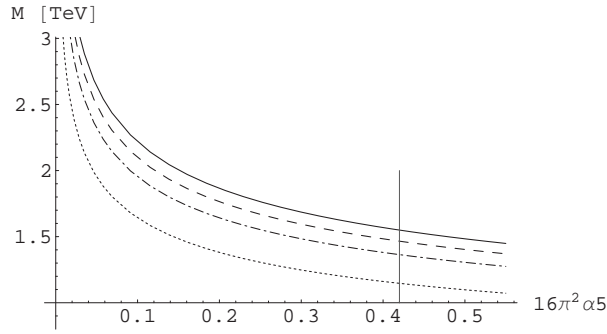


Figure 4.15: Mass of the scalar resonance as a function of  $\alpha_5$  in scalar singlet model, with the resonance width to mass ratio  $f_\sigma$  equal to 1.0 in full line, 0.8 dashed, 0.6 dot-dashed, 0.3 dotted line. One sigma limit on the  $\alpha_5$  as vertical line on the plot.

should satisfy set of equations 4.17. In general there are two possibilities  $j < i$  over constrained system (adding at least one relation of the type  $\alpha_i = g_i(\vec{\alpha})$ ) or  $j = i$  normal situation, together with possibility  $f_i \equiv 0$ . In order to extract quartic coupling limits in particular model alphas were set to zero when applicable and additional relations were exploited when they exist to reduce the number of free alphas to the minimal value. Fitting is then redone and values of the couplings used in eq.4.20 were obtained. Fit is done with Minuit as usual but in some cases where we have additional coupling relations already highly correlated system was too much even for the most stable minimum search methods. In those cases brute force minimum search was performed on the grid in parameter space. All the algebraic computations (leading to the solution 4.20) were done with Mathematica [60] to prevent human made contributions to the new physics.

## 4.6 Mass limit results

### 4.6.1 Scalar singlet

#### Isospin conservation

Lets start from the system of equations 3.82 and 3.83. First we will consider isospin conserving case,  $h_\sigma = 0$ , which leads to  $\alpha_7 = \alpha_{10} = 0$ . Since  $\alpha_4 = \alpha_6 = 0$ , there is only a dependence on  $\alpha_5$  as a free parameter. After the fit, we get  $\sigma_{\alpha_5} = 0.42$  for the symmetric error or  $-0.452 < \alpha_5 < 0.397$  for the asymmetric ones at  $1\sigma$  level. Expressing the width of the resonance as a fraction of its width,  $\Gamma_\sigma = f_\sigma M_\sigma$ , it is possible to solve eq. (3.83) and  $\alpha_5 = g_\sigma^2 \frac{v^2}{8M_\sigma^2}$  to obtain the resonance mass as a function of the quartic coupling and this fraction:

$$M_\sigma = v \left( \frac{4\pi f_\sigma}{3\alpha_5} \right)^{\frac{1}{4}} \quad (4.21)$$

In Fig. 4.15, we plot the mass of a scalar singlet resonance as a function of the coupling for a given width. The vertical line in the plot is the  $1\sigma$  sensitivity limit. Results are summarized in the Table.4.6.1

$f_\sigma = \frac{\Gamma_\sigma}{M_\sigma}$	1.0	0.8	0.6	0.3
$M_\sigma$ [TeV]	1.55	1.46	1.36	1.15

Table 4.16: Mass reach for the scalar resonance in the  $SU(2)_c$  conserving case depending on different resonance widths.

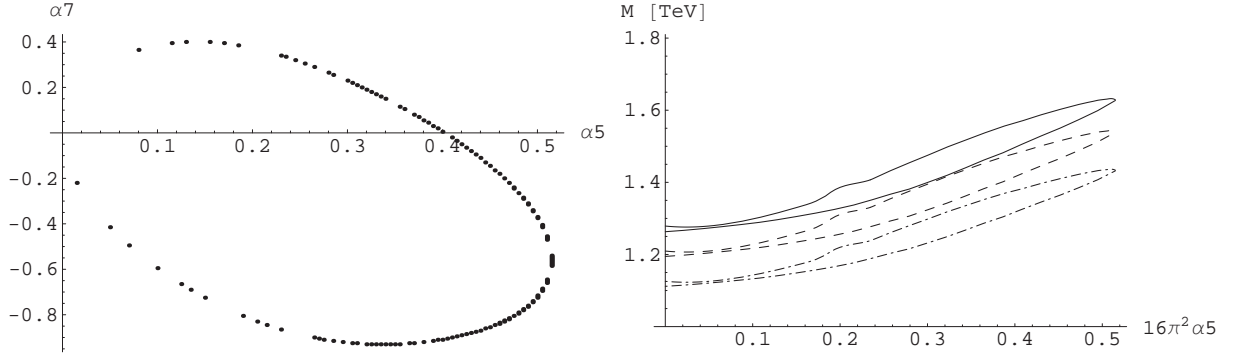


Figure 4.16: On the left,  $1\sigma$  contour in the  $\alpha_5 - \alpha_7$  plane. On the right, the dependence of the resonance mass on  $\alpha_5$  along the contour for  $f_\sigma = 1$  (width equal to the mass) in full, and  $f_\sigma = 0.8$  in dashed and  $f_\sigma = 0.6$  in dot-dashed. Upper and lower lines correspond to the different branches of the solution of  $\alpha_7 = \mathcal{F}[\alpha_5]$ , respectively.

### Isospin violation

If we allow for isospin violation,  $\alpha_4$  and  $\alpha_6$  are still zero, leaving the three free parameters  $\alpha_5$ ,  $\alpha_7$  and  $\alpha_{10}$  for the fit. With only two independent variables, the system of equations (3.82) is over constrained with the additional relation:

$$\alpha_7^2 = 2\alpha_5\alpha_{10} \quad (4.22)$$

that should hold exactly.

Using this equation it is possible to eliminate one of the couplings from further consideration. We will choose to eliminate  $\alpha_{10}$ . Solving the system of equations, it is now possible to express the mass as a function of the width,  $\alpha_5$  and  $\alpha_7$ :

$$M_\sigma = v \left( \frac{4\pi\alpha_5 f_\sigma}{2\alpha_5^2 + (\alpha_5 + 2\alpha_7)^2} \right)^{\frac{1}{4}}. \quad (4.23)$$

If we limit ourselves to the case that we vary the couplings only along the  $1\sigma$  contour in the  $\alpha_5, \alpha_7$  plane, we end up with the result shown in Fig. 4.16. The lower of the two curves (dashed one) gives a lower boundary to the allowed region for the scalar singlet case. Upper boundary you can extract from the maximum of the mass formulae. This gives  $\alpha_7 = -\alpha_5$  and leads to functional dependence of upper boundary as:

$$M_\sigma = v \left( \frac{2\pi f_\sigma}{\alpha_5} \right)^{\frac{1}{4}}. \quad (4.24)$$

Now it is possible to fully constrain the region in  $\alpha_5$  and  $M$  parameter plain. Result is shown in Fig.4.17

$f_\sigma = \frac{\Gamma_\sigma}{M_\sigma}$	1.0	0.8	0.6
$M_\sigma$ [TeV]	1.39	1.32	1.23

Table 4.17: Average mass along the contour for the scalar resonance in the isospin breaking case depending on different resonance widths. Numbers in the table are averaged values along the lower limit.

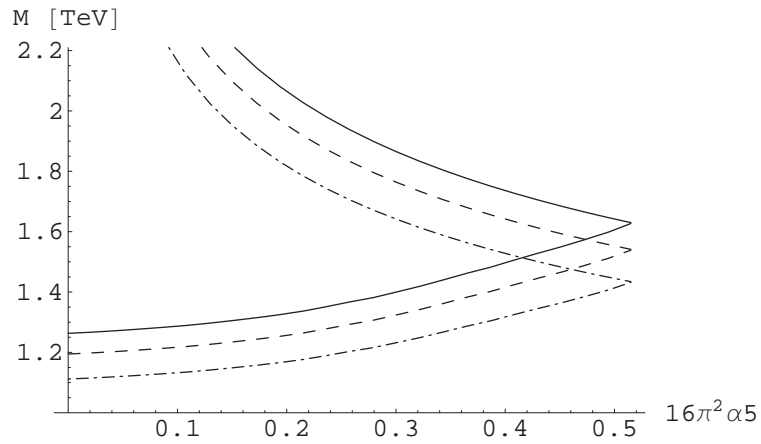


Figure 4.17: Allowed region for scalar singlet resonance with isospin breaking in dependence on  $\alpha_5$  between upper and lower boundary. Ratio of width to mass equal to 1.0 in full, 0.8 dashed, 0.6 dot-dashed.

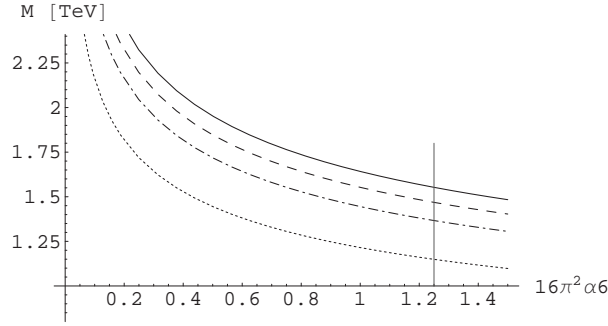


Figure 4.18: Dependence of the resonance mass for the charged component on  $\alpha_6$  for different assumed widths (in  $f_\pi = \Gamma_\pi/M_\pi = 1.0$  in red, 0.8 in green, 0.6 in blue, 0.3 in brown, respectively). The red vertical line represents the maximal value of  $\alpha_6$  along the  $1\sigma$  surface.

$f_\pi = \frac{\Gamma_\pi}{M_\pi}$	1.0	0.8	0.6	0.3
$M_{\pi^0}$ [TeV]	1.49	1.41	1.31	—
$M_{\pi^\pm}$ [TeV]	1.55	1.47	1.37	1.15

Table 4.18: Dependence of the mass reach for scalar triplet resonances on different resonance widths. For neutral component numbers in the table are average values along the lower limit.

#### 4.6.2 Scalar triplet

Considering system of equations 3.86 and 3.87 we can distinguish two solution branches. (a) In the case of  $\alpha_6 = \alpha_7 = \alpha_{10} = 0$  with apparent isospin conservation the solution for Mass dependence on couplings reduces to the isospin conserving case for scalar singlet. With no contribution to the width of charged component.

$$M_{\pi^0} = v \left( \frac{4\pi f_{\pi^0}}{3\alpha_5} \right)^{\frac{1}{4}} \quad (4.25)$$

(b) If we allow for isospin breaking, only  $\alpha_4$  remains zero and we get the constrain:

$$\alpha_7^2 = 2\alpha_5(\alpha_6 + \alpha_{10}), \quad (4.26)$$

which is the generalization of the singlet case. Again we use over constraining to eliminate  $\alpha_{10}$ . Solving the remaining system we get:

$$M_{\pi^\pm} = v \left( \frac{4\pi f_{\pi^\pm}}{\alpha_6} \right)^{\frac{1}{4}} \quad (4.27a)$$

$$M_{\pi^0} = v \left( \frac{2\pi\alpha_5 f_{\pi^0}}{\alpha_5^2 + (\alpha_5 + \alpha_7)^2} \right)^{\frac{1}{4}} \quad (4.27b)$$

with additional condition that  $\alpha_5$  and  $\alpha_6$  must be positive in order to get real solutions for the mass.

Results are shown in Table.4.6.2.

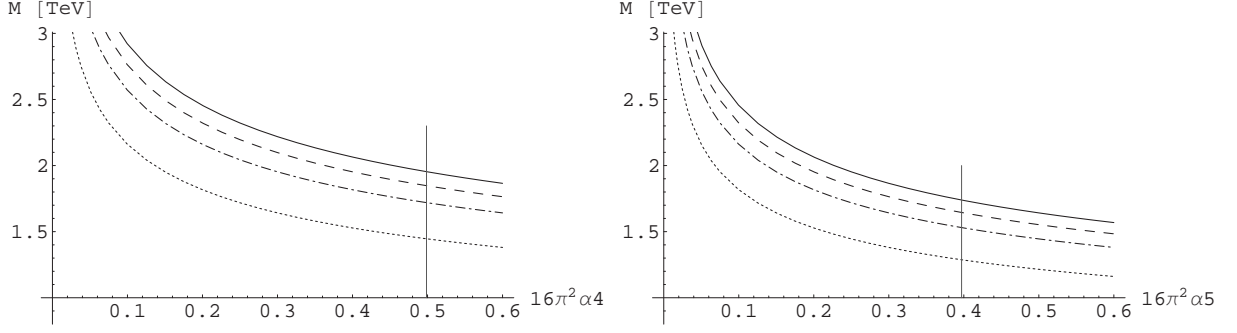


Figure 4.19: Dependence of the resonance mass for the all components on  $\alpha_4$  for different assumed widths (in red  $f_\phi = \Gamma_\phi/M_\sigma = 1.0$ , green 0.8, blue 0.6, brown 0.3). The red vertical line represents the maximal value of  $\alpha_4$ . On the right, the special case when  $\alpha_5 \neq 0$ , red line represents  $\alpha_5$  at  $1\sigma$

$f_\phi = \frac{\Gamma_\phi}{M_\phi}$	1.0	0.8	0.6	0.3
$M_\phi$ [TeV]	1.95	1.85	1.72	1.45
$M_{\phi 0}$ [TeV]	2.06	1.96	1.82	1.53

Table 4.19: Mass reach for the scalar quintet in the  $SU(2)_c$  conserving case depending on different resonance widths.  $M_\phi$  corresponds to the equation 4.28 and  $M_{\phi 0}$  for 4.29

### 4.6.3 Scalar quintet

Considering solutions of the equations 3.90 and 3.91 we can split the result in several classes: (a) For isospin conservation only  $\alpha_4$  is non-vanishing. Leading to the unique solution

$$M_\phi = M_{\phi 0} = M_{\phi +} = M_{\phi ++} = v \left( \frac{4\pi f_\phi}{\alpha_4} \right)^{\frac{1}{4}} \quad (4.28)$$

(b) In case of broken isospin symmetry there are several possible solution i.e. physics scenarios. In case that only  $h'_\phi = 0$  i.e. only  $\alpha_5$  is non-vanishing. Charged and doubly charged resonances do not get contribution to the width at leading order. And the solution for neutral state is:

$$M_{\phi 0} = v \left( \frac{2\pi f_\phi}{\alpha_5} \right)^{\frac{1}{4}} \quad (4.29)$$

For the case of isospin breaking,

$$\alpha_7^2 = 2\alpha_5 \left( \frac{1}{2}\alpha_4 + \alpha_6 + \alpha_{10} \right), \quad (4.30)$$

that is used to eliminate  $\alpha_{10}$  but this time with two branches for solution. We obtain the solution for masses

$$M_{\phi \pm\pm} = v \left( \frac{4\pi f_{\phi \pm\pm}}{\alpha_4} \right)^{\frac{1}{4}} \quad (4.31)$$

$$M_{\phi \pm} = v \left( \frac{4\pi f_{\phi \pm}}{\alpha_4} \right)^{\frac{1}{4}} \quad (4.32)$$

$$M_{\phi^0} = v \left( \frac{12\pi\alpha_5 f_{\phi^0}}{(\sqrt{\alpha_4\alpha_5} - 2\alpha_5)^2 + 2(\alpha_5 + \alpha_7)} \right)^{\frac{1}{4}} \quad (4.33)$$

For the doubly charged component situation is clear if  $g_\phi$  is not zero there is a contribution to it, and we can extract the mass limit in the usual way.

For single charged component there is a special situation when  $\alpha_4 = -\alpha_6$  when we have no contribution to the width of this component but still contributions to the width of neutral and doubly charged ones. Relation between couplings reduces to

$$\alpha_7^2 = 2\alpha_5 \left( -\frac{1}{2}\alpha_4 + \alpha_{10} \right) \ \& \ \alpha_6 = -\alpha_4 \quad (4.34)$$

And we have expressions for the mass

$$M_{\phi^{++}} = v \left( \frac{4\pi f_{\phi^{++}}}{\alpha_4} \right)^{\frac{1}{4}} \quad (4.35)$$

$$M_{\phi^0} = v \left( \frac{12\pi\alpha_5 f_{\phi^0}}{2(\alpha_5 + \alpha_7)^2 + \alpha_5(\sqrt{\alpha_4} - 2\sqrt{\alpha_5})^2} \right)^{\frac{1}{4}} \quad (4.36)$$

For special case a) lower limits are the same only difference is that there is no upper limit for neutral case since there is a singular direction of mass equation when denominator is zero but  $\alpha_5$  is still nonzero. this can be seen on the plot ( maybe to drop this plot at all I'll redo it in nicer way anyhow)

special case b) ..  $h_\phi = k_\phi = 0$  leads to  $\alpha_6 = \alpha_{10} = 0$  contributions to the charged components are the same.

$$M_{\phi^{++}} = M_{\phi^+} = v \left( \frac{4\pi f_{\phi^{++}}}{\alpha_4} \right)^{\frac{1}{4}} \quad (4.37)$$

$$M_{\phi^0} = v \left( \frac{4\pi\alpha_4 f_{\phi^0}}{\alpha_4^2 + 2\alpha_7^2} \right)^{\frac{1}{4}} \quad (4.38)$$

with the relation between couplings reduced to:

$$\alpha_7^2 = \alpha_5\alpha_4 \quad (4.39)$$

c) general case

$f_\phi = \frac{\Gamma_\phi}{M_\phi}$	1.0	0.8	0.6	0.3
$M_\phi$ [TeV]	1.95	1.85	1.72	1.45
$M_{\phi^0}$ [TeV]	1.77	1.67	1.55	1.31

Table 4.20: Mass reach for the scalar quintet special case b) depending on different resonance widths.  $M_\phi$  corresponds to the equation 4.37 and  $M_{\phi^0}$  for 4.38 as an average over lower limit

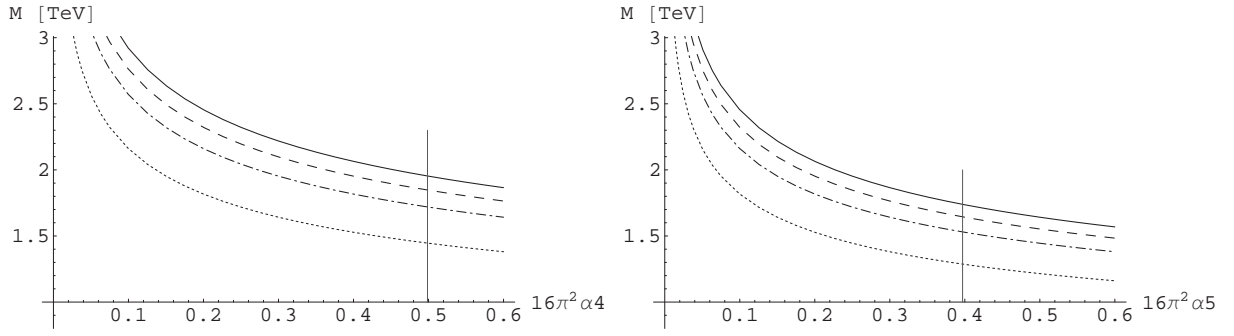


Figure 4.20: Dependence of the resonance mass for special case b) on  $\alpha_4$  for different assumed widths (in red  $f_\phi = \Gamma_\phi/M_\sigma = 1.0$ , green 0.8, blue 0.6, brown 0.3). The red vertical line represents the maximal value of  $\alpha_4$ . On the left dependence for charged members, on the right for neutral

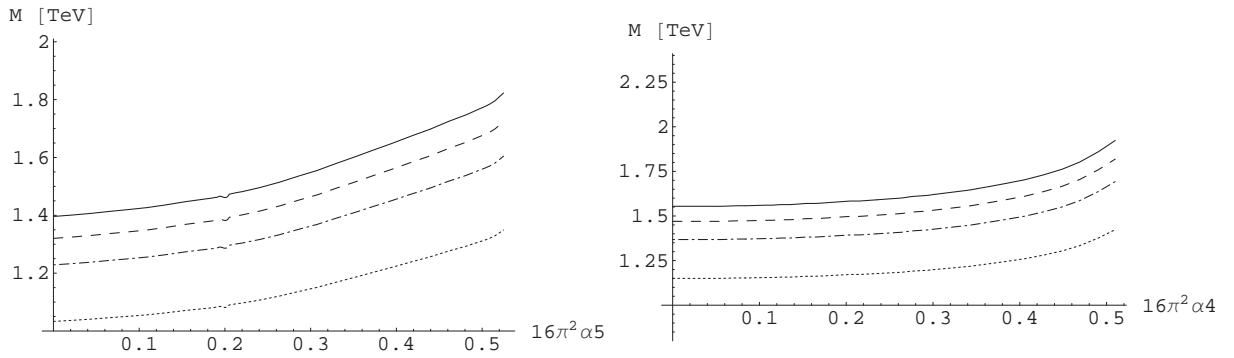


Figure 4.21: from left to right mass dependence in most general case for neutral, charged and doubly charged component of multiplet

$f_\phi = \frac{\Gamma_\phi}{M_\phi}$	1.0	0.8	0.6	0.3
$M_{\phi_{\pm\pm}}$ [TeV]	1.95	1.85	1.72	1.45
$M_{\phi_{\pm}}$ [TeV]	1.64	1.55	1.44	1.21
$M_{\phi_0}$ [TeV]	1.55	1.46	1.35	1.14

Table 4.21: Mass reach for the scalar quintet in most general case.  $M_{\phi_0}$  and  $M_{\phi_{\pm}}$  are averages over lower limit.

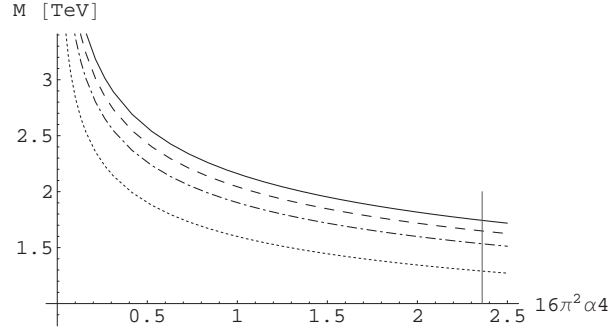


Figure 4.22: Dependence of Mass of vector resonance on  $\alpha_4$  for different assumed widths (in  $f_\pi = \Gamma_\pi/M_\pi = 1.0$  in red, 0.8 in blue, 0.3 in brown, respectively), under condition  $l_\omega = 0$

$f_\omega = \frac{\Gamma_\omega}{M_\omega}$	1.0	0.8	0.6	0.3
$M_\omega$ [TeV]	1.74	1.65	1.53	1.29

Table 4.22: Mass for vector resonance case  $l=0$ , for different assumed widths (in  $f_\pi = \Gamma_\pi/M_\pi = 1.0$  blue 0.8, green 0.6, brown 0.3).

#### 4.6.4 Vector singlet

For vector singlet isospin breaking has to be involved. First we find the solution from the system of equation for quartic couplings and additional  $\lambda$  type couplings contributing to the same order as in (eq.3.92). Ignoring the parameter  $k_\omega$  since it has no physical meaning in terms of the resonance mass and width, at least to the order considered. Relation between the couplings are as:

$$\alpha_1 = \alpha_2 = \alpha_4 = \alpha_7 = -\alpha_5 = -\alpha_6 = -\alpha_8 = -\alpha_9 \quad (4.40)$$

leaving only one free coupling for which we chose  $\alpha_4$ . Solution for the mass then is:

$$M_\omega = v \left( \frac{96\pi f_\omega - l_\omega^2}{8\alpha_4} \right)^{\frac{1}{4}} \quad (4.41)$$

For the limit extraction we use simplifying assumption  $l_\omega = 0$  that reduces solution to:

$$M_\omega = v \left( \frac{12\pi f_\omega}{\alpha_4} \right)^{\frac{1}{4}} \quad (4.42)$$

Now we have two free parameters one can be determined from measurement of quartic couplings  $\alpha_4$  but for the second  $f_\omega$  we need additional measurement. Such measurement is measurement of triple couplings as is [73] or [74]. We use result [73] to construct the  $\chi^2$  for the  $\Delta g_1^Z, \Delta k^Z$  and  $\lambda^Z$  and use consistent set of numbers at  $1\sigma$  level. Results for this case are shown in Fig. 4.22 and table 4.6.4.

Now we introduce triple couplings into the solution, but if we want to be consistent one cannot allow cosines and sines of the mixing angles to go above 1. From this one gets natural upper constrain on the mass. Since only  $l_\omega$  is contributing to the width of resonance it's sufficient to solve  $M$  as a function of  $\lambda_z, \alpha_4, f_\omega$ . In the solution  $\lambda_z$  comes only in squares and it's

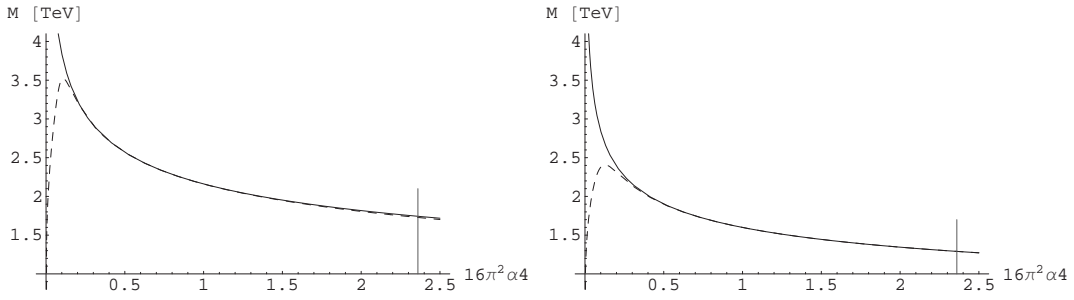


Figure 4.23: Dependence of Mass of vector resonance on  $\alpha_4$  for different assumed width equal to the mass on the left and 0.3 of the mass on the right. Red curve is upper limit. Blue one is for maximal value of  $\lambda_z$  and brown one for  $\lambda_z = 0$  that coincides with discussed case  $l_\omega = 0$

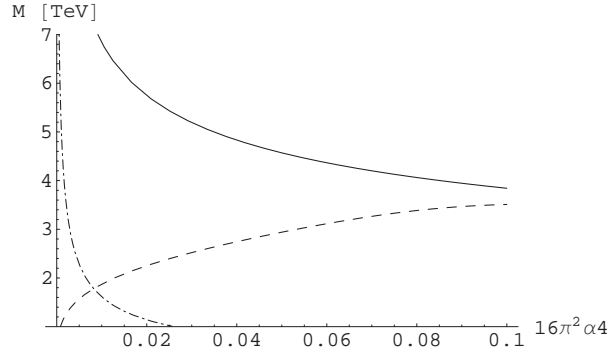


Figure 4.24: Dependence of Mass of vector resonance on  $\alpha_4$  for different assumed width equal to the mass. Red curve represents constrain coming from  $\beta_1$

thus not sensitive to the sign, and using results from [73] we obtain the range  $0 < \lambda_z < 0.00033$ . If we plot now two extreme cases for  $\lambda_z$  we get.

If I do not use the correction to the cw and sw there is no influence on the result since  $\lambda_z$  is so small. The result is same as for  $l=0$ . If we use the limit  $\alpha_4 = 2.36$  and not the cw=1 curve averages over lower curve change a bit. If you argue that lower curve still takes into account  $\beta_1$  then forget all and use only consideration with  $l=0$ .

#### 4.6.5 Vector triplet

We will consider solutions of equations 3.94, 3.95 and 3.96. For simplicity we assume that there is no mass splitting between the neutral and charged state of the resonance. As for the singlet case parameters  $k_\rho, k'_\rho$  and  $k''_\rho$  are ignored, as well as the coefficients of the magnetic

$f_\omega = \frac{\Gamma_\omega}{M_\omega}$	1.0	0.8	0.6	0.3
$M_\omega$ [TeV]	2.22	2.10	1.95	1.63

Table 4.23: Mass limit for vector resonance. Values in the table are average values along the lower limit in the range 0 till 2.36

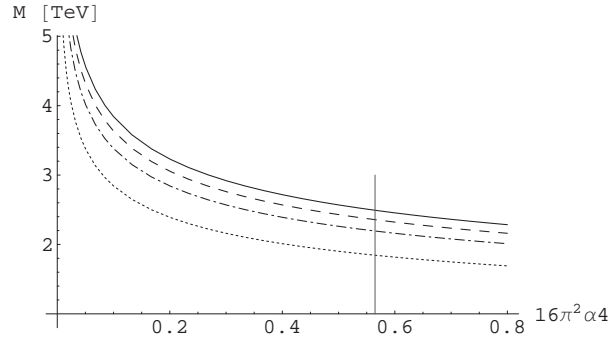


Figure 4.25: Dependence of the resonance mass for the vector triplet on  $\alpha_4$  for different assumed widths (in red  $f = \Gamma/M_\rho = 1.0$ , blue 0.8, green 0.6, brown 0.3). The red vertical line represents the  $1\sigma$  limit for  $\alpha_4$ .

moment operators of the heavy resonances,  $\mu$  and  $\mu'$ .

### Isospin conservation

Considering system of equation we get the usual relation between the couplings

$$\alpha_4 = -\alpha_5 \quad (4.43)$$

For the  $\alpha^\lambda$  couplings we get

$$\alpha_1^\lambda = 3\alpha_3^\lambda \quad (4.44)$$

leading to the solution in pure isospin conserving case :

$$M_\rho = v \left( \frac{12\pi\alpha_4 f_\rho}{\alpha_4^2 + 2(\alpha_2^\lambda)^2} \right)^{\frac{1}{4}} \quad (4.45)$$

while for  $l'$  switched on we have

$$M_{\rho^\pm} = v \left( \frac{12\pi\alpha_4 f_{\rho^\pm}}{\alpha_4^2 + 2(\alpha_2^\lambda)^2 + \frac{1}{2} \frac{s_W^2}{c_W^2} (\alpha_4^\lambda)^2} \right)^{\frac{1}{4}} \quad (4.46)$$

$$M_{\rho^0} = v \left( \frac{12\pi\alpha_4 f_{\rho^0}}{\alpha_4^2 + 2(\alpha_2^\lambda)^2} \right)^{\frac{1}{4}} \quad (4.47)$$

The case  $l_\rho = 0$  (i.e.  $\alpha_2^\lambda = 0$ ) brings us apparently back to the soliton for the vector singlet case. But now the correlations among the parameters are different especially  $\alpha_6 = \alpha_7 = 0$  that is not the case for the singlet. The assumption  $g_\rho = 0$ ,  $h_\rho \neq 0$  leads to the same result. Result for these case are shown in Table.4.6.5 and Figure.4.25.

### Isospin violation

In general case relations that hold between the couplings are:

$$\alpha_4 = -\alpha_5, \quad \alpha_6 = -\alpha_7 \quad (4.48)$$

$f = \frac{\Gamma}{M_\rho}$	1.0	0.8	0.6	0.3
$M_\rho$ [TeV]	2.49	2.36	2.19	1.84

Table 4.24: Mass reach for the vector triplet if  $g_\rho$  or  $h_\rho$  are zero depending on different resonance widths, with assumption  $l_\rho = l'_\rho = l''_\rho = 0$

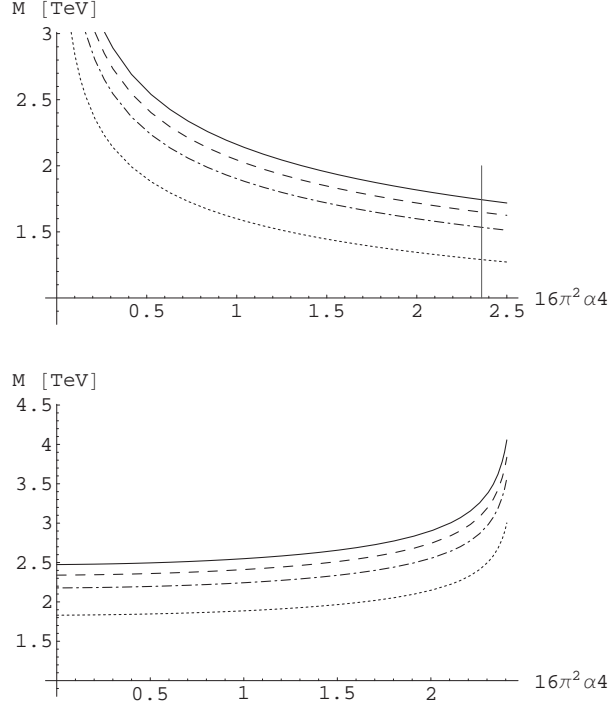


Figure 4.26: Dependence of the resonance mass for the vector triplet on  $\alpha_4$  for different assumed widths (in red  $f = \Gamma/M_{\rho^+} = 1.0$ , blue 0.8, green 0.6, brown 0.3). On the left for neutral component and on the right for charged one.

$$\alpha_1 = \alpha_4 + \alpha_6, \quad \alpha_8 = -\frac{\alpha_6}{2} \left( 1 + \frac{\alpha_6}{2(\sqrt{\alpha_1} + \sqrt{\alpha_4})^2} \right) \quad (4.49)$$

$$2(\alpha_1^\lambda + \alpha_2^\lambda) = - \left( 1 + \sqrt{\frac{\alpha_1}{\alpha_4}} \right) (2\alpha_3^\lambda + \alpha_4^\lambda) \quad (4.50)$$

At first lets consider all  $k_\rho$  and  $l_\rho$  are zero. Solution yealds:

$$M_{\rho^\pm} = v \left( \frac{12\pi\alpha_4 f_{\rho^\pm}}{\alpha_4 + \alpha_6} \right)^{\frac{1}{4}} \quad (4.51)$$

$$M_{\rho^0} = v \left( \frac{12\pi\alpha_4 f_{\rho^0}}{\alpha_4} \right)^{\frac{1}{4}} \quad (4.52)$$

Dependence of the mass on the couplings is shown on the Fig.4.26 and summarized in the Table.4.6.5

$f = \frac{\Gamma}{M_\rho}$	1.0	0.8	0.6	0.3
$M_{\rho^\pm}$ [TeV]	2.67	2.53	2.35	1.98
$M_{\rho^0}$ [TeV]	1.74	1.65	1.53	1.29

Table 4.25: Mass reach for the vector triplet with assumption  $l_\rho = l'_\rho = l''_\rho = 0$ . Values for charged component are averaged over lower limit

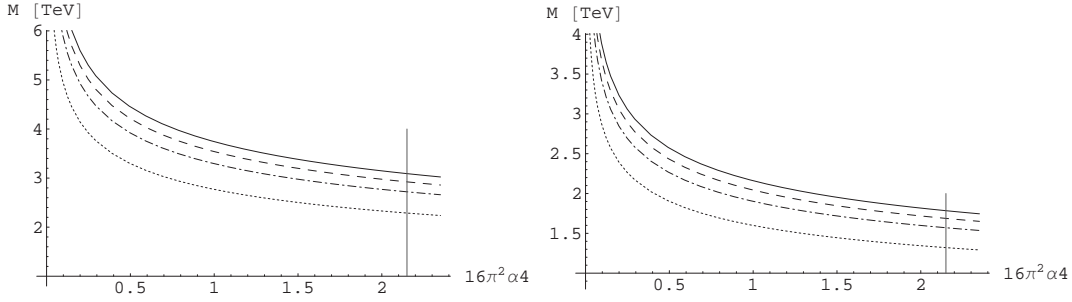


Figure 4.27: Dependence of the resonance mass for the vector triplet on  $\alpha_4$  for different assumed widths (in red  $f = \Gamma/M_{\rho^+} = 1.0$ , blue 0.8, green 0.6, brown 0.3) for  $g = -h$  case. On the left for charged and on the right for neutral one.

There is a special case for the solution when  $g_\rho = -h_\rho$ , relation between the coupling simplify to:

$$\alpha_1 = \frac{13}{\alpha_2} = -\alpha_3 = \frac{19}{\alpha_4} = -\frac{18}{\alpha_6} = \frac{12}{\alpha_9} \quad (4.53)$$

this leads to the mass solutions in the form:

$$M_{\rho^\pm} = v \left( \frac{108\pi f_{\rho^\pm}}{\alpha_4} \right)^{\frac{1}{4}} \quad (4.54)$$

$$M_{\rho^0} = v \left( \frac{12\pi f_{\rho^0}}{\alpha_4} \right)^{\frac{1}{4}} \quad (4.55)$$

with results presented in Fig.4.27 and Table.4.6.5.

Still assuming  $g_\rho = -h_\rho$  we can now allow non-zero values for  $l_\rho$  and  $l'_\rho$ . As in vector singlet case we need additional measurements in order to solve the system. Using results for  $\lambda^Z$  and  $\lambda^\gamma$  form [73] assuming  $l''_\rho = 0$  we have solvable system. Constructing the  $\chi^2$  distribution for the triple couplings and requesting that variables are connected with condition  $\chi^2 = \chi_{min}^2 + 1$  can solve for the masses although only numerically due to the polynomial equation of higher order. Results are in the Table.4.6.5 and Fig.4.28 and Fig.4.29. If we allow  $\mu \neq \mu' \neq 0$  this

$f = \frac{\Gamma}{M_\rho}$	1.0	0.8	0.6	0.3
$M_{\rho^\pm}$ [TeV]	3.09	2.92	2.72	2.29
$M_{\rho^0}$ [TeV]	1.78	1.69	1.57	1.32

Table 4.26: Mass reach for the vector triplet with assumption  $g = -h$ .

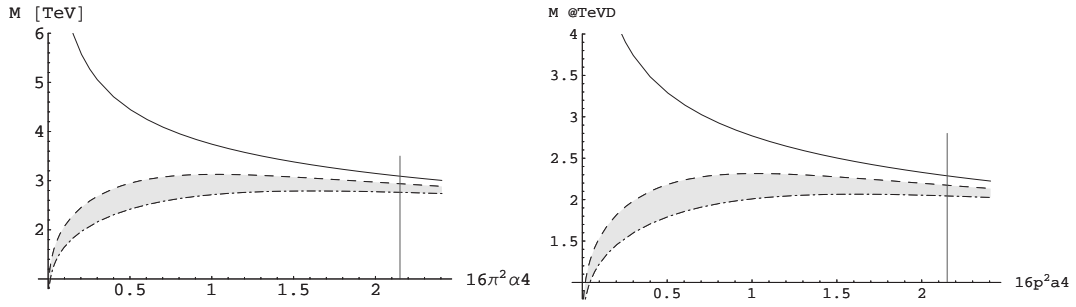


Figure 4.28: Dependence of the resonance mass for charged component of the vector triplet on  $\alpha_4$  for different assumed widths ( $f=1$  on the left and  $f=0.3$  on the right) for  $g_\rho = -h_\rho$  case. Full line represent the case when  $l_\rho = l'_\rho = l''_\rho = 0$ , and the dashed one minimal value when we allow  $l_\rho \neq l'_\rho \neq 0$ . The grey shaded area becomes allowed if  $\mu_\rho, \mu'_\rho \neq 0$ .

$f = \frac{\Gamma}{M_\rho}$	1.0	0.8	0.6	0.3
$M_{\rho^\pm}$ [TeV]	2.91	2.75	2.56	2.16
$M_{\rho^0}$ [TeV]	1.84	1.79	1.66	1.40

Table 4.27: Mass reach for the vector triplet with assumption  $g = -h$  with  $l_\rho \neq l'_\rho \neq 0$ . Values in the table are average values along the lower limit

leads to 10% reduction in the lower limit but without putting any constrain on to the values of  $\mu$ .

#### 4.6.6 Tensor singlet

Considering system of equations eq.3.97 and eq.3.98 we have following possible solutions:

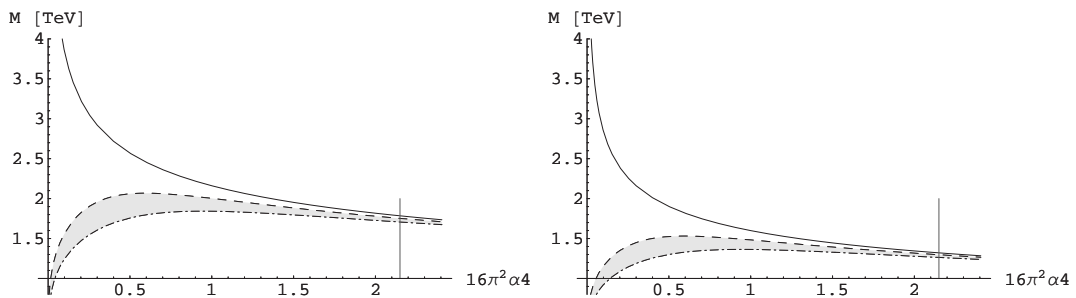


Figure 4.29: Dependence of the resonance mass for neutral component of the vector triplet on  $\alpha_4$  for different assumed widths ( $f=1$  on the left and  $f=0.3$  on the right) for  $g_\rho = -h_\rho$  case. Full line represent the case when  $l_\rho = l'_\rho = l''_\rho = 0$ , and dashed one minimal value when we allow  $l_\rho \neq l'_\rho \neq 0$ . The grey shaded area becomes allowed if  $\mu_\rho, \mu'_\rho \neq 0$

$f = \frac{\Gamma}{M_\rho}$	1.0	0.8	0.6	0.3
$M_{\rho^\pm}$ [TeV]	2.54	2.41	2.34	1.88
$M_{\rho^0}$ [TeV]	1.71	1.62	1.51	1.27

Table 4.28: Mass reach for the vector triplet with assumption  $g = -h$  with  $l_\rho \neq l'_\rho \neq 0$  when  $\mu \neq \mu' \neq 0$ . Values in the table are average values along the lower limit

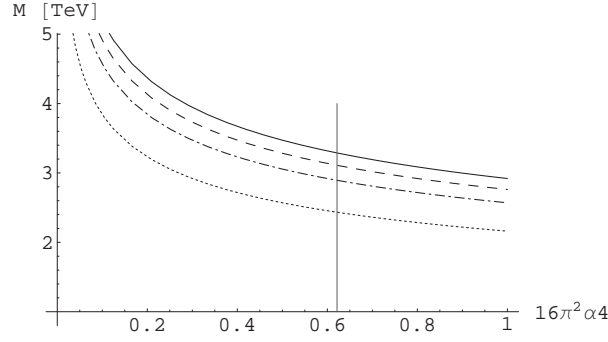


Figure 4.30: Dependence of the resonance mass for the tensor singlet case on  $\alpha_4$  for different assumed widths (full line  $f = \Gamma/M = 1.0$ , dashed 0.8, dot-dashed 0.6, dotted 0.3).

### Isospin conservation

For this case  $\alpha_4$  and  $\alpha_5$  are non-zero but related with:

$$\alpha_5 = -\frac{1}{4}\alpha_4 \quad (4.56)$$

Choosing  $\alpha_4$  as fit variable we get  $\alpha_4 = 0.64369$  for parabolic error and  $-0.65404 < \alpha_4 < 0.62154$  for asymmetric errors at  $1\sigma$  level. Mass dependence on the coupling is then given by:

$$M = v \left( \frac{40\pi f}{\alpha_4} \right)^{\frac{1}{4}} \quad (4.57)$$

Results for this case are shown on the Fig.4.30 and in Table.4.6.6.

### Isospin breaking

In this case  $\alpha_6, \alpha_7$  and  $\alpha_{10}$  are also nonzero but with constrains:

$$\alpha_4 = -4\alpha_5 \ \& \ 2\alpha_{10}\alpha_5 = -3\alpha_7^2 \ \& \ \alpha_6 = -4\alpha_7 \quad (4.58)$$

$f = \frac{\Gamma}{M}$	1.0	0.8	0.6	0.3
$M$ [TeV]	3.29	3.11	2.89	2.43

Table 4.29: Mass reach for the tensor singlet in the  $SU(2)_c$  conserving case depending on different resonance widths.

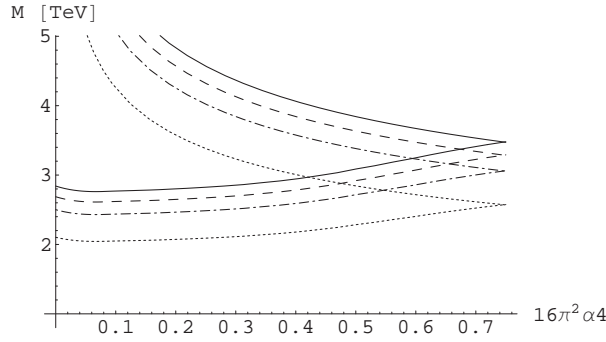


Figure 4.31: Dependence of the resonance mass for the tensor singlet case on  $\alpha_4$  for different assumed widths (full line  $f = \Gamma/M = 1.0$ , dashed 0.8, dot-dashed 0.6, dotted 0.3).

$f = \frac{\Gamma}{M}$	1.0	0.8	0.6	0.3
$M$ [TeV]	3.00	2.84	2.64	2.22

Table 4.30: Mass reach for the tensor singlet in the broken isospin case depending on different resonance widths. Values in the table are average values along the lower limit.

From which it is easy to see that these conditions reduce to the eq.4.56 in case of zero values for  $\alpha_6, \alpha_7$  and  $\alpha_{10}$ . From initially five coupling we have only two independent. We choose to take  $\alpha_4$  and  $\alpha_6$  as such. Then the mass of the tensor singlet is given by:

$$M = v \left( \frac{120\alpha_4\pi f}{2\alpha_4^2 + (\alpha_4 + \alpha_6)^2} \right)^{\frac{1}{4}} \quad (4.59)$$

maximum of equation eq. 4.59 we obtain when  $\alpha_4 = -\alpha_6$  leaving us once again with only one parameter fit and mass relation in the form eq. 4.60, that gives the upper limit for given  $\alpha_4$ .

$$M = v \left( \frac{60\pi f}{\alpha_4} \right)^{\frac{1}{4}} \quad (4.60)$$

Mass reach is shown in Fig.4.31 and Table 4.6.6.

#### 4.6.7 Tensor triplet

Considering possible solutions of the system eq.3.99,3.100, as for the scalar triplet there is no isospin conserving solution but there are several special case in isospin breaking scenario.

(a) If one assumes  $h_a = k_a = 0$  and  $h'_a$  is only non vanishing parameter, isospin breaking does not show up experimentally and solution solution formally reduces to the one for the isospin-conserving tensor singlet case:

$$M_{a^0} = v \left( \frac{40\pi f_{a^0}}{\alpha_4} \right)^{\frac{1}{4}} \quad (4.61)$$

Since relation between the coupling is identical ( $\alpha_4 = -4\alpha_5$ ) both fit and resulting limits are identical as those in Fig.4.30 and in Table.4.6.6.

$f_a = \frac{\Gamma_a}{M_a}$	1.0	0.8	0.6	0.3
$M_{a^0}$ [TeV]	3.01	2.85	2.65	2.23
$M_{a^\pm}$ [TeV]	3.48	3.29	3.06	2.57

Table 4.31: Dependence of the mass reach for tensor triplet resonances on different resonance widths. For neutral component numbers in the table are average values along the lower limit.

(b) In most general situation with all considered coupling non vanishing we get following constrains:

$$\alpha_4 = -4\alpha_5 \ \&\& \ (2\alpha_6 - \alpha_7)^2 = \frac{9}{2}\alpha_4(\alpha_6 + 4\alpha_7 + 3\alpha_{10}) \quad (4.62)$$

that are used to eliminate  $\alpha_5$  and  $\alpha_{10}$  from the system giving the mass solutions:

$$M_{a^\pm} = v \left( \frac{60\pi f_{a^\pm}}{\alpha_4} \right)^{\frac{1}{4}} \quad (4.63a)$$

$$M_{a^0} = v \left( \frac{9720\pi\alpha_4 f_{a^0}}{162\alpha_4^2 + (9\alpha_4 + 8\alpha_6 - 4\alpha_7)^2} \right)^{\frac{1}{4}} \quad (4.63b)$$

In this case we have three independent couplings thus we have  $1\sigma$  volume. For the charged component Situation was rather simple after the fit knowing the error matrix we construct  $\chi^2$  that is depending on three variables  $\alpha_4, \alpha_6$  and  $\alpha_7$ . Condition that up value of  $\chi^2$  corresponds to the  $1\sigma$  limit reduces number of free variables to 2. This allow us to plot Mass dependence on the single variable since for a given  $\alpha_4$  within the fit limits one calculates value of  $\alpha_7$  subtitles them in mass equation and plots. For the neutral component case this in not enough to pick triplet of points thus additional condition  $9\alpha_4 + 8\alpha_6 - 4\alpha_7$  is introduces. Fixing third variable along this surface that guarantees the maximum of eq.4.63a we can do the explained thick again and plot mass dependence on one coupling only. Note that in this case solution for the neutral state becomes:

$$M_{a^0} = v \left( \frac{60\pi f_{a^0}}{\alpha_4} \right)^{\frac{1}{4}} \quad (4.64)$$

Minimum within the  $1\sigma$  volume we get on the surface of  $9\alpha_4 + 8\alpha_6 - 4\alpha_7 = 0$  when the solution for the neutral component becomes same as for the charged component. This condition is equivalent to the  $h'(h' + h + 2k) = 0$ , and  $h'_a$  cannot be zero since otherwise we do not have any solution at all. Results are shown in Fig.4.32 Fig.4.33 and in table 4.6.7.

## 4.6.8 Tensor quintet

### Isospin conservation

From system of equations (eq.3.101 and eq.3.102) after checking for nontrivial solution where  $\alpha_4$  and  $\alpha_5$  are non-zero we get the following set of constrains

$$g_t \neq 0, \ h_t = k_t = h'_t = 0 \quad (4.65)$$

$$h'_t \neq 0, \ g_t = k_t = h_t = 0 \quad (4.66)$$

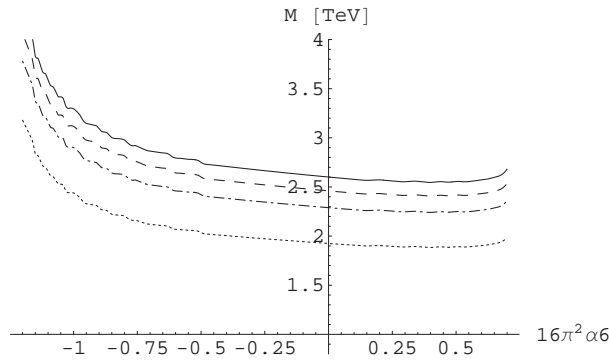


Figure 4.32: Dependence of the resonance mass for the charged component of triplet on  $\alpha_4$  for different assumed widths  $f = \Gamma/M = 1.0$  full,  $e$  0.8 dashed, 0.6 dot-dashed, 0.3 dotted). Vertical line represents the  $1\sigma$  limit for  $\alpha_4$ .

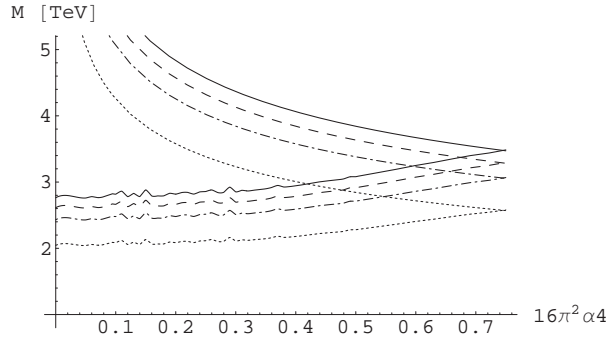


Figure 4.33: Dependence of the resonance mass for the neutral component of triplet on  $\alpha_4$  for different assumed widths ( $f = \Gamma/M = 1.0$  full,  $e$  0.8 dashed, 0.6 dot-dashed, 0.3 dotted).

$$h'_t = h_t = 0, \quad g_t = -2k_t \quad (4.67)$$

$$h'_t = 0, \quad g_t = k_t = -\frac{1}{2}h_t \quad (4.68)$$

$$h'_t = 0, \quad g_t = 2k_t = -\frac{1}{2}h_t \quad (4.69)$$

In all possible combinations relation  $\alpha_5 = 2\alpha_4$  holds, except for the case from eq.4.66 where it is  $\alpha_5 = -\frac{1}{4}\alpha_4$ . This leads to two distinct solutions (a) First one is strict isospin conservation (eq.4.65). Solving for mass yields

$$M_t = v \left( \frac{30\pi f_t}{\alpha_4} \right)^{\frac{1}{4}} \quad (4.70)$$

After elimination of  $\alpha_5$  and fit we obtain  $\alpha_4 = 0.16116$  as a parabolic error and  $-0.17387 < \alpha_4 < 0.15134$  as asymmetric once at  $1\sigma$ . Results are shown in Fig.4.34 and Table.4.32. Same result we get for cases where  $h'_t = 0$  that are experimentally unobservable as isospin breaking cases.

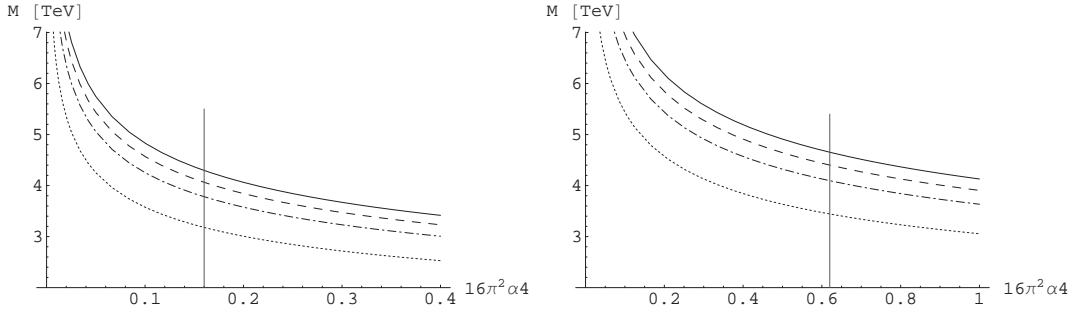


Figure 4.34: Dependence of the resonance mass for the tensor quintet b) case on  $\alpha_4$  for different assumed widths (in red  $f = \Gamma/M_t = 1.0$ , blue 0.8, green 0.6, brown 0.3). The red vertical line represents the  $1\sigma$  limit for  $\alpha_4$ .

$f = \frac{\Gamma}{M_t}$	1.0	0.8	0.6	0.3
$M_t$ [TeV]	4.30	4.06	3.78	3.18

Table 4.32: Mass reach for the tensor singlet in the  $SU(2)_c$  conserving case b) depending on different resonance widths.

### Isospin breaking

a)  $g_t = k_t = h_t = 0$   $hp = free$  in this case we have contribution only to the width of neutral member. Relation between the couplings is  $\alpha_5 = -\frac{1}{4}\alpha_4$ . Mass dependence is

$$M_{t0} = v \left( \frac{60\pi f_t}{\alpha_4} \right)^{\frac{1}{4}} \quad (4.71)$$

c) special case  $h_t = k_t = 0$  leads to

$$\alpha_6 = -4\alpha_7 \quad 81\alpha_7^2 = 2\alpha_4^2 + 7\alpha_4\alpha_5 - 4\alpha_5^2 \quad (4.72)$$

$$M_{t^c} = v \left( \frac{270\pi f_{t^c}}{\alpha_4 + 4\alpha_5} \right)^{\frac{1}{4}} \quad (4.73)$$

$$M_{t^0} = v \left( \frac{270\pi f_{t^0}}{5\alpha_4 + 2\alpha_5} \right)^{\frac{1}{4}} \quad (4.74)$$

(d) In completely general case all couplings are non-zero and the constraint equation is

$$(2\alpha_6 - \alpha_7)^2 = (2\alpha_4 - \alpha_5)(\alpha_4 + 4\alpha_5 + 2\alpha_6 + 8\alpha_7 + 6\alpha_10) \quad (4.75)$$

$f = \frac{\Gamma}{M_{t0}}$	1.0	0.8	0.6	0.3
$M_{t0}$ [TeV]	4.65	4.40	4.10	3.44

Table 4.33: Mass reach for the tensor singlet in the  $SU(2)_c$  conserving case a) depending on different resonance widths.

$f = \frac{\Gamma}{M_t}$	1.0	0.8	0.6	0.3
$M_{tc}$ [TeV]	6.76	6.39	5.95	5.00
$M_{t^0}$ [TeV]	4.53	4.28	3.98	3.35

Table 4.34: Mass reach for the tensor quintet in the  $h = k = 0$  case depending on different resonance widths. Values in the table are average over lower limit.

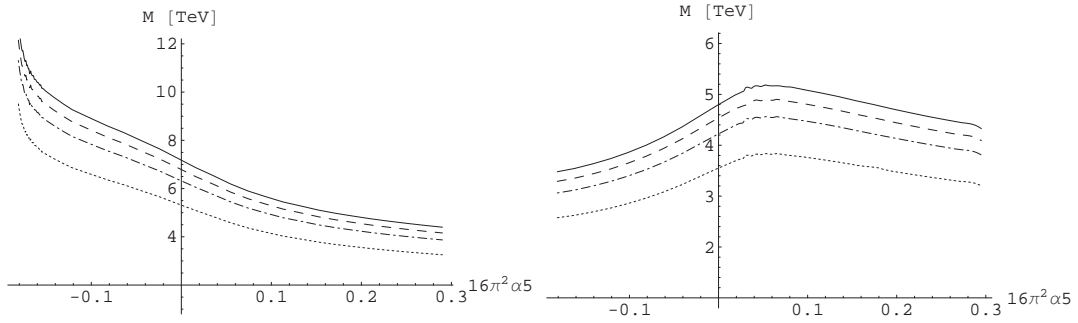


Figure 4.35: Dependence of the resonance mass for the tensor quintet in case  $h = k = 0$  for different assumed widths (in red  $f = \Gamma/M_t = 1.0$ , blue 0.8, green 0.6, brown 0.3)

solving for masses yealds

$$M_{t^{\pm\pm}} = v \left( \frac{270\pi f_{t^{\pm\pm}}}{\eta_{45}} \right)^{\frac{1}{4}} \quad (4.76)$$

$$M_{t^{\pm}} = v \left( \frac{270\pi f_{t^{\pm}}}{\eta_{45} + \eta_{67}} \right)^{\frac{1}{4}} \quad (4.77)$$

$$M_{t^0} = v \left( \frac{810\pi f_{t^0}}{[\sqrt{\eta_{45}\zeta_{45}} - 2\zeta_{45}]^2 + 2[\zeta_{45} + \zeta_{67}]^2} \right)^{\frac{1}{4}} \quad (4.78)$$

with abbreviations  $\eta_{ij} = \alpha_i + 4\alpha_j$  and  $\zeta_{ij} = 2\alpha_i - \alpha_j$ .

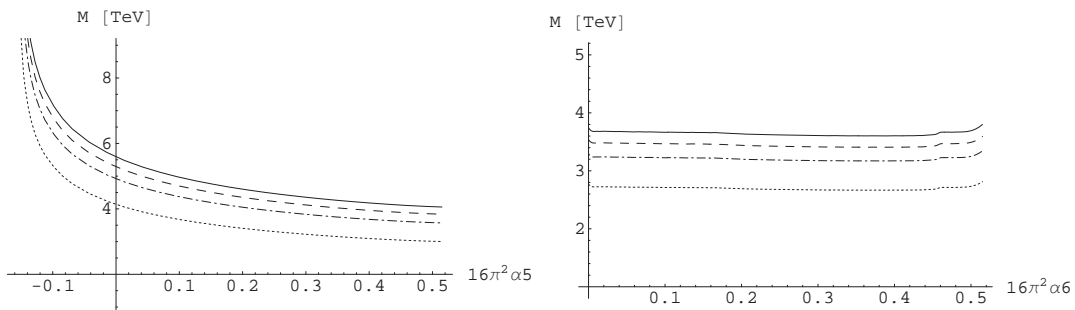


Figure 4.36: Dependence of the resonance mass for the tensor quintet doubly charged case left, charged case right for different assumed widths ( $f = \Gamma/M_t = 1.0$  full line, 0.8 dashed, 0.6 dot-dashed, 0.3 dotted)

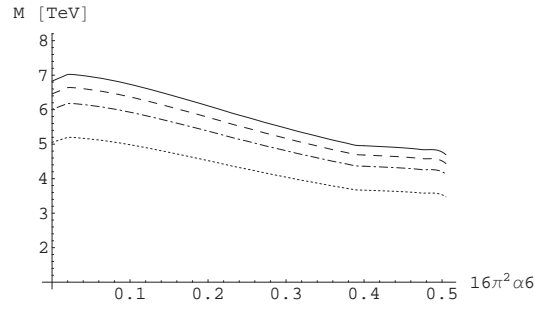


Figure 4.37: Dependence of the resonance mass for the tensor quintet neutral case for different assumed widths ( $f = \Gamma/M_t = 1.0$  full line, 0.8 dashed, 0.6 dot-dashed, 0.3 dotted)

$f = \frac{\Gamma}{M_t}$	1.0	0.8	0.6	0.3
$M_{t\pm\pm}$ [TeV]	5.17(4.06)	4.89(3.84)	4.55(3.57)	3.83(3.00)
$M_{t\pm}$ [TeV]	3.64	3.44	3.20	2.69
$M_{t0}$ [TeV]	5.84	5.52	5.14	4.32

Table 4.35: Mass reach for the tensor quintet in the full case depending on different resonance widths. Values in the table are average over lower limit. In brackets minimal value along the lower limit

## 4.7 Summary

At an ILC with high energy (1TeV) and luminosity ( $1ab^{-1}$ ) and possibility for both electron and positron polarization, precise measurement of weak boson interactions will be feasible. In Table.4.7 and Table.4.7 results are combined for all spin and isospin channels. Table.4.7 assumes  $SU(2)_c$  conservation, so the  $\Delta\rho$  parameter automatically vanishes. In this case only channels with I+J even couple to weak boson pairs. Table.4.7 shows results without this constrain. In each case, a single resonance with maximal coupling (i.e.  $\Gamma = M$ ) was assumed to be present. In a real situation particular structure of the parameter dependence can be used to disentangle multiple resonances. Amount of information that can possibly be gained on top of the analysis of fermionic couplings, or otherwise if such couplings are small or absent. In this case only operator that scales with  $1/M^2$  corresponds to the  $\rho$  parameter associated to custodial-SU(2) violation. Apart from that, all  $1/M^2$  effects in bosonic interactions can be absorbed into unobservable redefinition of the SM parameters. All shifts due to heavy resonances in oblique corrections, triple gauge couplings and quartic couplings scale with  $1/M^4$ . Taking these consideration into account, We find limits for the sensitivity of the ILC in the 1 to 3TeV range, where the best reach corresponds to the highest spin/isospin channel. These limits are not as striking as possible limits from contact interactions, but they agree well with the expected direct search limits for resonances at LHC. Performing global fits of all electroweak parameters, analogous to LEP analysis, and combining data from both experiments well be important for disentangling the contributions. Significant knowledge about the mechanism of electroweak symmetry breaking can thus be gained even in the case when no new particle content of the theory is discovered.

Spin	I=0	I=1	I=2
0	1.55	-	1.95
1	-	2.49	-
2	3.29	-	4.30

Table 4.36: Accessible scale in TeV for all possible spin/isospin channels. Custodial SU(2) symmetry is assumed to hold.

Spin	I=0	I=1	I=2
0	1.39	1.55	1.95
1	1.74	2.67	-
2	3.00	3.01	5.84

Table 4.37: Accessible scale in TeV for all possible spin/isospin channels. Custodial SU(2) symmetry is assumed to hold.

# Chapter 5

## Particle flow

### 5.1 The concept of particle flow

To explore the new physics described above high precision is mandatory. To achieve this a new reconstruction concept, which has a significant impact on the detector design that is in development.

The LEP experiments introduced the so called "energy-flow method". It consists of the reconstruction of "pseudo-particles"- an approximation to single particle reconstruction in order to enhance detector performance. Enhancement of the performance comes from the fact that when combining information from the tracker and calorimeter we can re-weight them according to the precision that they are measured with and not treat them equally. The logical consequence of Energy Flow is called "Particle Flow" (P-Flow), instead of an approximate solution we require reconstruction of 4-momenta of all measurable particles. It has two major ingredients: **separation** of the showers within the calorimeter and **precision** in two components precision of calorimetry and the usage of the most precise measurement for the assignment of the particle momenta i.e. usage of the tracker for charged particles. The ingredients need to be achieved at the level of the detector (hardware) and at the level of reconstruction (software). Both elements are determined by the overall desired performance. Particle Flow reconstruction thus implies that instead looking at software and hardware separately in respect of the performance, we have a "detector triangle" as in Fig.5.1. Interactions of the ingredients are bidirectional and thus the chosen method for reconstruction will put con-

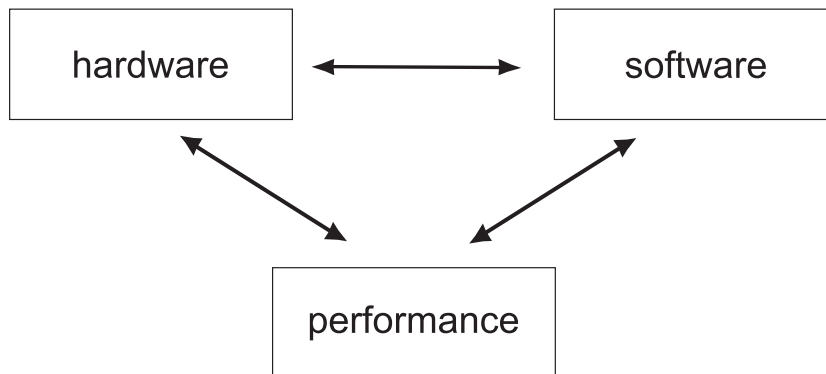


Figure 5.1: Detector performance is interplay of the used hardware and applied software reconstruction algorithm.

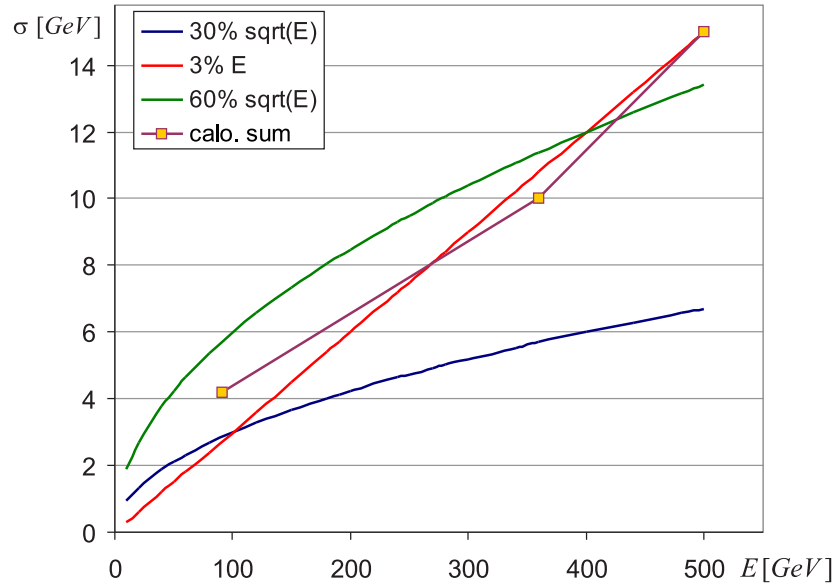


Figure 5.2: Dependence of the absolute event energy resolution for different jet energy parameterization in comparison with calorimeter sum. Points for the calorimere sum width are for different processis and the conector line is just to guide the eye.

strains on the hardware parameters and different hardware parameters will impact methods to be chosen in reconstruction governed by the performance goal that is set. In order to acheive optimal design of the detector components it is mandatory to develop an understanding of all contributions to the overall performance and to make their proper factorization. Jet energy resolution is usually expressed in the form:

$$\frac{\Delta E}{E} = \frac{a}{\sqrt{E}} \quad (5.1)$$

with the performance goal  $a=30\%$ . Recently a parameterization is introduced [20] in the form:

$$\frac{\Delta E}{E} = b \quad (5.2)$$

where  $b \sim 3 - 4\%$  driven with idea to have reconstructed width comparable with the natural width of the weak bosons, althoe it is not equivalent to the one from eq.5.1. As we can see in Fig.5.2 approximate equivalence of the parameterizations exists only around  $90\text{GeV}$ . The new parameterization (with  $b=3\%$ ) crosses the performance of the calorimeter sum in the LDC detector [78] at  $\sim 270\text{GeV}$  making concept of the Particle Flow obsolete. Not to mention that at  $\sim 400\text{GeV}$  is equivalent to the best LEP performance of  $60\%\sqrt{E}$  so there cannot be any room for “the superior performance of ILC Detector”, and we should remind ourself that such “performance” would require some 40% more luminosity for the the precision measurement for various processes [79, 80, 81, 82, 83] in comparison with performance goal of  $30\%\sqrt{E}$ . For this reason we will continue to use eq.5.1 in the following.

Table 5.1: Comparison of the calorimeter performance of the LEP and LDC detector in terms of resolution, segmentation and Perfect Particle Flow (PPF) performance.

	ALEPH	DELPHI	L3	OPAL	LDC
ECAL resolution	$\frac{18\%}{\sqrt{E}}$	$\frac{32\%}{\sqrt{E}}$	$\sim \frac{2\%}{\sqrt{E}}$	$\frac{28\%}{\sqrt{E}}$	$\frac{10(14)\%}{\sqrt{E}}$
long. segment. [ $X_0$ ]	4 and 9	$\sim 0.8 \rightarrow 3.2$	no	no	0.4(0.6),1.2
transv. segment. [cm]	$3 \times 3$	$\sim 0.34 \times 0.34$	$2 \times 2$	$10 \times 10$	$1 \times 1 (.5 \times .5)$
HCAL resolution	$\frac{85\%}{\sqrt{E}}$	$21\% + \frac{112\%}{\sqrt{E}}$	$5\% + \frac{55\%}{\sqrt{E}}$	$\frac{120\%}{\sqrt{E}}$	$\frac{50\%}{\sqrt{E}}$
long. segment. [ $\lambda$ ]	0.3	0.3	$\sim 0.35$	0.15(0.2)	0.1
transv. segment. [ $^\circ$ ]	$3.7 \times 3.7$	$3.75 \times 3.0$	$\sim 2.5 \times 2.5$	$7.5 \times 5.0$	$max(.9 \times .9)$
EFLOW [ $\%/\sqrt{E}$ ]	65	84	-	95	30*
PPF [ $\%/\sqrt{E}$ ]	34	46	-	48.5	17

### 5.1.1 Hardware parameters and Eflow reaches of LEP experiments

In chapter 2. we have already introduced the design parameters of the proposed ILC detector within the LDC concept. Here we will highlight the difference between the LEP experiment detectors and the proposed one in terms of hardware parameters and reconstruction performance from the Particle Flow point of view. In Table.5.1 the calorimeter performance of the LEP detectors ([75],[76],[77],[122],[123]) and the proposed LDC detector is summarized. The first requirement for Particle Flow is precision. If one would compare calorimeter resolutions only and chose the best sampling calorimeter already existing at LEP one would say that the proposed ECAL is close to the ALEPH one and HCAL is close to the L3 hadron calorimeter and one would not expect much difference in the performance. But if we look at the EFLOW row containing reached jet energy resolutions for LEP detectors (for hadronic events at the Zpole) and the design goal for the ILC detector (with asterix in the table) difference is obvious. Lets consider in some detail why is there a difference. The first question would be:”Not all experiments were mentioned, why?” True, there is no performance number for L3, for the reason that the tracker information was not significantly better then the calorimeter one in order to apply the method i.e. it didn’t fulfill the precision requirement. Conclusion: There is no (energy) particle flow without excellent tracking. If we assume for the moment that the remaining three have satisfied the precision criteria how can we explain the difference? In the PFLOW row we have performance limits for the full implementation of the Particle Flow algorithm on the basis of eq.5.3. Comparing the numbers one could extract a rule of thumb multiply the P-Flow performance by two to obtain the EFLOW performance. Looking at the calorimeter segmentation both in the ECAL and in the HCAL and compare it with the proposed one for the ILC detector we can see the same large difference as for the performance. The conclusion is that the remaining detectors have failed to comply with the separation requirement at the hardware level. If there is not enough separation at the hardware level only EFLOW is possible: superior momentum information from the tracker can be used only to an extent to correct the calorimeter information via the **subtraction** of momentum and the creation of pseudo particles when cluster track matching within some window is not satisfied. This provides improvement on a statistical basis and an overall gain limited by the width of the correction window defined usually proportional to the calorimeter resolutions (this is nat-

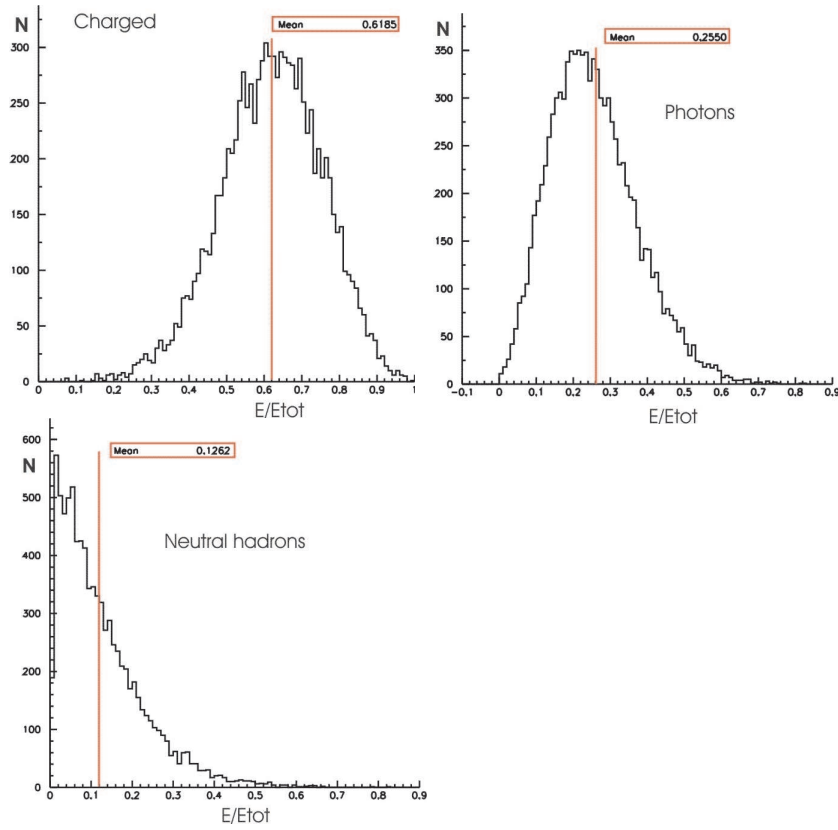


Figure 5.3: Distributions of energy fractions in different particle types for hadronic events at Zpole. Mean values marked with vertical red line.

usually a second point were precision is required). In case of Particle Flow instead of statistical correction we have **substitution** - only tracking information is used for assignment of charged particle momenta.

### 5.1.2 Jet energy resolution

As already mentioned our goal is to understand the source and relative weights of all, or at least dominant, contributions to the jet energy resolution. First considerations were made on the basis of the expression:

$$\sigma_{jet}^2 = \sigma_{\gamma}^2 * f_{\gamma} + \sigma_{had}^2 * f_{had} + \sigma_{ch}^2 * f_{ch} \quad (5.3)$$

factorizing the jet energy resolution into charged, photons and neutral hadron components. Three components are assumed to be measured by different sub-detectors i.e. charged with tracker, photons with ECAL, and neutral hadrons with HCAL. This implicitly introduces that we have full separation. The associated  $\sigma$  is one of the tracker for the charged part (effectively negligible), of the ECAL for photons and of the HCAL for the neutral hadron part of the jet. Weight factors “f” take into account relative energy fraction for the given kind of particles. Weight factor can be extracted with good accuracy from the hadronic Zpole events (since weights do not vary significantly with different final states and energies). Distributions are shown in Fig.5.3 and for calculations we will use  $f_{ch} = 0.62$ ,  $f_{\gamma} = 0.26$  and  $f_{had} = 0.12$ .

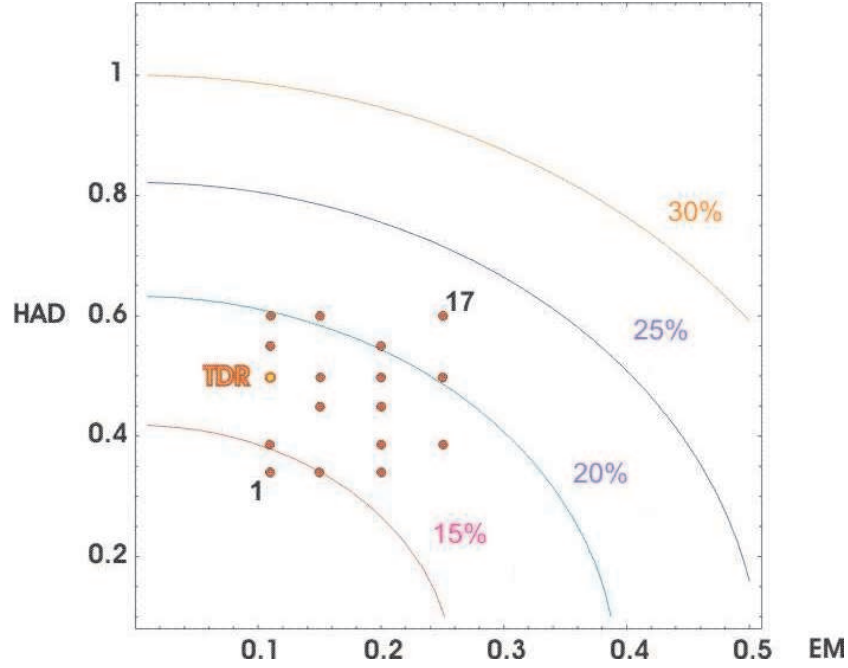


Figure 5.4: Jet energy resolutions in dependence on calorimeter resolutions according to the eq.5.3. Special point corresponding to TESLA TDR detector labeled TDR. Expected jet energy resolution according to eq.5.3 drawn with full lines.

Note that variation of the individual components are not Gaussian, so that their usage in eq.5.3 is an approximation that is valid only for central part of reconstructed distribution i.e. tails are more prominent than in the pure Gaussian case. To explain any observed deviation from the result of eq.5.3 (for example those already mentioned in Table.5.1) an additional term was introduced, the so called “confusion” term giving the final form of the equation as:

$$\sigma_{jet}^2 = \sigma_{\gamma}^2 * f_{\gamma} + \sigma_{had}^2 * f_{had} + \sigma_{ch}^2 * f_{ch} + \sigma_{conf}^2 \quad (5.4)$$

This term has lead to lot of confusion, although it was intended to describe the degradation of the reconstruction performance due to the true physical overlap of the showers in the detector, and possibly one added by reconstruction procedure. Unfortunately this term is not a direct measure of the relative weight of the leak of separation requirement of Particle Flow introduces to the reconstruction performance but a mixture of various effects as we will see in following. To check the validity of the eq.5.3 following exercise was made. Events for a few physics processes were generated ( $e^+e^- \rightarrow q\bar{q}, W^+W^-, t\bar{t}$ ) in their hadronic decay channels and center of mass energies (91.2GeV and 500GeV). Stable particles from events were separated into three categories matching the contributions in the formulae. The particle energies were smeared with resolutions according to the class that they belong and the total energy was recalculated. Due to the non-Gaussian nature of the obtained distribution the RMS was taken as a measure for the spread. In order to exclude any possible dependence of the result on the resolutions used, 17 points in ECAL, HCAL resolution space were chosen for testing as in Fig.5.4.

Since there was a similar agreement with the prediction only the result for Zpole events is shown in Table.5.2. There is rather good agreement with the prediction if we take RMS as a measure of the distribution width. But if we repeat the conditions under which such agreement has been reached:

Table 5.2: Jet energy resolution in dependence of ECAL and HCAL resolutions according to the theoretical formulae (upper number) and simple smearing for hadronic Zpole events (lower number).

<i>HCAL</i> [%]	<i>ECAL resolution</i> [%]			
	11	15	20	25
34	12.12	13.19	14.82	
	12.72	13.62	15.04	
38	13.26		15.76	17.52
	13.88		16.24	17.80
45		16.15	17.51	
		16.88	18.16	
50	16.77	17.56	18.81	20.31
	17.33	18.21	19.20	20.79
55	18.27		20.16	
	19.03		20.83	
60	19.79	20.46		22.86
	20.57	21.14		23.41

- fully spherical detector - no acceptance, no dead zones and no thresholds of any kind
- each particle was measured with the resolution appropriate to it's kind - 100% separation
- 100% reconstruction efficiency for all particles

it is clear that this result is of little practical use (if any). A significantly different factorization of effects is needed in order to get better understanding of reconstruction limits.

### 5.1.3 Contributions to the jet energy resolution

In this section we will try to introduce a different type of jet energy resolution factorization and investigate the relative weights of some of them. Final jet energy resolution is a convolution of several effects:

$$\sigma_{Ejet} = \sigma_{PPU} \oplus \sigma_{JFU} \oplus \sigma_{DG} \oplus \sigma_{PFA} \quad (5.5)$$

where PPU stands for pure physical uncertainties, DG detector geometry, JFU jet finder uncertainty and finally PFA uncertainty due to application of the reconstruction software. Pure physical uncertainty can be factorized further:

$$\sigma_{PPU} = \sigma_{\Gamma} \oplus \sigma_{lumi} \oplus \sigma_{ISR} \oplus \sigma_{\nu} \quad (5.6)$$

with contributions from particle widths  $\sigma_{\Gamma}$ , luminosity curve  $\sigma_{lumi}$ , initial state radiation  $\sigma_{ISR}$  and energy lost to the neutrinos  $\sigma_{\nu}$ . Additionally we can also separate contributions coming from detector geometry into those from detector acceptance and dead zones within detector acceptance:

$$\sigma_{DG} = \sigma_{toBeamTube} \oplus \sigma_{DeadZones} \quad (5.7)$$

While for the PFA contribution we can use eq.5.3 that is valid for perfect Particle Flow (PPF). We do not claim that this factorization is final and the addition of new terms is not forbidden but on the contrary desirable. The result of the eq.5.5 will depend on the particular

physical process, quality of accelerator (in particular the beam spot size and crossing angle), the detector geometry and jet finder algorithm applied. But the quality of the PFA has nothing to do with the mentioned contributions since it should be a function of the sub-detector contributions and quality of reconstruction. For the PFA quality estimate it is necessary to split the resolution into mentioned independent terms or to remove them from analysis. Quality assessment of the Particle Flow or it's comparison is possible only after such splitting. In order to perform such a quality analysis mass of the event was chosen as an estimator since it eliminates use of jet algorithm. Events were generated without ISR and with fixed center of mass energy that simplifies equation 5.5 to:

$$\sigma_{Ejet} = \sigma_{Ev} \oplus \sigma_{toBeamTube} \oplus \sigma_{DeadZones} \oplus \sigma_{PFA} \quad (5.8)$$

Following assumptions were made for detector subcomponents and it's geometry:

- ECAL resolution  $12\%/\sqrt{E}[GeV]$ ,
- HCAL resolution  $50\%/\sqrt{E}[GeV] \oplus 4\%$ ,
- TPC resolution  $0\%$ ,
- beam tube region up to  $\theta = 5^\circ$ ,
- minimal transverse momentum to reach TPC  $P_t^{min} = 0.36GeV$ .

After the generator [71] all stable particles are checked and neutrinos were removed from the list. All particles with a direction of flight less than  $5^\circ$  to the beam axes are also removed. For charged particles above this polar angle we additionally check the momentum. If the transverse momentum is less than  $P_t^{min}$  the particle is also removed - this accounts for an efficiency drop for low energy tracks and gives maximal effect that is to be expected since our efficiency is 0. Realistic tracking shows a significant drop in the performance in this energy range [84]. The  $P_t$  cut used corresponds to magnetic field of 4T and inner radius of the TPC of 0.3m. All particles that are left are then again separated in three categories charged, neutral hadrons and photons. Momenta of particles are then smeared according to the resolution of their detector (infinite precision for tracker i.e. charged particles since  $\sigma_{ch}^2 \gg \sigma_\gamma^2, \sigma_{had}^2$ ). At this stage we can introduce again the reconstruction effect that is the probability to correctly identify particles and assign their masses correctly. We choose extreme possibilities that give the maximal size of the effect, so masses of charged and neutral hadrons are 100% correct - perfect ID or none is identified and an arbitrary mass for all is assigned (in our case  $\pi^\pm$  mass for charged and  $K0_L$  mass for neutral hadrons). Effects of the correct-incorrect mass assignment are labeled  $m^0$  and  $m^\pm$  in the tables. Although some effects will introduce tails in the reconstructed distribution we want a convenient way of expressing their convolution. Relative contributions are thus expressed as Gaussian widths and their addition in squares is assumed. Two methods were used to obtain consistent numbers. Turning one effect on a time and extracting the width of the distribution, or by calculating the difference of the distribution widths:

$$(\sigma^i)^2 = (\sigma_{tot}^i)^2 - (\sigma_{tot}^{i-1})^2 \quad (5.9)$$

in the case when  $i$  effects are included  $\sigma_{tot}^i$  and in the case without a particular contribution  $\sigma_{tot}^{i-1}$  their difference equals a contribution of the investigated effect  $\sigma^i$ .

Results for events at Zpole are in Table.5.3 these will be used for explanation, for the remaining processes  $e^+e^- \rightarrow q\bar{q}, W^+W^-, t\bar{t}$  detailed tables for center of mass energy 500GeV and 1TeV are in Appendix B. From effects listed in first three are non Particle Flow contributions,

<i>Effect</i>	<i>separate</i> $\sigma$ [GeV]	<i>joined</i> $\sigma$ [GeV]	<i>total</i> $\sigma$ [GeV] (%/ $\sqrt{E}$ )	% of total
$\sigma_\nu$	0.84	0.84	0.84 ( 8.80)	12.28
$\sigma_\theta$	0.73	1.11	1.11 (11.65)	9.28
$\sigma_{P_t}$	1.36	1.76	1.76 (18.40)	32.20
$\sigma_{HCAL}$	1.40	1.40	2.25 (23.53)	34.12
$\sigma_{ECAL}$	0.57	1.51	2.32 (24.27)	5.66
$m^0$	0.53	1.60	2.38 (24.90)	4.89
$m^\pm$	0.30	1.63	2.40 (25.10)	1.57

Table 5.3: Contributions to the width of reconstructed mass distribution from different sources for Zpole events.

cms. energy	91.2GeV		500GeV		1TeV		
process	Z	Z	$W^+W^-$	$t\bar{t}$	Z	$W^+W^-$	$t\bar{t}$
$\sigma_{nonPPF}$ [GeV]	1.76	2.76	3.13	3.01	3.07	5.21	6.46
$\sigma_{PPF}$ [GeV]	1.63	3.94	4.79	4.38	6.56	6.46	6.35
$\sigma_{total}$ [GeV]	2.40	4.81	5.72	5.31	7.24	8.29	9.06
$\sigma_{total}$ [%]	25.1	21.5	25.6	23.7	22.9	26.2	28.6

Table 5.4: Particle Flow and non particle flow contributions to the total reconstructed width of an event.

and last four are particle flow contributions. In the first column results are labeled “separate” i.e. each contribution with its width is expressed in GeV. In the second column non PFA and PFA contributions are in succession joined together to get their total contribute but they were not mixed. In column “total” all contribution are subsequently added thus the last number represents the total expected width of 2.4GeV. In the last column the relative contribution of the effect under consideration is expressed in terms of his contribution to the total width defined with:

$$contribution = \frac{\sigma_i^2}{\sigma_{total}^2} \quad (5.10)$$

What can we conclude from Table.5.3? Looking at the “joined” column we can see that the total non PFA contribution has  $\sigma = 1.76GeV$  and is of same size as the PFA contribution  $\sigma = 1.63GeV$ . It states that for a perfect reconstruction and particle separation in a detector of assumed geometry there is an irreducible contribution to the total width of Zpole events that has the same order of magnitude as the one we can attribute to the Particle Flow. This is in good agreement with the rule of thumb derived in previous section (i.e. factor  $\sim 2$  to the perfect reconstruction a bit larger in LEP detector due to the additional losses and non accounted detector geometry effects). For the ILC detector (LDC) we obtain a final resolution of 25.1% that is within the design requirements (similar results were obtained for SiD and GLD detector [85, 86]). Relative weights of non PFA contributions and PFA contributions are, as stated above, process and energy dependant. This we can see in Table.5.4 It seems that at higher energies particle flow contributions are starting to be dominant and up to the effects we have included into our consideration it is possible to have performance within the requirements. We can express the contributions as a fraction of the total and compare them for different processes as in Table.5.5. For a compact presentation the contributions of acceptance  $\sigma_\theta$  and  $\sigma_{P_t}$  cut are merged into “low angle” contribution, at the same time

cms. energy	91.2GeV		500GeV	
process	Z	Z	$W^+W^-$	$t\bar{t}$
$\sigma_\nu$	12.28	2.44	1.50	6.65
$\sigma_{low\ angle}$	41.48	30.66	28.43	25.41
sum non PFA	53.76	33.10	29.93	32.07
$\sigma_{HCAL}$	34.12	40.01	51.39	54.79
$\sigma_{ECAL}$	5.66	20.95	14.40	6.95
$\sigma_{mass}$	6.56	5.95	4.28	6.19
sum PFA	46.34	66.91	70.07	67.03

Table 5.5: Overview of different contributions to the total reconstructed width of the event. All values are percent of the total width according to the eq.5.10.

both charged and neutral mass assignment are merged into the  $\sigma_{mass}$ . Looking at the HCAL and ECAL contributions one can notice a significant difference between the processes. This is an important feature of this factorization, in this way we can pinpoint processes that are stressing one part of the detector and use them for optimization of the design. It is important to mention that there are much more contributions than it is possible to introduce than those covered so far, but of importance is that we have established a framework without obscure formulations and unexplainable effects.

## 5.2 Magnetic field effects

So far in our exploration of the Particle Flow issues like calibration and magnetic field dependence were hidden from the reader in a “clever” way but that does not mean that they are not present. Already in eq.5.4 both effects are present if we explain our assumptions correctly. The magnetic field enters here in rather complex way by affecting the parameters in our factorization. Resolutions that enter the expression are single numbers for the whole detector thus they are averaged resolutions over the detector or proper correction was taken in the case of any non-uniformity of the response due to the all possible reasons including magnetic field. The second assumption that is affected is 100% efficiency of the tracker irrespective of particle energy. The efficiency curve certainly depends on the strength of magnetic field. Integration of all effects that might impact the shower separation in the confusion term intrinsically contains the field again since the field will effect the average distances on the face of the calorimeter and shower sizes. The magnetic field impact on Particle Flow via tracking was partially taken into account in previous section so here we will focus our attention on calibration effects, shower shape impact and finally full reconstruction dependence. We will try to estimate maximal impact of those indirect magnetic field effects and to stress places that could lead to the worsening of resulting performance due to the not accurate treatment of them that is specially important for the optimization stage since it could lead to the wrong conclusions.

### 5.2.1 Effects on calibration

Even in the case of a “in-air-floating” detector (as in simulation at the moment) with no dead regions and non-uniformities, high magnetic field breaks the equivalence of the barrel

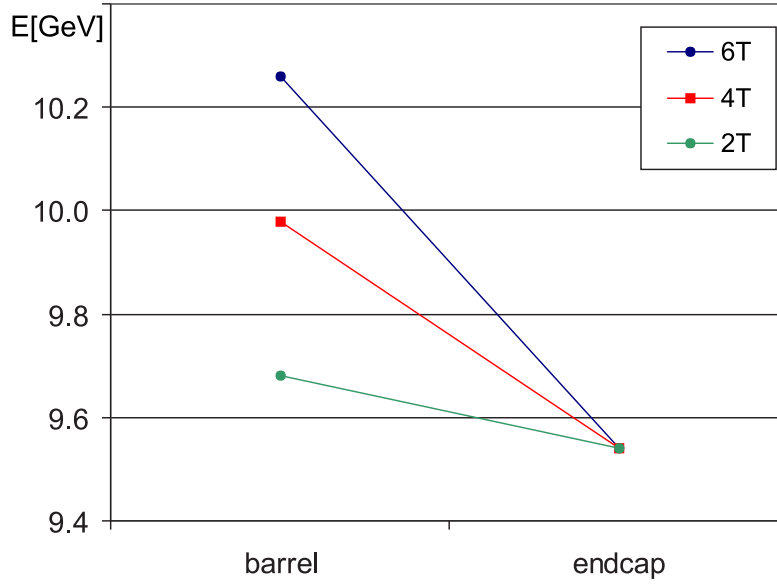


Figure 5.5: Dependence of the 10GeV photon energy calibration on the magnetic field and location in the detector.

and end cap part of the calorimeter, due the different orientation of the magnetic field to the sampling structure. For highest accuracy we need to look at higher order effects that could effect the reconstruction procedure. Initial calibration coefficients for the ECAL were extracted by shooting single photons in to the barrel part of the calorimeter at nominal field of 4T, and by adjusting position of Gaussian peak to the incoming energy:

$$E_{in} = c_1 \sum_{i=1}^n E_{hit}^i + c_2 \sum_{j=1}^m E_{hit}^j \quad (5.11)$$

where  $E_{in}$  is the incoming photon energy,  $c_1$  and  $c_2$  are calibration coefficients for first and second sampling structure in the ECAL, and the sums are going over all the hits that are in the first or second part, where  $E_{hit}$  is deposited energy in the active part of sampling structure as stored by the simulation<sup>1</sup>. Photons of 10GeV were simulated for three different magnetic fields 2, 4 and 6T. For each field two subsamples (with 10k events) were made with photons entering calorimeter perpendicular to the barrel part or perpendicular to the end cap part. It is true, that these are not situations occurring in the real event but a idea is to study the limits of what can occur in physics events to make conclusion about maximal possible effect. After the simulation the reconstructed energy was calculated, using the **same** calibration coefficients for all six cases, and put into a histogram. The mean of the Gaussian distribution is extracted by a fit. The results are shown in Fig.5.5. The overall calibration is effected by an order of 5% if one changes magnetic field between 2T and 6T in the barrel region. Difference between the barrel and the end-cap region depends on the magnetic field but it is roughly also 5%. The same procedure was repeated for  $K0_L$  and the same dependence was observed with an effect of 1% between the different fields in the barrel part and 3% for the barrel end-cap difference

<sup>1</sup>0.5 MIP threshold assumed

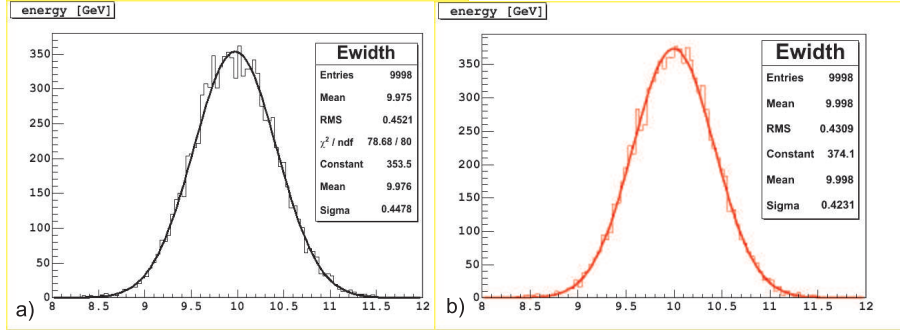


Figure 5.6: Reconstructed width for 10GeV photon for barrel part in a), and for end-cap part in b) after correction for the peak position.

at 4T. There is no ad hoc solution to the effect. The simple factor multiplication for the mean correction will return the right energy but with a different width of measured distribution as in Fig.5.6. The distributions are perfectly Gaussian but the resolution is 14.16% in barrel and 13.38% in end cap making 5.8% relative change. Only a proper initial calibration correction will give similar resolutions and this is a must if one would like to compare performance of the detector in different magnetic fields. Note that the observed effect are smaller than those from the dependence of the impact angle to the sampling structure that are of the order of 15% [87].

### 5.2.2 Effects on shower size

Does the magnetic field effect the shower sizes and the shower separation? In order to estimate the shower size change we will use following variable:

$$w = \sqrt{\frac{\sum r_i^2 E_i}{\sum E_i}} \quad (5.12)$$

where  $r$  is radial distance of the hit from the incoming direction of the particle and  $E$  is energy of the hit. Sum is going over all the hits from the simulation that are above 0.5 MIP threshold. In Fig.5.7 results for 10 GeV photons and 10GeV kaon are shown. The dependence is as expected. For the photons in the end cap the magnetic field is focusing the shower thus reducing radial width. In the barrel region the magnetic field is deflecting charged part of the shower from original direction thus increasing the width. The maximal relative change is roughly 10% for photons and neutral kaon ( $K0_L$ ) at 6T and around 5% at 4T. Thus magnetic field is effecting energy distribution within the shower. The measure for the shower radial distribution that we have used (eq.5.12) is interesting also for another reason. It is constructed in the same way as the inertia tensor:

$$I = \sqrt{\frac{\sum r_i r_j E_{hit}}{\sum E_{hit}}} \quad i, j = x, y, z \quad (5.13)$$

effectively it is the same after rotation of the coordinate system to align with the main axis of the inertia tensor. And since the determination of the inertia tensor principal axis is often used for determination of the photon direction it leads to the same type of the effect. This situation is shown in Fig.5.8. One can clearly see the one to one correlation between the

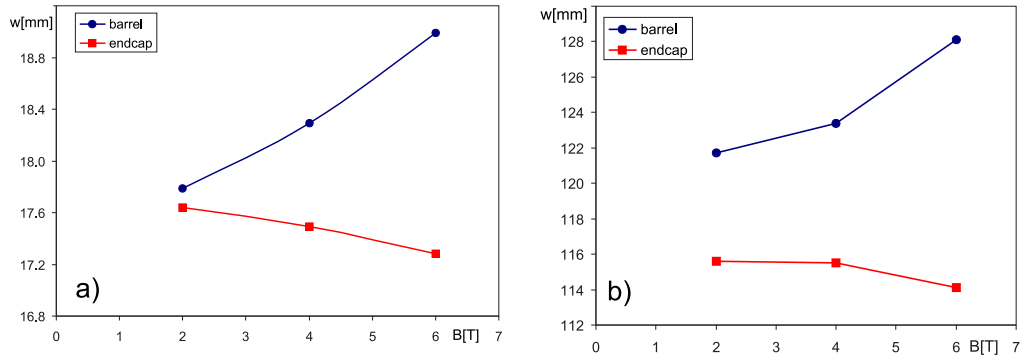


Figure 5.7: Dependence of the radial shower size on the magnetic field and part of calorimeter for 10 GeV photons left (a), and 10 GeV  $K^0_L$  right (b).

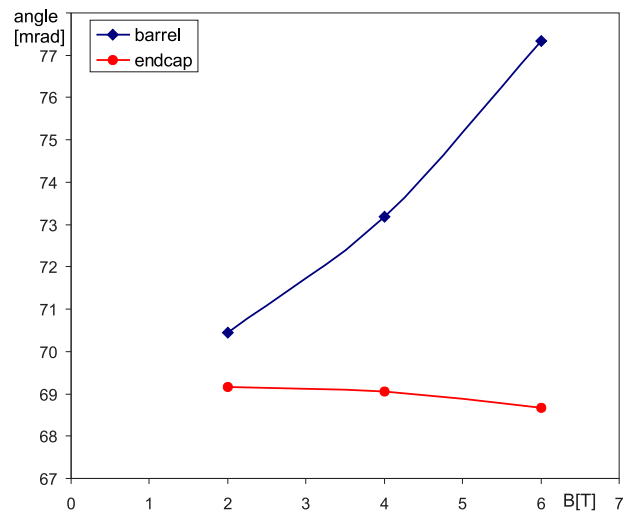


Figure 5.8: Dependence of direction determination on magnetic field for different parts of calorimeter for 10 GeV photon sample.

Fig.5.7a and Fig.5.8. If one uses such a method for the determination of the photon direction, that is not optimal, error on the direction determination will start to depend significantly on the magnetic field and part of the detector. Note that for 10GeV photons that we have used, the obtained resolution is significantly larger than the expected one (29.5mrad) for this energy [88]. One increases significantly the directional error of the reconstructed particle and violates the assumptions in the jet energy resolution estimation, that directional error is significantly smaller than the energy measurement one, leading to a worse overall performance. This is a clear indication that drawing conclusions at this point should be done very carefully so as not to attribute particular problem of the method used to test P-Flow with P-Flow in general.

### 5.2.3 Effects on full reconstruction

So far we have explained the field dependence on the level of single particles with effects on the percent level in terms of non-uniformity of the response over the detector (as from simulation) and changes in the shower sizes. Of significant interest is the detector performance in dependence on the magnetic field, since if strong, this will significantly limit room for optimization of the detector. The vertex detector and tracking resolution goal give lower limit, first due to the amount of background, second due to the achievable point resolution and number of measurement points on a fixed radius. Higher limit, except from the physical limits, is from cost, mechanical constraints and already introduced low energy track efficiency. In order to check the performance of the reconstruction on the magnetic field (that is not possible with pure calculation on the generator level), the same sample of Zpole hadronic events was passed through the full detector simulation with different magnetic fields (2,4 and 6T). After that the reconstruction was done using true information as stored by the simulation. Clusters are reconstructed by collecting the hits that belong to the particle according to their ID. In the case of several contributions to the same hit, assignment is made to the cluster of a particle with the highest contribution. Tracks were reconstructed from hits within the tracking system in same way. The only cut imposed was that the track should have at least 3 hits. After that, clusters from the charged particles were discarded if the track exist, and the true momentum was used. For neutral particles the measured energy is used and applied to the true direction. After that a search for the secondary vertices was performed through the Monte Carlo particle tree and the particles were recombined with correct mass assignment (assuming correct identification of the decaying particle). The procedure is repeated until all reconstructed objects have reached interaction point. The mass of the event is then calculated and put into a histogram. A double Gaussian fit was performed on the distributions (the first one to account for central part of the distribution, and two half-Gaussians with center fixed on to the same mean to cover for the asymmetric wings). The obtained mass distributions are in the Fig.5.9. If we take the width of the central Gaussian as the measure for the reconstructed width and also fraction of the integral that is under this distribution as an efficiency estimator, one can come to a conclusion about field dependence. **There is no B field dependence of the reconstruction if you comply with the assumptions introduced in eq.5.3**, thus this factorization is not appropriate to take into account B field effects of P-Flow.

The obtained width values (in Table 5.6) are within statistical errors (2%) and in good agreement with the expected value of 1.51GeV for a given detector (according to eq.5.3). Small drop of the efficiency at 6T is due to the effective momentum cut by our 3 hits for track condition. A objection can be made that this will not hold for the real life reconstruction. It is true but the intention was to show that there is no direct contribution term of magnetic field to the Particle Flow performance. Effects can, and should, be taken into account but this can be done through the non P-Flow contributions, introduction of averaged or effective

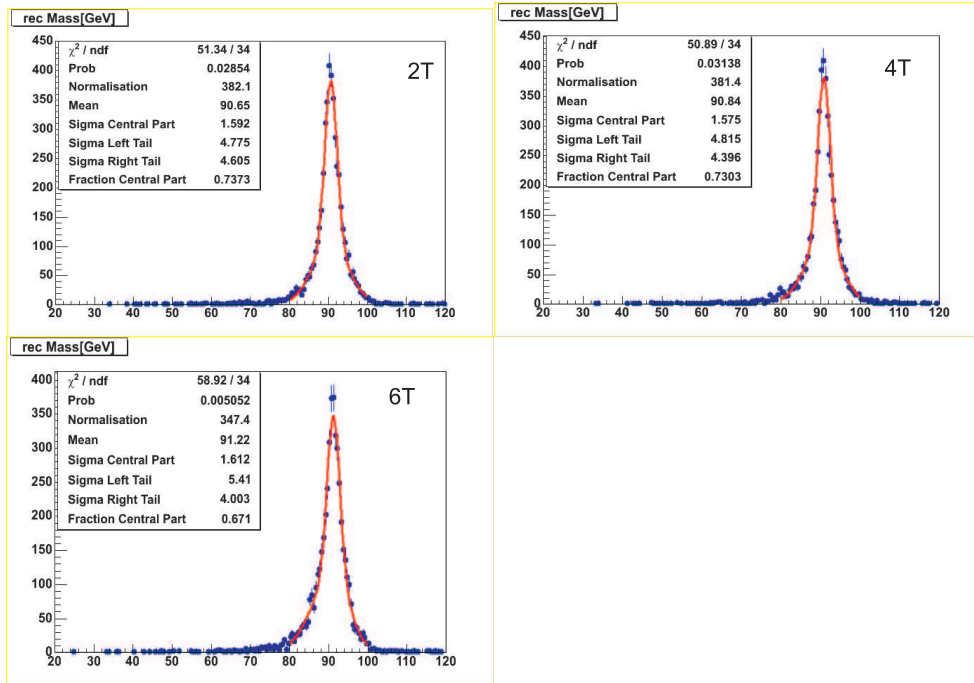


Figure 5.9: Reconstructed mass distributions for Zpole events in different magnetic fields.

Table 5.6: Dependence of perfect reconstruction on magnetic field in case of Zpole hadronic events.

B field [T]	$\sigma[GeV]$	fraction
2	1.59	0.74
4	1.58	0.73
6	1.61	0.67

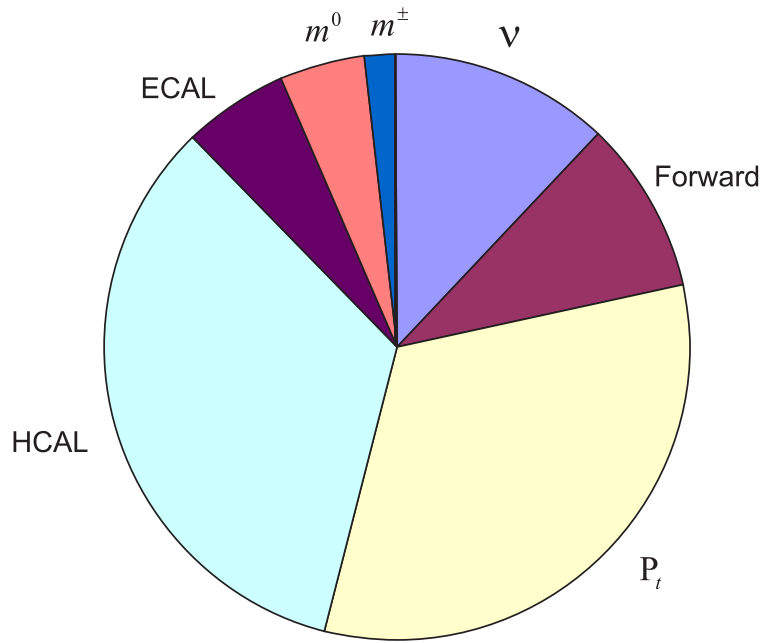


Figure 5.10: Contribution to the reconstructed width of hadronic Zpole events.

resolutions if no correction is applied, and adjusting the tracking efficiencies and acceptance cuts.

### 5.3 Conclusion

We have shown that the initial factorization of the contributions to the reconstruction performance 5.3 holds under the assumptions that is made on (5.1.2). It is thus useful to describe only perfect Particle Flow (PPF), but not applicable to the more realistic setups. For that reason factorization eq.5.5 is introduced that allows clear separation of all possible effects. Up to the level of accuracy used it was shown that  $\sim 30\%/\sqrt{E}$  goal should be reachable for all processes. An important issue of P-Flow performance is the dependence on the magnetic field, since it is directly related to the cost. We have investigated the direct field effects (on calibration and shower size), that are limited to  $\leq 5\%$  variation over the detector, and confirmed that the expression eq.5.3 holds for different fields. This leads to the conclusion that PPF is magnetic field independent. Effects from the possible breakdown of shower separation assumption and effects on the tracking efficiency acceptance can be incorporated as separate contribution in the framework established by eq.5.5. This is indeed the largest achievement of our investigation of P-Flow, that a framework is established without any misleading and confusing places. Fig.5.10 demonstrates that there are more ingredients to the picture than initially assumed, and treated so far opening room for further investigations.



## Chapter 6

# Particle Reconstruction in ILC Detector

### 6.1 Approach to Reconstruction

#### 6.1.1 Reconstruction framework

It is not possible to talk about reconstruction of single type particles in a detector without having full interconnection with rest of reconstruction procedure i.e. each particle specific method must be able to communicate with others and interchange acquired information in order to get a consistent final particle identification and best possible performance. The photon finding and reconstruction procedure that will be explained later was intended to work within a framework that has few distinct steps <sup>1</sup>:

- tracking

This part is common to all reconstruction procedures and it is not specific. The main prerequisite is to provide set of tracks with best momentum estimator at the end of the track closer to the calorimeter. Due to the lack of such information from the tracking code available Monte Carlo truth from the simulation can be used as a supplement, but the procedure does not rely on the type of the tracker used. Accurate extrapolation from the last track point till the face of the calorimeter is performed, a seed is created, the track is assigned to it and an extrapolation (with energy loss) through the calorimeter is made under assumption of energy loss for minimum ionizing particle.

- object creation and pre-clustering

Although at the end of simulation, or in the real detector, one has hits in a given format, LCIO [89] in our case, it might be preferable to change the structure containing the information or to do additional calculation and store the output before the start of full reconstruction. There are several advantages for this approach: speed, quantities that are frequently used and are not changing during execution can be calculated at early stage only once and then stored; convenience, there is a well defined place where all used attributes of any reconstruction object ( hit, cluster, seed etc.) are stored thus increasing the readability of the code (within the framework used); maximization of input information for reconstruction procedure, by doing the initial preprocessing of the objects coming into reconstruction we try to maximize input information that is

---

<sup>1</sup>These steps should not be regarded as a part of sequential procedure, at some stage of reconstruction repetition of some of them, or methods within, might be needed

available for decision making within algorithms and to follow the basic spiraling logic of highly performant reconstruction that is graduate(iterative) information collection that leads to final result.

- reconstruction in the calorimeter

The major procedure for extraction of information from the calorimeter output. This part in the case of particles producing electromagnetic shower will be explained in detail in following sections.

- estimation of physical quantities at interaction point (IP)

The event and its physical content were created at IP and the result of full reconstruction should be set of best estimators of particle momenta and energies at the IP. This part of the procedure includes finding of secondary and tertiary vertices, photon conversions and kinks. Not applying this step will lead to inevitable performance drop of any reconstruction procedure.

To the contrary of some ideas that the realization of this task is possible with separate-sequential procedure,  $30\%/\sqrt{E}$  is an ambitious goal and only a well integrated and deep event analysis can reach such performance. The accumulation of knowledge during the reconstruction procedure makes cross-jumps between any formal step in the procedure mandatory in order to minimize the introduction of errors.

### 6.1.2 Requirements for the electromagnetic shower reconstruction

We want to reconstruct electromagnetic (EM) showers in ECAL originating both from photons and from electrons or positrons. By reconstruction we assume a procedure that is both precise (returns the exact number of particles) and accurate (reproduces the intrinsic calorimeter resolution without introduction of any additional spread). Reconstruction in the ECAL is an essential part of the overall reconstruction. As shown in the previous chapter contribution of the ECAL resolution to the particle flow performance is at the  $\sim 5\%$  level assuming **full shower separation**. The fraction of event energy for dominant processes (like  $e^+e^- \rightarrow W^+W^-, t\bar{t}$ ) that is deposited in the ECAL is over 50% stressing the need to accomplish the full shower separation both on the hardware and software level to achieve minimal impact of ECAL on the final PFA performance.

There is a huge spread of EM shower energies in physics events at a given center of mass energy. There are at least three distinct sources with different energy distributions. Those are direct photons from the IP, photons from  $\pi^0$  decay, electrons and associated bremsstrahlung photons. Direct photons from the IP have exponential distribution from zero with sharply dropping probability to higher energies.  $\pi^0$  distribution is peaked, with the position of the peak moving logarithmically with growing center of mass energy. Electrons(positrons) rarely come from the hadron decays and are mostly coming directly from weak boson decays  $Z \rightarrow e^+e^-$  or  $W^\pm \rightarrow e^\pm\nu$ . Bremsstrahlung adds additional photons to the distribution and smears the initial energy distribution of electrons. Additional effect is that amount of material between the IP and the calorimeter, although small, makes photon conversion possible, introducing another specific class for reconstruction <sup>2</sup>, and additional source of electrons (positrons).

The energy distributions of electrons and photons were extracted from Zpole events passed through the full G4 detector simulation. Using the Monte Carlo information one can select various subclasses of particles entering the calorimeter. On Fig. 6.1 is the energy distribution of electrons that covers full range between zero and half of the center of mass energy. Fig. 6.2

<sup>2</sup>in fact several depending on the point of conversion

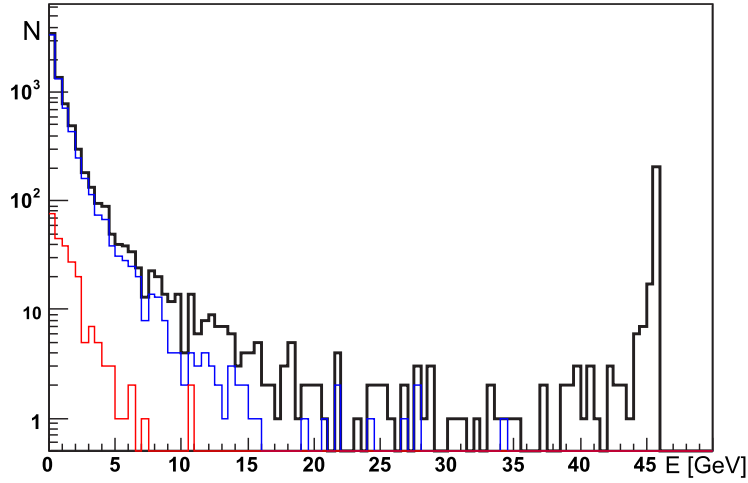


Figure 6.1: Energy distribution of electrons(positrons) entering the calorimeter for events at Zpole. In black total distribution, in blue conversion electrons, in red other decays electrons.

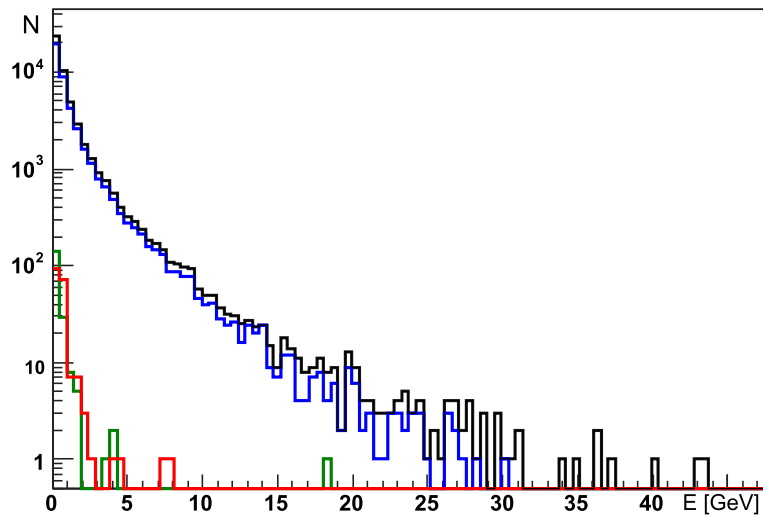


Figure 6.2: Energy distribution of photons entering the calorimeter for events at Zpole. In black total distribution, in blue photons from  $\pi^0$  decays, in red bremsstrahlung photons and in green other decay photons.

shows the distribution of photon energies with their subcomponents. Although the energy of the electromagnetic showers covers such huge range we would still prefer the reconstruction algorithm with the same “dynamic range” to be capable of uniform treatment irrespective of the incoming energy. Even though we have such energy spread one should not forget that the mean energy of the particles in the fully hadronic events, to which the reconstruction performance goal of  $30\%/\sqrt{E}$  refers, rises logarithmically with center of mass energy and even at 1TeV does not exceed 10GeV. Thus in the bulk of the cases algorithm will deal with showers with small and intermediate energies.

## 6.2 Electromagnetic Shower

From the discovery of electromagnetic showers in 1933 [90, 91], they are one of the most studied and best described phenomena in nature. Early on, significant and successful effort was made in the development of the theory [92, 93, 94, 95] due to the fact that all dominant processes are exclusively governed by quantum electrodynamics<sup>3</sup>. Together with the large number of experiments accumulated knowledge led to the development of simulation tools like EGS [101, 102, 103] that have been standard for almost 30 years (for latest comparison with data see [104]). Since we are talking about a well know facts in our introduction we will mention only the most important features with a minimal amount of detail, these can be found in the abundant literature.

The most important processes involved in the generation of electromagnetic (EM) showers are: ionization losses, Cherenkov radiation, bremsstrahlung, photoelectric effect, Compton effect and pair production (for details see [96, 97]). From mentioned processes, bremsstrahlung and pair production are dominant for high-energy electrons and photons, respectively. Their cross sections become almost energy-independent for incoming energies  $\gg \frac{m_e c^2}{\alpha Z^{1/3}}$ , where  $\alpha$  is the fine-structure constant,  $Z$  is the atomic number of the medium and  $m_e$  is the electron mass. As a consequence, the radiation length, emerges as a natural unit of length and represents the mean-path length of an electron in material and is given by:

$$\frac{1}{X_0} = 4\alpha \frac{N_A}{A} Z(Z + \zeta) r_e^2 \ln \frac{183}{Z^{1/3}} \quad [cm^2 g^{-1}] \quad (6.1)$$

where  $N_A$  is the Avogadro constant,  $A$  is atomic weight of the medium and  $r_e$  is the classical electron radius.  $\zeta$  is a correction that takes into account the contribution of atomic electrons to the overall bremsstrahlung process with values between 1.2 and 1.4 [98]. Radiation lengths have been calculated and tabulated [99]. Since we have same “natural” unit of length for electrons and photons the induced shower, shower development at same  $X_0$  thickness in different material should behave the same but this scaling is not perfect and photon and electron induced showers have to an extent different behavior [100]. We are interested in average behavior of EM showers and the usage of those properties in the reconstruction, thus the introduction of second order corrections is possible and straight forward but not necessary for our purpose at the moment. When more than one absorber is present in the showering medium, the overall radiation length can be expressed as:

$$\frac{1}{X_0} = \sum_i \frac{f_i}{X_{0i}} \quad (6.2)$$

where  $f_i$  and  $X_{0i}$  are fraction by weight and the radiation length of the absorber  $i$ , respectively. Corresponding the density can be calculated from:

$$\frac{1}{\rho} = \sum_i \frac{f_i}{\rho_i} \quad (6.3)$$

where  $\rho_i$  is the density of the  $i$ -th absorber. One of the basic answers from the theory (experiment) is how EM shower look like in terms of longitudinal and transversal profile, so we will investigate this properties in some detail.

<sup>3</sup>except for example ( $\gamma, n$ ) reaction that is totally irrelevant for basic properties of the cascade

### 6.2.1 Longitudinal development

Due to the complexity of the processes involved descriptions of the EM shower were developed with some approximations. One such model has been proposed by Rossi [105] and called “approximation B”. It takes into account radiation phenomena and pair production, together with constant collision losses per unit of length. Since one is taking into account only some processes we need a unit that is expressing in which energy range they are really dominant. Such unit is critical energy usually defined as and energy at which electron loses as much energy in collision as in radiation [106] or as energy at which the ionization loss per radiation length is equal to the electron energy [105]. One of the several approximate expressions is:

$$E_c = 2.66 \left( X_0 \frac{Z}{A} \right)^{1.1} \quad [MeV] \quad (6.4)$$

The multiplication of electrons and positrons occur when their energy is much larger than the critical energy and they get absorbed when collision losses become dominant. The number of particles increases rapidly with depth until the maximum, located at depth  $t_{max}$ , is reached i.e. the longitudinal development of the shower has a maximum. The shower behavior can be understood in a simplified way, following crude a approximation. Let  $E$  be the energy of incoming photon, which after a depth of  $\approx 1X_0$  generates  $e^+e^-$  pair of equal energy. After a additional distance  $\approx 1X_0$  both the electron and positron will emit a bremsstrahlung photon. By continuing the process, and assuming equal sharing among the generated particles, the number of them will double every radiation length. The number of particles at depth  $t$  is  $N(t) \approx 2^t$ , while their energy is  $E_p(t) \approx E/N(t) = E2^{-t}$ . When the particle energy is  $E_p \approx E_c$  multiplication will stop. This occurs at depth  $t_{max}$  for which  $E_c \approx E2^{-t_{max}}$  thus we expect that  $t_{max} \approx \ln(E/E_c)$  Under approximation B, this maximum depends on the incoming energy as  $\ln(E/E_c)$ . We can here introduce a natural variable for the expression of energy:

$$y = \frac{E}{E_c} \quad (6.5)$$

and express the position of the maximum as:

$$t_{max} = T = a(\ln(y) + c) \quad [X_0] \quad (6.6)$$

where  $a=1.01$ ,  $c_e=-1.0$  for electrons and  $c_\gamma=-0.5$  for photons as calculated by Rossi (newer more accurate calculation give  $a=1.0$ ,  $c_e=-0.5, c_\gamma=0.5$ ). Another useful parameter is the location of the center of gravity of the shower  $t_{cg}$  that is given by

$$t_{cg} = 1.01(\ln(y) + d) \quad [X_0] \quad (6.7)$$

where  $d=0.4$  or  $1.2$  for electrons or photons, respectively. Longitudinal shower distribution is approximately described by [107]:

$$\frac{dE}{dt} = \frac{(\beta t)^{\alpha-1} \beta \exp(-\beta t)}{\Gamma(\alpha)} \quad (6.8)$$

where  $\beta \approx 0.5$ . The position of the cascade maximum is then:

$$t_{max} = T = \frac{\alpha - 1}{\beta} = \ln(y) + f \quad [X_0] \quad (6.9)$$

were  $f = -0.5$  for electrons and  $0.5$  for photons. The condition for 98% longitudinal containment can be approximately given by

$$L(98\%) \approx 3t_{cg} \quad [X_0] \quad (6.10)$$

where  $t_{cg}$  is given by eq.6.7.

### 6.2.2 Transverse development

Processes neglected in the longitudinal development are responsible for the transverse development of EM showers. During the cascade development the energy is degraded into low-energy electrons via ionization, Compton scattering and photoelectric interactions, which generated electrons that dissipate their energy mainly by collision. Photoelectric and Compton scattering generate secondary electrons which are no longer aligned with the incoming photon direction and can even be emitted in the backward hemisphere in the case of photoelectric electrons. Secondary Compton photons are no longer along the primary photon direction thus contributing to the broadening of the cascade. Coulomb scattering of electrons that are not radiating any more also leads to the spread of electron directions away from the axes defined by the primary particle direction. The transverse depth unit of a cascade is the Molière radius defined as [108, 109]:

$$R_M = \left(\frac{E_S}{E_c}\right) X_0 \quad (6.11)$$

where  $E_S = \sqrt{\frac{4\pi}{\alpha}} m_e c^2 = 21.2 \text{ MeV}$ . In a material made out of several absorbers, an estimate of the overall Molière radius can be obtained from:

$$\frac{1}{R_M} = \frac{1}{E_S} \sum_i \frac{f_i E_{c,i}}{X_{0,i}} \quad (6.12)$$

The 95% lateral containment for electromagnetic cascades is given by:

$$R(95\%) = 2R_M \quad (6.13)$$

The transversal distribution of the shower depends on the calorimeter depth at which it is measured. At least a two-component structure is needed to describe the transverse profile which displays a narrow central (core) and broad peripheral part. The central part scales as  $R_M$  and is mainly due to multiple scattering of fast electrons responsible for the deposition of most of the incident energy. The peripheral part is mainly due to the propagation of photons. Several two component parameterizations of the transverse shape as a function of the calorimeter depth exist and most of them have a double exponential form.

One of them is provided by the data obtained from a silicon calorimeter [112]. The lateral cascade distributions have been measured using a silicon calorimeter with tungsten and uranium as absorber for incoming electron energies of 2,4,6 GeV. Experimental data have been fitted to radial energy distributions using the radial probability density function

$$F(r) = \frac{1}{N} \frac{\exp[-\frac{\sqrt{r}}{\lambda_1}] + C_{12} \exp[-\frac{r}{\lambda_2}]}{r} \quad (6.14)$$

where  $\lambda_1^2$  and  $\lambda_2$  are in units of  $R_M$ ,  $C_{12}$  is the relative weight of the two components,  $r$  is the radial distance in units of  $R_M$  and  $N$  is coming from usual normalization condition:

$$\int_0^{2\pi} d\phi \int_0^\infty F(r) r dr = 1 \quad (6.15)$$

We will use the following form:

$$f(r) = p f_C(r) + (1-p) f_T(r) = p \frac{2r R_C^2}{(r^2 + R_C^2)^2} + (1-p) \frac{2r R_T^2}{(r^2 + R_T^2)^2} \quad (6.16)$$

with  $0 \leq p \leq 1$ ,  $R_C$  ( $R_T$ ) are medians of the core (tail) component of radial profile and  $p$  is the probability giving relative weight of the core component as proposed by Grindhammer

Table 6.1: Materials and their characteristics as implemented in G4 simulation for first structure in ECAL

material	d [mm]	$\rho[\frac{g}{cm^3}]$	$X_0$ [mm]	Z	A	$E_c[MeV]$
W	1.4	19.3	3.504	74	183.8	8.004
G10	1.2	1.7	162.02	11	21.32	47.273
Si	0.5	2.33	93.676	14	28.09	36.737
fiber	0.8	$1.29 \cdot 10^{-6}$	28516	7.3	14.61	0.0026
effective	3.9	7.75	9.458	67.408	166.868	9.0804

[113]. The spatial energy distribution of the electromagnetic shower is then given by three probability density functions:

$$dE(\vec{r}) = E f(t) dt f(r) dr f(\phi) d\phi \quad (6.17)$$

describing the longitudinal  $f(t)$  (eq.6.8), radial  $f(r)$  and azimuthal  $f(\phi)$  energy distributions, where  $t$  stands for the longitudinal shower depth in units of radiational length,  $r$  is the radial distance from the shower axis in units of Molière radius and  $\phi$  is the azimuthal angle. For consideration of the average profile it is enough to assume a uniform distribution in  $\phi$  i.e.  $f(\phi) = 1/2\pi$ . The choice of the parameterization was driven more by practical than accuracy considerations. The requirement was that the code is still used and supported, possibly even further developed. Parameterization as in [113] was used in past experiments (H1,Zeus), it was implemented in the Geant3 framework, and is implemented in the Geant4 framework [114] and used for accelerated full simulation in CMS thus fully satisfying the requirements. Since we will not use it for simulation but for reconstruction, accuracy requirements are a bit more relaxed and it can easily be exchanged with another if it is not suitable for our application. There is a low energy cutoff at which the parameterization can be used for simulation that is around 800MeV [114]. This is not a problem for the usage in reconstruction as we will see for the low energy region one needs a dedicated and different procedure anyhow.

### Calorimeter parameters

In order to use the mentioned parameterization a detailed knowledge of the materials and their properties is needed. Tables 6.1,6.2,6.3 show lists of materials and their properties as implemented in the detector simulation. Data from the tables were used according to formulae given in appendix C to calculate all needed variables for the computation of the spatial energy distribution eq.6.17 at a given point. Note that data in the tables correspond to the calorimeter in the original TESLA design <sup>4</sup>. Calculation according to the formulae gives the Molière radius for the first ECAL structure as 22.08mm, for the second 13.84mm and 22.98mm for the HCAL. This makes the transversal segmentation around  $\sim 0.5R_M$  in ECAL and  $\sim 0.8R_M$  in HCAL for the cell size of 10mm in ECAL and 30mm in HCAL leaving enough measurement points on the transverse profile if we take into account eq.6.13.

Table. 6.3 is here to remind us that the hadronic part of the calorimeter has a rather good EM resolution ( $20\%/\sqrt{E}$ ) and that methods in the algorithm are also applicable for the location and extraction of the electromagnetic fraction in the hadronic cascade either for reconstruction or for software compensation. For data presented here, no attempt was made to collect possible tails of the electromagnetic shower in the HCAL.

<sup>4</sup>corresponds to LDC00 model in full simulation

Table 6.2: Materials and their characteristics as implemented in G4 simulation for second structure in ECAL

material	d [mm]	$\rho[\frac{g}{cm^3}]$	$X_0$ [mm]	Z	A	$E_c[MeV]$
W	4.2	19.3	3.504	74	183.8	8.004
G10	1.2	1.7	162.02	11	21.32	47.273
Si	0.5	2.33	93.676	14	28.09	36.737
fiber	0.8	$1.29 \cdot 10^{-6}$	28516	7.3	14.61	0.0026
effective	6.7	12.5769	5.53	71.635	177.614	8.4709

Table 6.3: Materials and their characteristics as implemented in G4 simulation for the HCAL

material	d [mm]	$\rho[\frac{g}{cm^3}]$	$X_0$ [mm]	Z	A	$E_c[MeV]$
Fe	20.0	19.3	17.59	26	55.85	20.653
scintillator	5.0	1.7	162.02	11	21.32	47.273
fiber	1.5	$1.29 \cdot 10^{-6}$	28516	7.3	14.61	0.0026
effective	26.5	6.134	23.06	25.318	54.354	21.285

### 6.3 Photon finding algorithm

Since we often hear about an “imaging” calorimeters the basic idea of the algorithm is to use the picture processing methods to extract the needed information. Lets use our EM shower average energy density profile and integrate it over the ECAL layers and rings within layers around the initial photon direction with a width equal to the cell size. This defines the function:

$$f(r, n, d) = \int_{r-d/2}^{r+d/2} \int_n^{n+1} \int_0^{2\pi} dE(\vec{r}) dr dt d\phi \quad (6.18)$$

where r is radius, n layer number and d cell size. If we plot this function with some number of thresholds as in Fig.6.3 we can have estimate of the distribution of energy deposited in cells. We can see that on the basis of this picture in the ideal case we would be able to distinguish how many photons we have (by the number of red zones), and to separate close by photons in some color (second blue shade). The “picture” taken with the calorimeter will be smeared due to the physics (fluctuations in the shower) and due to the finite cell size since the radius is not changing in infinitesimal but finite steps (egual to the cell size). In a highly granular calorimeter as the one proposed for the ILC detector this smearing is small and enough information survives that our idea can be applied. This is the essence of the algorithm. From some initial set of data containing only a monochromatic set of points in space we are painting them according to the deposited energy with some pallet and then trying to distinguish features as one would do by naked eye. As a counter measure to the smearing additional noise reduction procedure is introduced in order to remove ”bad” pixels. This establishes an integrated procedure for both localization of single and separation of close by showers.

#### 6.3.1 Algorithm steps

The algorithm tries to merge two distinct approaches to the reconstruction, one with the predominant use of energy information and second with predominant use of topology information. My personal opinion is that only an optimal balance of this who sides can give you the wanted

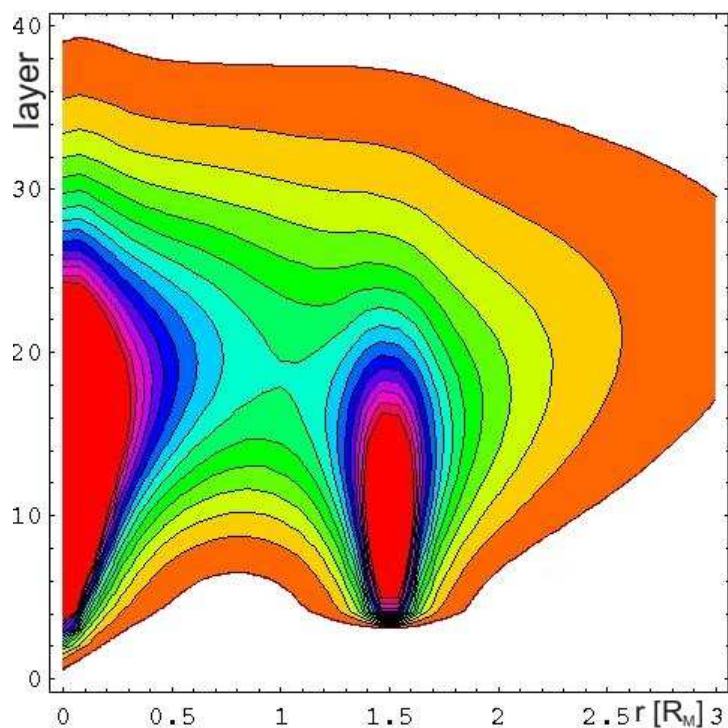


Figure 6.3: Photon profile 10GeV and 4 GeV photon, energy density distribution integrated over layers and rings of cell size width.

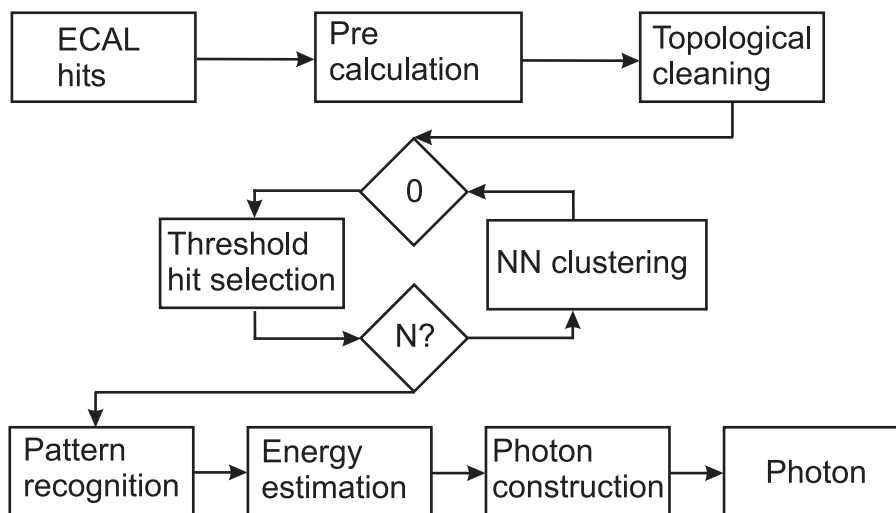


Figure 6.4: General layout of the photon finder algorithm.

performance. Fig. 6.4 shows the basic layout of the algorithm. Now we will go through each step of the algorithm in some detail.

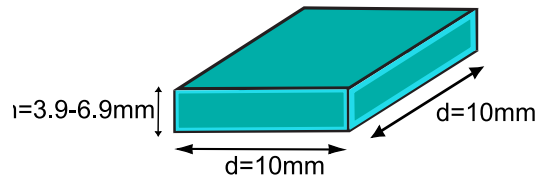


Figure 6.5: Dimensions of the ECAL cell volume, thickness ( $h$ ) depends on the amount of absorber.

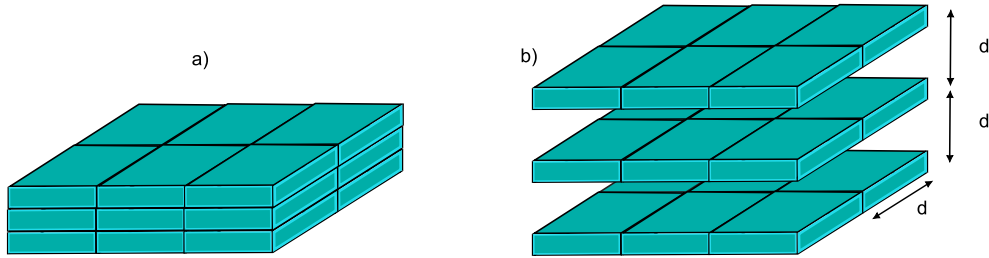


Figure 6.6: Transformation of the cell coordinates to isotropic space a) real cell arrangement b) cell coordinates after transformation, where  $d$  is cell size.

### ECAL hits

The ECAL volume is divided by segmentation (both longitudinal and transversal) into quanta for which we have separate information from the detector - ECAL cells. ECAL cell, as shown in Fig.6.5 for  $1 \times 1\text{ cm}$  transversal segmentation, has a thickness that varies from 3.9-6.9mm in different zones (first or second sampling structure) or in different designs of the ECAL. Note that this is not a cubic volume. Each of these volumes has a unique ID, measured energy (assumed to be in GeV) and coordinate (characteristic point within the cell volume - in the simulation geometrical center of active material). This information stored together, we will call hit. Assuming that proper calibration is performed and that the mentioned information is stored in LCIO hit classes, the treatment of simulated and real data will not differ. At the initial stage calibrated hits together with the information about minimum ionizing particle (MIP) signal size are passed to the algorithm. Information is copied to the internal hit class and amplitudes in units of MIP are calculated and stored.

### Pre-calculation

From the knowledge about the shower development one expects rather compact object without discontinuities arising in the calorimeter, thus the natural choice for collecting hits is a nearest neighbor (NN) type of clustering. For NN clustering one needs to define a metric in which the distance<sup>5</sup> between objects is calculated and the cutoff value for the distance at which we consider two objects to be neighbors. Due to the fact that the cell volume is not a cubic one, a simple Euclidian metric and one cutoff on the physical distance between hits will not work. There are two possible solutions to this problem. One can define a rather complex metric and work in the cell ID space or we can transform the cell coordinates into an isotropic space and use a simple distance measure. Both approaches should give the same result but due to technical reasons transformation was chosen as the preferred solution. The basic requirement

<sup>5</sup>not necessary physical length

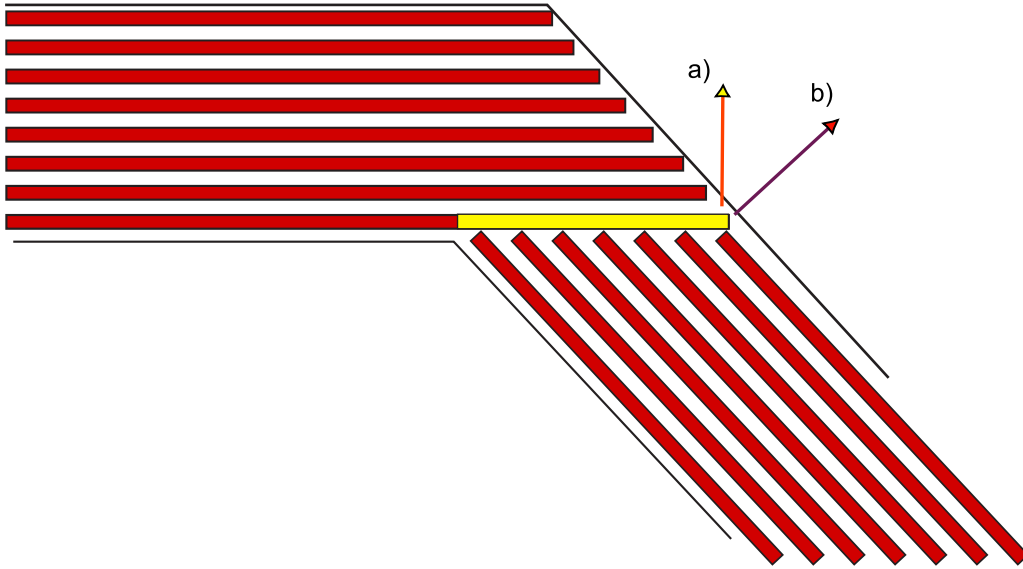


Figure 6.7: Special region in the ECAL geometry due to the mechanical design. Connectivity of hits is preserved by two transformations a and b, that are applied to the special part of first layer (marked yellow).

of such transformation is that it preserves the connectivity that is specially important due to the specific construction of the ECAL. Effectively we are “projecting” hit space to a cubic grid, and thus under neighbor assume any hit that is on any of 26-th vertices around a given point. Fig.6.6 shows effect of the transformation. The second set of hit coordinates is calculated (and stored) by stretching layers apart until they are on the distance equal to the cell size. Once the transformation is performed, a nearest neighbor (NN) algorithm can be called with a simple Euclidian measure. For the calculation of the neighbors speed optimised functions from the ANN library [115] were used, with the distance cut defining the neighborhood  $D = 2d^2 + (d + \delta l)^2$ , where  $d$  is cell size and  $\delta l$  is introduced to account for the relative layers offsets ( $\sim 1mm$ ) but keeping the condition  $D < 4d^2$  so as we do not introduce jumps over the layer. Links to neighbours are stored in internal hit class in order to speed up clustering procedure by skipping the recalculation of the distance. Due to the specific construction of the ECAL, as shown in Fig.6.7 special care needs to be taken in transition regions between modules. This is solved in the way that the hits from yellow region are formally considered twice, once for the module they are belonging to a) and second time by calculating effective layer number for second module b) and performing the transformation with appropriate parameters. The corner part shown repeats itself eight times over the barrel structure and each time the same procedure is applied. Pre-calculation is to some extent time consuming operation but since neighbors are determined at this stage (and stored) no recalculation of the distance is needed for the clustering procedure so that the total computational overhead is minimized. After this stage for each hit we know how many neighbors it has and who they are (links to neighboring hits in form of pointers are kept in internal hit class), thus pre calculation has increased available information for reconstruction.

### Topological cleaning

Now it is possible to benefit from the additional knowledge about the event by cleaning the picture before the crucial step of core localization and identification. By topological cleaning we assume removing hits with less than  $M$  neighbors from the intermediate processing in algorithm<sup>6</sup>. Topological cleaning is introduced from general considerations for algorithm working on full physics events where one would like to clean the picture from the things that are obviously not photons: isolated hits and track segments for which we don't need to consider energy information. Effects of the topological cleaning are shown on Fig.6.8. Only some hits on the surface of the electromagnetic shower are removed and at the same time the muon track is fully erased. This step is not mandatory, and algorithm can work without it. Photon finding in this algorithm is based on recognition of the dense part of the shower i.e. "core" so why would one like to do a separation of hits on the topology? There is a correlation between the energy information and the topological one but this is not the main reason for this approach. Two major reasons for this step are: - due to the Landau distribution of the hit energy on track segments in the calorimeter, hits can have almost arbitrary energy; - the same is true for the neutron hits that are randomly spread around. With topological cleaning these hits are removed from consideration in a natural way and can be passed to other algorithms within the reconstruction for processing. Second by topological cleaning we are smoothing the surface of the shower and reducing the problems with natural fluctuations. The only significant argument against the usage is the problem with low energy photons ( $\leq 0.5\text{GeV}$ ). Not only that such photons have ill defined shape that is hard to recognize with any kind of the procedure, but in a dense calorimeter they start to behave more and more track like i.e their energy density distribution is so contained in a volume comparable with the cell size that there are not enough hits satisfying selection criteria to construct the core. This leads to a drop of the efficiency in this energy range and is not the responsibility of the topological cleaning alone but a result of the rather complex interplay with other algorithm steering parameters (specially minimal number of hits in NN cluster). If one decides to use this step in the algorithm only hits that pass the cut will be used in the following steps until the final photon construction when naturally all the hits<sup>7</sup> are considered.

### Central loop

In order to locate the core parts of electromagnetic showers we will do an energy scan over hits. All the hits still available (all of them if no topological cleaning) are split into  $N$  subsets with the condition  $E_{hit} > T_i$  where  $T_i$  is  $i$ -th threshold (level)  $0 \leq i < N$ . It is obvious that this kind of spiting is not exclusive thus some of the hits will appear in more than one category, and it is exactly what we want for the pattern recognition step. After such splitting NN clustering is performed on each subset (hits are clustered only with the neighbors belonging to a given set). By doing this after finishing  $N$ -loops we have  $M$  (where  $M \leq N$  depending on highest  $\gamma$  energy in the event and chosen parameters of the algorithm) sets of clusters made at different energy levels and this set of clusters is the input information into pattern recognition. On Fig.6.9 all the thresholds used are plotted on top of the hit energy distribution in MIP units for 5GeV photon. The first threshold should be same as the calibration one thus including all available hits.

Why do we need  $N$  levels, and could  $N$  be 1 or 2? In order to answer this question we should look at hit energy distribution for showers from different ends of spectrum. In Fig.6.10 the

<sup>6</sup>central loop and pattern recognition

<sup>7</sup>may not be true if it is used in synergy with other algorithms

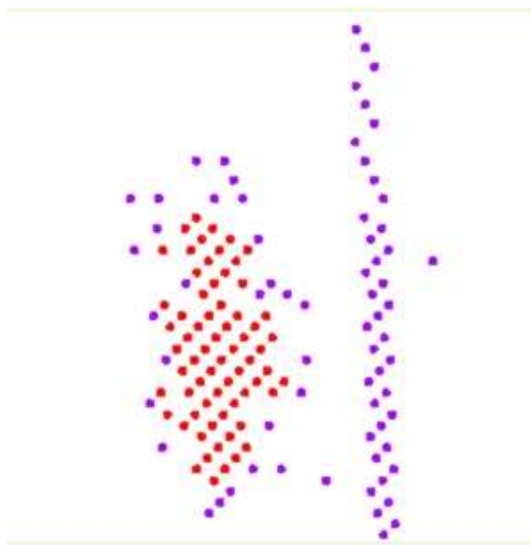


Figure 6.8: Effect of topological cleaning. On the picture are photon and muon close by. In red are hits left after such procedure in blue those removed, cut  $M \leq 4$ .

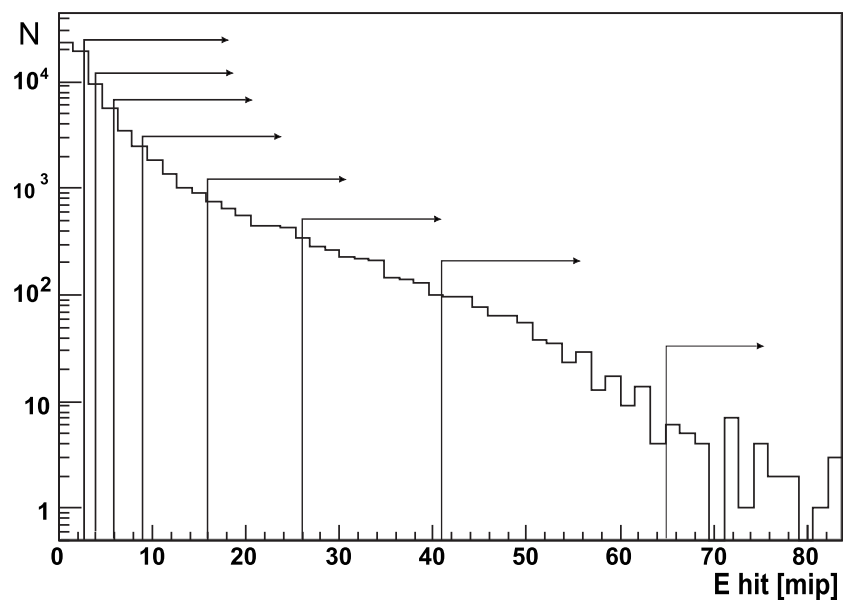


Figure 6.9: Energy distribution for ECAL hits from 5 GeV photon with all default thresholds (except first one).

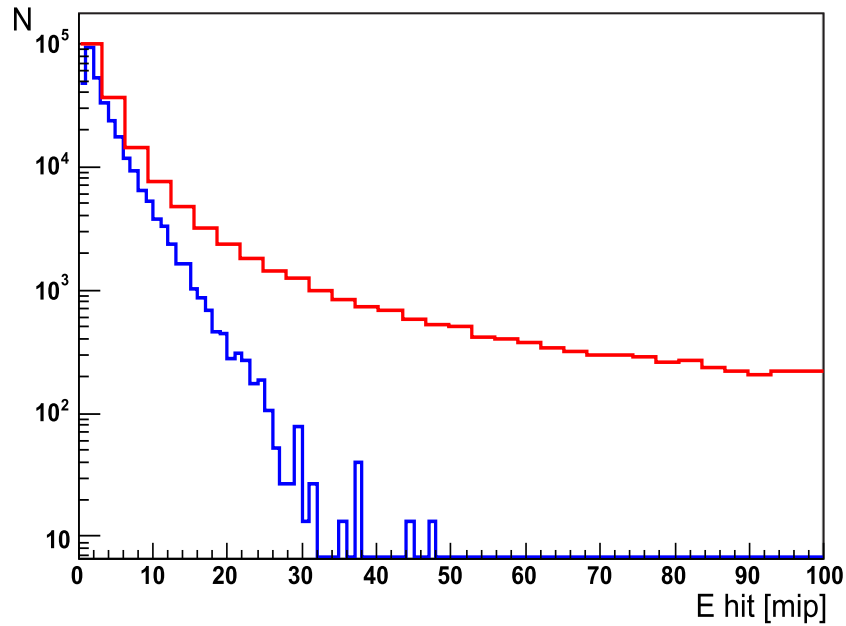


Figure 6.10: Energy distribution for ECAL hits, in blue 1GeV photon in red 20GeV photon. Normalized to maximum.

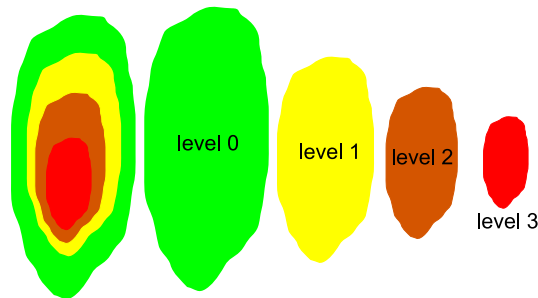


Figure 6.11: Expected pattern after threshold clustering for isolated EM shower.

energy distribution of hits from 1GeV and 20GeV showers is plotted. If we keep in mind that distribution for energies between 1 and 20 GeV will lie between the two curves, and assume two close by photons, it is clear that the separation simply on the basis of the thresholding and clustering would be possible with good efficiency, only for a pair of energies and particular extent of overlap. One or two thresholds is enough if one would use it for image cleaning (that is done by topology in this algorithm) and the core finding by another procedure (peak finding on spherical projection, clustering in  $\theta - \phi$  or another approach). We are not only interested to find in finding bulk electromagnetic showers but also to have good close by shower separation. Note that thresholds are more densely covering lower part of the hit energy spectrum (Fig.6.9) exactly for the reason to have good separation over the full energy range.

### Pattern recognition

This is the step of the procedure where the decision about the number of photon candidates is made and the photon candidates are produced. Initially all lowest level clusters are labeled

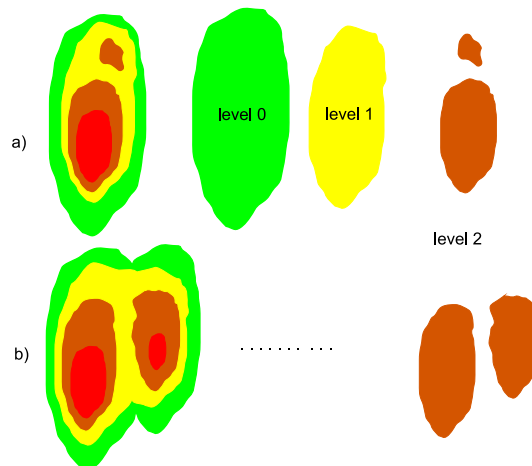


Figure 6.12: Expected patterns after threshold clustering in case of fluctuations a) and two close by photons b).

as photon candidates. What would be the distinctive sign of a single photon? As shown in Fig.6.11 according to our threshold selection and neglecting the fluctuations one would have a repeating structure of clusters in which each level cluster will enclose only one cluster of higher level. If this is the case lowest level cluster is kept as a core of the electromagnetic shower. The lowest level cluster is natural choice since it contains the maximal fraction of the full shower energy and will give the most accurate estimate of the incoming energy in next step.

If at some level  $i+1$  we have 2 or more clusters a decision needs to be made to consider them as two “cores” of electromagnetic shower or one needs to be kept and other discarded. Natural fluctuations of the shower tend to create false cores. Due to the lateral containment of the shower over the small number of cells and NN clustering procedure these ghosts are appearing mostly in the second part of the shower development as in Fig.6.12 a). At the same time we can have two close by photons that are overlapping to some extent so that their separation is achieved only at  $i$ -th level Fig.6.12 b). In the case of two real photons the starting point need not to be at the same calorimeter depth and is exponentially distributed from the face of the calorimeter along the incoming direction. Thus there is an angle between the direction connecting shower centers with respect to the incoming direction. This angle is not 90 degrees (as it would be for same starting point, same incoming energy and no fluctuations) but is on the average significantly larger then the angle for the ghost cores. This gives us a powerful separation criteria. The second separation criteria is distance of two core candidates. For the fake cores NN cluster is most probably split due to the fluctuations in one layer of the calorimeter and in the case of two real photons we have much wider distribution. These differences in behavior are used in a cone cut as on Fig.6.13. A cone with some opening angle (parameter of the algorithm) is constructed from the center of one cluster along the assumed direction of incoming particle. If the center of second cluster is within the cone and distance is small enough this cluster is discarded as a fluctuation as in Fig.6.13 a). If the second cluster on level  $i$  is outside of the cone as in Fig.6.13 b) the initial core is discarded and two new ones are formed.

The performance of this part of the procedure is steered with several parameters for clustering, splitting (initial “core” is deactivated and two new ones emerge), discarding and merging (two cores of the same level are merged and are considered as one further one). The merging

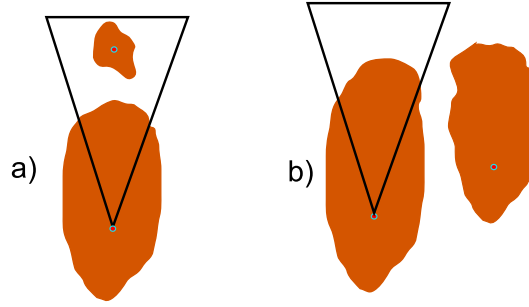


Figure 6.13: Cut based separation used to discriminate between fluctuations in case a) and two close by photons in case b). Triangle represents cut cone.

procedure is a additional correction procedure in order to minimize the software induced errors. Imagine a situation from Fig.6.13 in such a way that left core in the part b) is replaced by part a). Now we have 3 cores at given level, two correct ones and one fake. If two are chosen to be new cores the runaway fraction, third core, is then merged into one of others even thoe is not connected in nearest neighbor meaning. This merging procedure is not affecting the number of cores found but is needed for the next step that is energy estimation. If one would throw away fluctuation fragment we would significantly decrease the accuracy for energy estimation procedure. The result of the pattern recognition step is a set of cores - photon candidates.

### Energy estimation

After pattern recognition we have a set of core clusters i.e. photon candidates. For each of these candidates we need a estimation of the incoming photon energy. Why we need this when calorimeter measures the energy? We need such a step in order to collect the full photon energy (in distant and isolated hits) and to have more accurate photon profile construction. Since the sizes of the photon profile vary logarithmically with energy there is no need for a extremely accurate but still want precise estimator. This step is in a sense calibration procedure. Large samples of photons are passed through the simulation and the algorithm with the modification that energy of clusters at each level is stored. After that incoming energy is parameterized as a function of core energy and threshold level. As one can see from Fig.6.14 linear parameterization of the form

$$E_{\gamma} = a + bE_{core} \quad (6.19)$$

is sufficient for given level. Once this lookup table for given detector is made it's easy to make a function:

$$E_{\gamma} = f(E_{core}^i, i, detector) \quad (6.20)$$

that gives estimation of incoming photon energy, where  $i$  stands for threshold level and detector implies that this parameterization needs to be done for particular choice of detector (sampling, cell size, simulation parameters etc.), and algorithm parameters. Even tho procedure for creation of incoming energy estimation function 6.20 is straight forward it can be lengthy procedure if one would like to cover larger energy range or make several of them for detector optimization purpose.

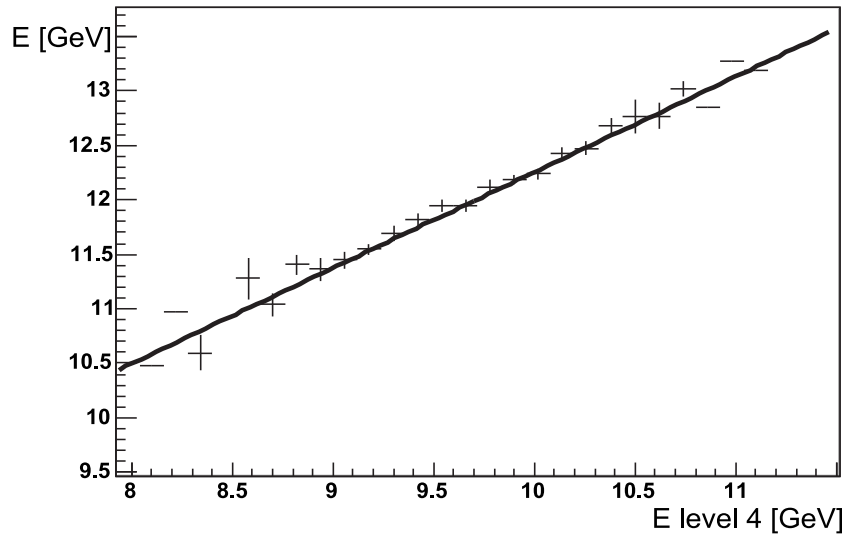


Figure 6.14: Example of the energy estimation fit for 12 GeV photons. On abscise energy of the cluster on level 4, on ordinate energy of true cluster.

### Photon construction

After energy estimation one has all the variables needed to construct a photon on the basis of 3D model. The parameters are energy, direction (one can choose between IP-center of the core or inertia tensor direction) and starting point. At this place topological information can be helpful since one can neglect isolated hits when searching for hit closest to the ECAL face along the chosen direction as an approximation of the starting point. Once all input parameters are calculated it is possible to calculate the energy density for a photon at the position of each hit. Why energy density and not the integral over the cell volume? Due to the complexity of the energy density function for the 3D profile and arbitrary orientation of the cell volume to the direction of the photon one would need a complicated and time consuming numerical integration procedure at this stage without a clear gain. At this stage estimator is needed that will satisfy two conditions: It has the knowledge about the shape (in order no to pick up arbitrary distant hits) and it is proportional to the deposited energy in the cell volume (in order to be used for separation in case of close by  $\gamma(e)$ ). Value of energy density distribution at a hit position is such estimator, first requirement it satisfies automatically. We are making replacement of the kind:

$$\int_{cell} f(r_1, t_1, E_1) dr_1 dt_1 \Rightarrow f(r_1, t_1, E_1) \quad (6.21)$$

that should satisfy:

$$\int_{cell} f(r_1, t_1, E_1) dr_1 dt_1 > \int_{cell} f(r_2, t_2, E_2) dr_2 dt_2 \Leftrightarrow f(r_1, t_1, E_1) > f(r_2, t_2, E_2) \quad (6.22)$$

It can be proven by hand or some mathematical computation package [118] that inequality holds for radial functions of the form that we have in eq.6.16:

$$\frac{Ar}{(r^2 + B)^2} \quad (6.23)$$

if  $r_1 > r_2$ . Full energy density distribution of eq.6.17 is used to calculate “probability” that hit belongs to a given photon candidate. In order to provide user with the full information needed for each spatial point requested value of the estimator and radial distance from the direction is returned. Now we can assign a estimator to each available hit. By available hits we mean all the hits in ECAL irrespective of their topology **if they are not assigned by another procedure**. Good example for this is Fig. 6.8 it means that muon “track” hits in the ECAL are already assigned to the muon and are not subjected to this part of the procedure. In final stage after processing hits with multiple contributions in some way either deterministic (assignment to one or another photon candidate - used in the algorithm at the moment) or weighted ( i.e. energy shearing between the photon candidates with some weight) one should have full set of hits that can be stored in a cluster class of choice. **At this step or any later during reconstruction procedure quality check is needed before final assignment - quality check is left to be performed by user.**

### 6.3.2 Summary of steering parameters

Parameters of the detector as geometry and materials although used in algorithm are not variables since whole calibration procedure for the energy estimation step would need to be redone (material change is changing the shower development and at the same time integrals of photon shower energy density distribution over the cell volume thus energy estimation on the base of the cluster with given threshold and topology characteristic will be affected and in order to preserve reachable accuracy level of such procedure it needs to be repeated). Sequence of tasks would be to adjust the parameters of the algorithm (if not satisfied with the default) using an old calibration and after that redo the calibration for the final data processing. Here is full set of steering parameters for the algorithm as it used for the evaluation of performance that will be presented later. The steering parameters of the algorithm are:

- Topological cleaning threshold - Minimal number of neighbors that hit needs to have in order to be considered within photon candidate search routine.

*Default value*  $M = 4$ .

- Number of threshold levels- number of subsets in which the hits will be divided for internal clustering and pattern recognition. Choice of particular number of levels should be made on expected energy range of photons (electrons), precision of search, amount of work needed for preparation of energy calibration procedure and speed penalty that is acceptable. Number of levels is arbitrary but due to the LCIO Cluster class properties (level of the photon candidate is stored in type bit-field by setting appropriate bit to 1) it's limited on 16 for larger number you would need to do the coding on your own!

*Default value*  $N = 10$

- Threshold levels - particular choice of  $N$  cut levels once  $N$  is determined in previous step (in units of MIP)

*Default value* 0.1, 1.5, 2.5, 4.0, 6.0, 9.0, 16.0, 26.0, 41.0, 65.0

- Minimal cluster size, in number of hits, for 0-th level cluster - As already stated initially all 0-th level clusters are considered as photon candidates thus this parameter affects the initially number of candidates and thus the efficiency of algorithm. Proper value needs to be chosen depending on actual value of topological cleaning parameter.

*Default value* 4

- Minimal cluster size, in number of hits, for i-th level

*Default value* 4

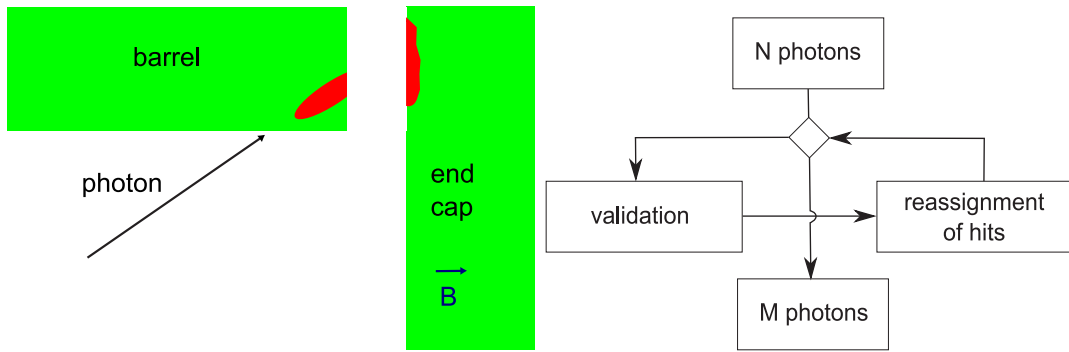


Figure 6.15: Transition region between ECAL barrel and end cap. EM shower distribution is represented with red zones on the left, algorithm for the fake suppression after preliminary photon construction on the right.

- Splitting condition - Cosine of the cone opening angle plus the distance between the splitted clusters (in mm). Plus additional parameter to suppress fluctuation called  $R_{cut}$  that is putting limit on the ratio of hits in next level to the number in previous.

*Default value* 0.9 35mm 0.4

- Energy density threshold - formally energy density function of the 3D photon model has non zero value even outside of the detector since longitudinal and transversal profile functions are normalized on the 0 to infinity range. For practical purpose this is of course nonsense. In order to limit range in which one would try to assign hits to a photon and still collect full energy some cutoff value needs to be chosen. This cut naturally arises from the fact that we have a 0.5MIP calibration threshold thus at some value of energy density it's integral over the cell volume will not reach 0.5MIP energy.

*Default value*  $0.00001 GeV X_0^{-1} R_M^{-1}$

### 6.3.3 Algorithm performance

#### Single photon

For testing algorithm performance single photon events were generated over the larger energy range, with uniform distribution in  $\theta$  and  $\phi$ , using MOKKA LDC00\_02Sc model. In order to have some reference performance values obtained from so far best reconstruction tool Pandora [116][117] were used for comparison. Definition of efficiencies for single photon case is: “Shoot exactly one photon into detector and expect to reconstruct exactly one “. Thus with single photon case we can test proper reconstruction and confirm that usual problem of the general clustering approach - splitting is solved. Due to the possibility of conversion in to the  $e^+e^-$  pair events were selected on the base of true information available from MC simulation. Condition is that endpoint of the photon is located in the ECAL. This condition reduces incoming sample by 20% but assures that we have exactly one photon entering the calorimeter. This cut is applied in all single photon samples.

Transition region of the two major parts of the ECAL (barrel and end cap) is making serious challenge for reconstruction and identification of EM shower. Current implementation in the MOKKA has empty space that will probably be partially or fully filled with material (cables,TPC support). With no or with little material this transition region acts as a magnetic spectrometer dividing neutral and charged part of the EM shower leading to considerable

spatial spread in the second part of the shower that is measured with end cap part as demonstrated in Fig.6.15. In order to isolate these effect one can define 200mm long region within the barrel,(measured from the edges of the barrel) that will be called corner region. On the basis of the Monte Carlo information we can separate (or remove) photons that start to shower within this zone. Dedicated procedure needs to be developed to cover reconstruction in this segment of the detector. Loss of the recognizable and characteristic shape of the EM shower will also make neutral hadron shower separation significantly harder. Effects of the corner region on the reconstruction performance will naturally depend on the angular distribution of the process in question and performance of the software compensation for these effects. In order to determine the true algorithm performance and exclude detector non uniformity effects for photons above 1GeV there was additional event selection cut that excludes the corner region of the ECAL thus giving clean algorithm performance. In order to estimate size of the effect same samples were processed with and without this cut.

As already mentioned quality check is left to be performed by user so that algorithm can be integrated within various frameworks. In order to estimate performance rudimentary correction procedure was developed. This is still not identification procedure in its full meaning! Most of the tools used like neural networks [119] and H matrix [120], or others do not construct cluster but just give the probability i.e. photon ID for cluster created in another procedure. Here we are making conceptual jump from disconnected and sequential procedure to iterative one:

- clustering  $\rightarrow$  particle ID to the integrated and essentially recursive approach to
- clustering  $\rightarrow$  validation  $\rightarrow$  clustering  $\rightarrow$  validation ... until all reconstructed object fit to the desired criteria.

Procedure developed is in fact a fraction of validation step that would contain also proper photon ID. Once the hits are preliminary assigned to the found cores one can check the consistency of the calibration energy and the energy collected in hits. Fakes have low energy and after the assignment of hits less energy then there is to be expected. This feature was used in the procedure sketched on Fig.6.15.

After preliminary assignment of hits to found cores energy of collected hits is calculated. Ratio of the collected energy and the estimated incoming energy from the calibration procedure is made.

$$E_r = \frac{E_{collected}}{E_{incoming}} \quad (6.24)$$

This quantity was used to make logical rejection criteria in the form:

$$if( not (E_r < 0.5 or (E_r < 0.6 and E_{incoming} < 0.6GeV))) \quad (6.25)$$

If condition is satisfied no action is taken. If not preliminary photon candidate is deleted and it's hits are reassigned to remaining photons. Loop is repeated until all the photons are processed and pass the criteria. This leads to reduction of number of reconstructed particles from N to M. In order to demonstrate the effect of this step number of cores i.e. preliminary photons was plotted on the Fig.6.16 and is stated separately in the full result tables in appendix.

In Fig.6.16 and Table 6.4 results for energy range 1-40GeV are presented for full detector. In order to see the impact of the post processing procedure there is additional column labeled "core" that is representing the performance on the level after pattern recognition (without fake suppression). We can see that general clustering approach as expected performs well at low energies and then efficiency drops rather fast due to the splitting of showers into several

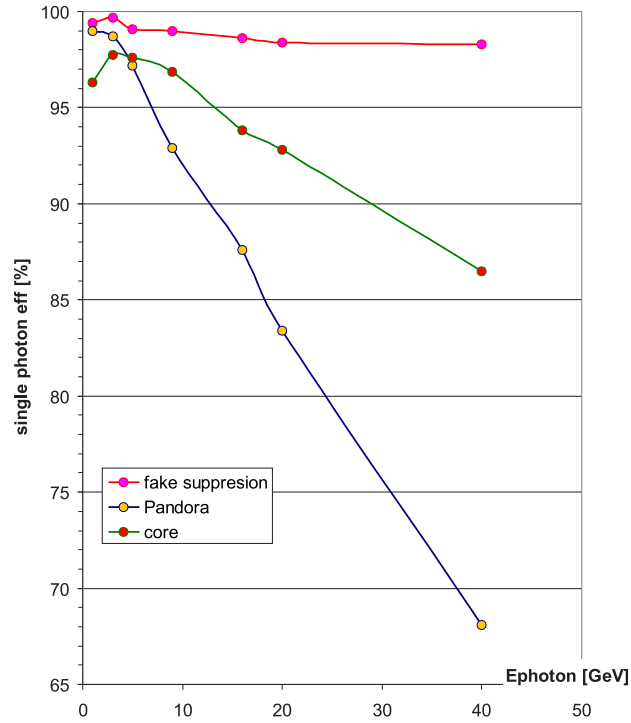


Figure 6.16: Single photon efficiency after core finding (in green), final result after fake suppression (in red) in comparison with Pandora-PFA (in blue).

Table 6.4: Single photon reconstruction efficiencies for single photon events, summary table. Full dataset.

Energy [GeV]	core [%]	algorithm [%]	Pandora-PFA[%]
1.0	96.32	99.4	99.0
3.0	97.76	99.7	98.7
5.0	97.60	99.1	97.2
9.0	96.86	99.0	92.9
16.0	93.80	98.6	87.6
20.0	92.80	98.4	83.4
40.0	86.50	98.3	68.11

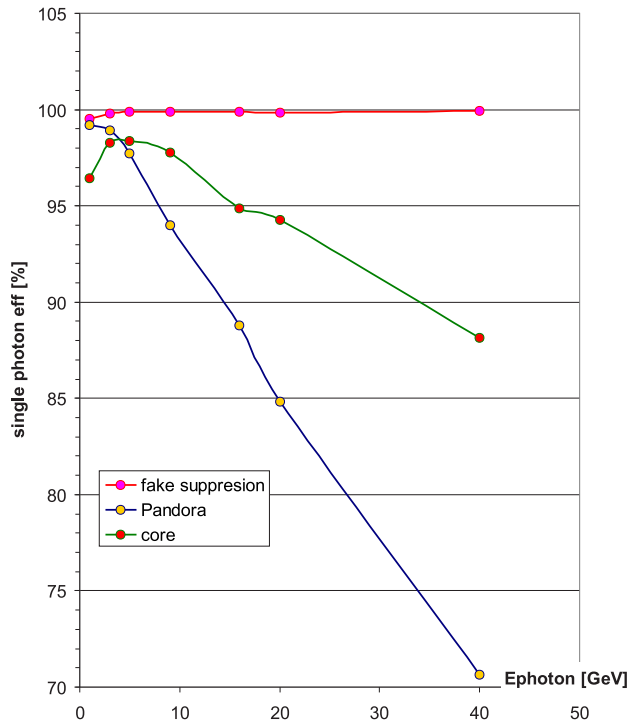


Figure 6.17: Single photon efficiency after core finding (in green), final result after fake suppression (in red) in comparison with Pandora-PFA (in blue) with ECAL corner region excluded.

clusters. Situation at the core finding stage is intermediate one, there is some basic level of fakes but the energy dependence is already much more flat and performance at higher energies is significantly better than with general clustering. After fake suppression final performance is now almost flat and at expected level.

In Fig.6.17 and Table 6.5 are results for the pure reconstruction performance since corner region event were removed from the data sample. Now one can clearly see the linear drop of the simple clustering and flat performance of explained algorithm.

Difference in performance depending on the inclusion of barrel end-cap transition region is demonstrated in Fig.6.18. At lower energies (below 3GeV) effect is almost negligible. This is due to the fact that size of shower in this energy region is small, plus solid angle for the region which needs to be hit in order to produce recognizable signature in both parts of ECAL is infinitesimally small. When we go to the higher energies size of the shower grows, as well as solid angle of the region in which leaking part of the shower from barrel is recognized a photon in the end-cap. This region is represented in almost linear drop in efficiency from 3-20GeV. For 20-40GeV region we have reached situation that none of the incoming photons within this zone is reconstructed as one so the total effect is proportional to the integral of the incoming photon angular distribution over the zone. Performance of both investigated reconstruction approaches is same in this zone and can be shortly described by you shoot one in you get arbitrary number of reconstructed particles at output. This confirms the statement that dedicated procedure need to be developed to deal with this region.

Additional check was made for the performance in the low energy region (below 1GeV). In this region reason for efficiency drop is now pure inefficiency that is to say there is 1 incoming

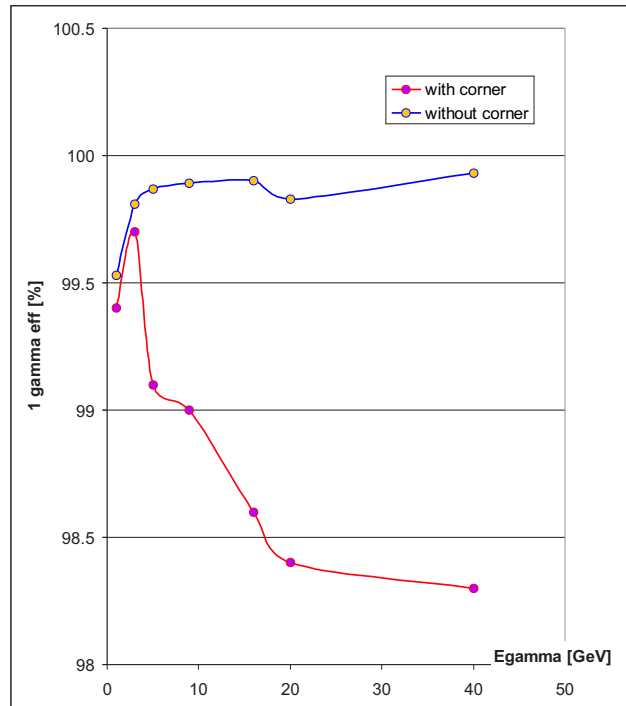


Figure 6.18: Single photon efficiencies for the algorithm for full data set (in red), and with corner region excluded (in blue).

Table 6.5: Single photon reconstruction efficiencies for single photon events, summary table. Without events going to the barrel end-cap transition region

Energy [GeV]	core [%]	algorithm [%]	Pandora-PFA[%]
0.3	65.55	65.18	57.86
0.4	83.86	84.73	77.18
0.5	92.05	94.57	90.17
0.7	95.98	99.00	99.01
0.85	96.12	99.31	99.19
1.0	96.44	99.53	99.19
3.0	98.27	99.81	98.94
5.0	98.37	99.87	97.71
9.0	97.76	99.89	94.01
16.0	94.85	99.90	88.80
20.0	94.27	99.83	84.85
40.0	88.14	99.93	70.63

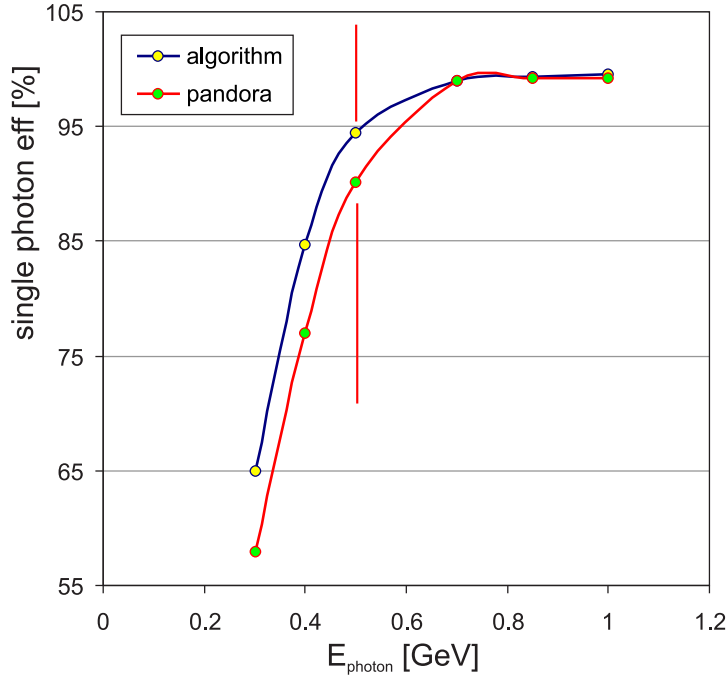


Figure 6.19: Single photon reconstruction efficiencies for low energy photons. Red line marks the 95% efficiency crossing point at 0.5GeV.

photon but there are no reconstructed particles. From the Fig.6.19 and the table 6.5 it is clear that improvement over the straight clustering approach is tiny and that 95% efficiency level is crossed at 0.5GeV. Drop of the efficiency is sharp going to the lower energies and follows one to one direct clustering of Pandora. There are several reasons for such a behavior: low energy photons do not have a well defined shape as those on higher energies, relative fluctuations in number of hits and their distribution is higher and the parameters of the algorithm were unchanged in order to test possibility to cover full energy range with one set of parameters. Any kind of reconstruction will have a hard time making a robust procedure to detect low energy photons and distinguish them from the background coming from other showers in a full physics event. At the present stage, the algorithm does not have satisfactory performance for the energies below 0.5GeV.

### Neutral pions

Neutral pions were also generated in order to test the performance of the algorithm. With pions we can check at the same time proper counting as in the single photon case but also proper separation of close-by photons with different energies. Proper separation of showers will represent itself in the width of the reconstructed mass distribution and pion reconstruction can improve overall PFA reconstruction [121]. Mass can be calculated in the usual way:

$$m_{\gamma\gamma} = \sqrt{2E_{\gamma 1}E_{\gamma 2}(1 - \cos\theta_{\gamma\gamma})} \quad (6.26)$$

$\pi^0$  samples were generated in flat distributions in  $\theta$  and  $\phi$  over the detector. Events were selected according to the MC truth information so that both photons reach the ECAL without conversion. An additional cut was implemented, as in the single photon case (If any of the photons

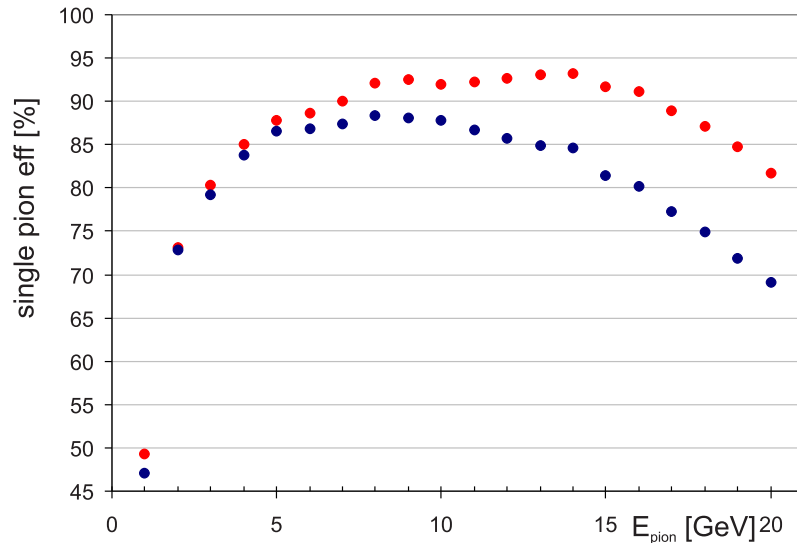


Figure 6.20: Comparison of single pion reconstruction efficiencies for algorithm (red) and Pandora-PFA(blue).

starts to shower within the 200mm from the barrel edge event is not processed), to remove events ending in problematic corner region. Here we introduce another definition of efficiency that is similar to one for the photon case. Efficiency is number of events in which we reconstruct exactly two photons divided by number of events in which we have two photons entering the calorimeter.

According to this definition event samples with  $\pi^0$  kinetic energy from 1 up to 20GeV were tested. Samples contain 10000 events minus those with conversion. Results are summarized in the Fig.6.20 and Table 6.6. First clear interesting point is 1GeV where both tested codes have pure performance that is dominated by the same type of low energy single photon efficiency. With the rise of pion kinetic energy both codes perform better due to the increase of the efficiency for the single photon case. After 5GeV algorithm performance starts to be significantly better then of the Pandora due to the splitting problem of clustering. Going to even higher energies this effect becomes even more prominent. In the same time second effect comes in to the game to reduce the performance drop of the clustering approach. In case of resolved photons splitting leads to the case 2 incoming photons  $\rightarrow$  3 reconstructed dropping the performance, in case of unresolved photons we have “1” incoming  $\rightarrow$  2 reconstructed formally boosting the reconstruction efficiency. This effect can be clearly seen on the mass distribution constructed from two reconstructed photons since it produces mass far from nominal. Algorithm performance is almost flat in the region 8-15GeV and then starts to drop due to the increased fraction of unresolvable cases.

In case two photons were reconstructed mass is calculated and stored in histogram without any additional cuts. In Fig.6.21 we can see negative effect of the cluster splitting on the  $\pi^0$  distribution as produced by Pandora. At the same time we can see almost perfect Gaussian shape with minimal number of events far from the nominal mass as a result of explained algorithm. Mass distribution histograms were fitted with simple Gaussian distribution and the width of the distribution was extracted.

Results are summarized in Fig.6.22 and Table.6.7. Explanation for the behavior is rather

Table 6.6: Pion reconstruction efficiencies for single pion events, summary table. Without events going to the barrel end-cap transition region

$\pi^0$ Energy [GeV]	algorithm [%]	Pandora-PFA [%]
1.0	49.24	47.14
2.0	73.15	72.86
3.0	80.36	79.19
4.0	85.06	83.82
5.0	87.83	86.57
6.0	88.68	86.83
7.0	89.97	87.39
8.0	92.13	88.37
9.0	92.55	88.10
10.0	92.03	87.81
11.0	92.23	86.65
12.0	92.69	85.67
13.0	93.01	84.93
14.0	93.21	84.58
15.0	91.74	81.49
16.0	91.11	80.16
17.0	88.98	77.26
18.0	87.08	74.93
19.0	84.76	71.92
20.0	81.75	69.17

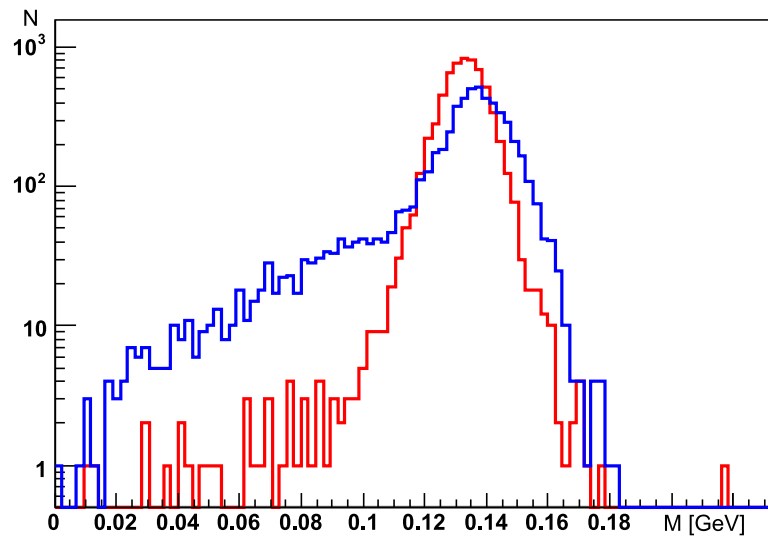


Figure 6.21: Comparison of  $\pi^0$  mass distribution for algorithm in red, and Pandora-PFA in blue. Kinetic energy of pions is 18 GeV.

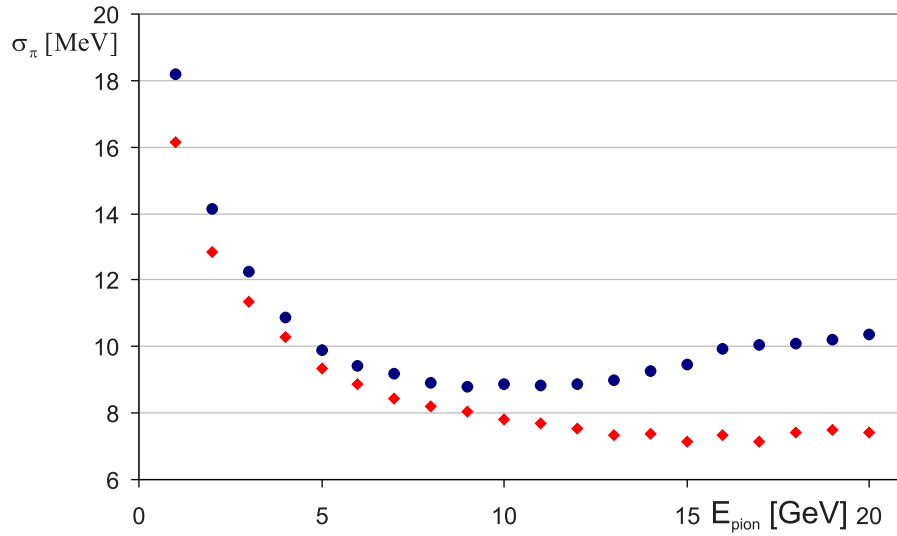


Figure 6.22: Comparison of width of reconstructed pion mass distribution for algorithm (red squares) and Pandora-PFA (blue circles).

Table 6.7: Width of the reconstructed pion mass distribution, summary table. Without events going to the barrel end-cap transition region

$\pi^0$ Energy [GeV]	algorithm [MeV]	Pandora-PFA[MeV]
1.0	16.16	18.20
2.0	12.85	14.16
3.0	11.34	12.27
4.0	10.29	10.86
5.0	9.25	9.90
6.0	8.88	9.41
7.0	8.46	9.18
8.0	8.22	8.91
9.0	8.05	8.77
10.0	7.81	8.88
11.0	7.68	8.85
12.0	7.55	8.86
13.0	7.35	8.98
14.0	7.36	9.25
15.0	7.14	9.46
16.0	7.35	9.94
17.0	7.16	10.06
18.0	7.41	10.08
19.0	7.49	10.22
20.0	7.42	10.36

E [GeV]	$N_{evt}$	Time [s]	Per evt. [ms]
1	8311	14	1.7
3	8276	19	2.3
5	8299	22	2.6
9	8316	29	3.5
16	4135	20	4.8
20	4171	22	5.3
40	4124	33	8.0

Table 6.8: Total processing time for single photon events.

simple on the low energy side where width of the mass is dominated by the resolution of the calorimeter and not by precision of the direction determination. Algorithm shows better performance over the clustering due to the capability of collecting the distant hits thus making equal nominal and effective resolution of the calorimeter. Due to the dual structure of the calorimeter energy dependence is not simple square root behavior and it determines behavior in transition region. On high energy side angular error starts to dominate it's clear that algorithm performance is as expected. Behavior of clustering approach can be explained with additional contribution to the error probably coming from the errors in separation of close by showers. Neglecting efficiency difference algorithm reconstructs  $\pi^0$  with mass distribution that is 10 – 30% better than one of the Pandora allowing for much better starting point for possible constrained fitting that could improve reconstruction performance even further .

### Speed

Since we are confident the code is doing that what is meant to do performance of the code in terms of needed CPU is also important issue. Maybe not for playing around with samples of the 1000 events ( corresponding to processes with fb cross section and  $1ab^{-1}$ ) but it will be of large importance for dominant processes with  $\sim 10^6$  events for same luminosity. Performance was estimated on the single photon events and is shown in Table.6.3.3 and on Fig.6.23. Measured time includes full processing from start of the program till end of program execution thus incorporating LCIO file reading, calorimeter hits digitization and algorithm execution time on P4 at 3GHz. As we can see from Fig.6.23 processing time is linear with energy with slope of  $0.15msGeV^{-1}$  that indicates that reading time is still dominating the performance and that algorithm does not introduce any significant time consumption.

### 6.3.4 Conclusion

New algorithm for reconstruction of electromagnetic showers is established. Already in this early stage of development it shows significant improvement over the general clustering algorithms. Significant advantage of the approach is that cluster construction and knowledge about it's shape and behavior are integrated in one procedure. This integration is important for the performance since it allows the auto correction inside the algorithm i.e. reassignment of the hits and possible drop of the hypothesis not leaving the user in the done deal situation as in cluster plus ID approach. Current performance has still not reached desired level in low energy region but there is a huge room for improvements, not by changing the structure of the algorithm but refining the procedures used at each of those steps. Fig.6.24 is the best summary for this chapter since it demonstrates the combined performance of the ILC detector and reconstruction software in comparison with the ALEPH detector plus reconstruction

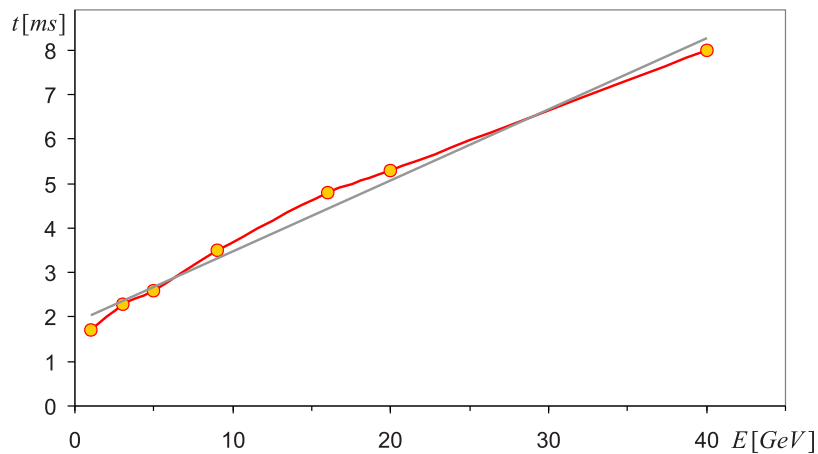


Figure 6.23: Speed of the algorithm per photon of given energy. Connected dots are data points from table 6.3.3, gray line represents linear fit.

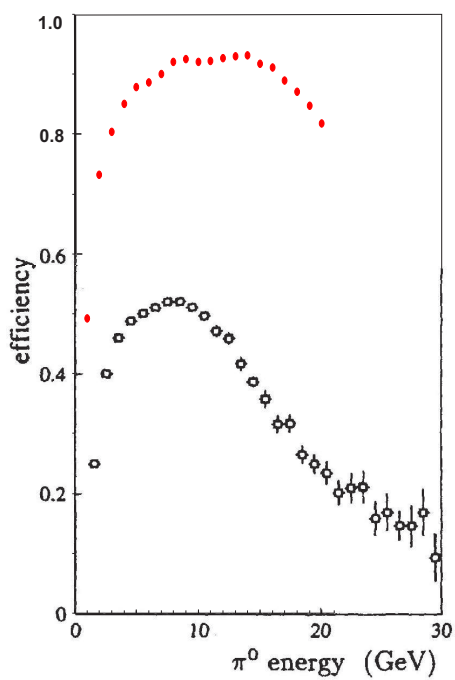


Figure 6.24:  $\pi^0$  reconstruction efficiency for ALEPH (black circles) and ILC detector with proposed algorithm (red dots).

[122] for  $\pi^0$ . I hope that this picture will bring us at least a permill closer to having the real detector.



## Chapter 7

# Summary and conclusions

The title of the theses is: "Measurement of quartic couplings at ILC and study of novel particle flow algorithms". What I want to stress is that altho large work has been done this theses is not presenting measurement at ILC. It presents results for given set of ILC machine and detector parameters that were considered as realistic at one point in time. Basic assumptions for the measurement of quartic couplings are:

- Both electron and positron polarizations are available
- Collected luminosity is at least  $1ab^{-1}$  at highest reachable energy (1TeV)
- Jet energy resolution is  $30\%/\sqrt{E}$
- Hermeticity and tracker coverage is as supposed for the TESLA TDR detector
- SM cross sections are calculated with precision at the percent level

Accepting those assumptions, and fighting that they do not stay only assumptions, it is possible to say that :

- direct measurement of quartic couplings to the theoretically favored precision ( $\sim 1$ ) is possible (if isospin conservation is assumed)
- Under equal time sharing between  $e^+e^-$  and  $e^-e^-$  channels weak boson scattering processes are giving equivalent results (if isospin conservation is assumed).
- Prospects for large indirect reach from this measurement are bleak even under most favorable conditions, specially in scalar and vector channel.
- If one accepts assumptions stated above as realistic one the precision is limited only with statistics.

Jet energy resolution goal is mostly driven with weak boson scattering processes, so we have studied in some details what are the contributions to the final performance and how it can be reached. On of the major ingredients in acheaving this goal is accurate separation of the showers in ECAL. New approach to reconstruction in ECAL, that fully exploits power of the calorimeter designed for particle flow was presented. It shows superior performance (with efficiency above 99% ) in the EM shower energy range from 0.5-40GeV with no energy dependence of the performance, with possible further improvements it refreshes the hope to reach desired performance.

# Appendix A

## Theory addons

### Notation

Gamma matrices

$$\gamma^0 = \begin{pmatrix} 0 & 1 \\ 1 & 0 \end{pmatrix} \quad (\text{A.1})$$

$$\gamma^i = \begin{pmatrix} 0 & -\sigma_i \\ \sigma_i & 0 \end{pmatrix} \quad (\text{A.2})$$

$$\gamma^5 = i\gamma^0\gamma^1\gamma^2\gamma^3 = \begin{pmatrix} 1 & 0 \\ 0 & -1 \end{pmatrix} \quad (\text{A.3})$$

$$\gamma_5^\dagger = \gamma_5 \quad (\gamma_5)^2 = I \quad \{\gamma^5, \gamma^i\} = 0 \quad (\text{A.4})$$

projection operators

$$P_R = \frac{1 + \gamma^5}{2} \quad \text{and} \quad P_L = \frac{1 - \gamma^5}{2} \quad (\text{A.5})$$

$$\bar{\psi}_L = (L\psi)^\dagger \gamma_0 = \psi^\dagger L^\dagger \gamma_0 = \psi^\dagger \gamma_0 R = \bar{\psi} R \quad (\text{A.6})$$

$$\bar{\psi}_R = \bar{\psi} L \quad (\text{A.7})$$

Fermion mass term mixes right- and left-handed fermion components,

$$\bar{\psi}\psi = \bar{\psi}_R\psi_L + \bar{\psi}_L\psi_R \quad (\text{A.8})$$

Pauli matrices

$$\tau_1 = \begin{pmatrix} 0 & 1 \\ 1 & 0 \end{pmatrix} \quad \tau_2 = \begin{pmatrix} 0 & -i \\ i & 0 \end{pmatrix} \quad \tau_3 = \begin{pmatrix} 1 & 0 \\ 0 & -1 \end{pmatrix} \quad (\text{A.9})$$

with commutation relations

$$[\tau_i, \tau_j] = i\epsilon_{ijk} \tau_k \quad (\text{A.10})$$

Lepton number conservation - neutrino masses equal 0 ! parity violation (pseudo scalar  $\mathbf{J}_i \mathbf{P}_e$ )

$$\partial_\mu \equiv \frac{\partial}{\partial x^\mu} \equiv \left( \frac{\partial}{\partial x^0}, \nabla \right) \quad (\text{A.11})$$

$$\partial^\mu \equiv \frac{\partial}{\partial x_\mu} \equiv \left( \frac{\partial}{\partial x_0}, -\nabla \right) \quad (\text{A.12})$$

$$\partial_\mu \partial^\mu = \frac{\partial^2}{t^2} = \square^2 \quad (\text{A.13})$$

d'Alembertian operator. The condition that an equation be Lorentz covariant is that on the two sides of the equation the un repeated upper and lower indices must balance separately and repeated indices must appear once as an upper and once as lower index.

### A.0.5 groups

Any set of elements satisfying :

- closure under group multiplication
- associative law
- existence of an identity element
- existence of an inverse element

is called group. If group multiplication is commutative the group is called Abelian group. If the group operations are defined by a continuous parameter and the derivative with respect to that parameter can be performed ( operations of the group are analytic functions on parameter space i.e. all order derivatives are well defined) the group is usually called Lie group. For general Lie groups the generators are closed under commutation, meaning that commutator of any two of them yields a linear combination of them

$$[G_i, G_j] = ic_{ijk}G_k \quad (\text{A.14})$$

where  $G_i$  are generators, the  $c_{ijk}$  are set of numbers called the structure constants ( hermiticity of the generators requires that they must be real). The generators form a closed Lie algebra eq.A.14. The elements or operation of a group can be represented by matrices, with the group multiplication represented by matrix multiplication of the corresponding matrices. Altho each element of the group is represented by a matrix the matrices corresponding to different elements need not be different. If each element of the group corresponds to a different matrix then the representation is called faithful representation. Every group has one-dimensional representation  $M_i = 1$  for all i, this representation is called trivial representation. Labeling. If matrices obey

$$R^T R = R R^T = I \quad R^{-1} = R^T \quad (\text{A.15})$$

group is called orthogonal and labeled with capital O. If all of them have additional property that their determinant are +1 they are called special with additional label S. if matrices are unitary the group has additional label U. Matrix is in a reduced form if it is in block diagonal form. Particles correspond to irreducible representation of groups i.e. representations whose matrices cannot all be put into block diagonal form by the same choice of basis set. Property of Abelian groups is that all of their irreducible representations are one-dimensional. Sum of diagonal elements of the diagonalize generators must be 0??

### Lagrangian

Scalar field.

$$\mathcal{L} = \frac{1}{2} \phi \partial_\mu \phi - \frac{1}{2} m^2 \phi^2 \quad (\text{A.16})$$

leads to

$$(\square^2 + m^2)\phi = 0 \quad (\text{A.17})$$

Spin 1/2 field .

$$\mathcal{L} = i\bar{\psi}\gamma^\mu\partial_\mu\psi - m\bar{\psi}\psi \quad (\text{A.18})$$

$$(i\gamma^\mu\partial_\mu - m)\psi = 0 \quad (\text{A.19})$$

Massless vector field

$$\mathcal{L} = -\frac{1}{4}F_{\mu\nu}F^{\mu\nu} - j^\mu A_\mu \quad (\text{A.20})$$

### Noether's theorem

Fundamental result that has connected symmetry and interaction is the Noether's theorem [27]. If an action is invariant under some group of transformations (symmetry), then there exist one or more conserved quantities (constants of motion) which are associated to these transformations. Let us assume that Lagrangian of the physical system is invariant under some set of continuous transformations

$$\phi_i(x) \rightarrow \phi'_i(x) = \phi_i(x) + \epsilon\delta_i\phi_i(x) + O(\epsilon^2) \quad (\text{A.21})$$

i.e.

$$\mathcal{L}[\phi_i(x), \partial_\mu\phi_i(x)] = \mathcal{L}[\phi'_i(x), \partial_\mu\phi'_i(x)] \quad (\text{A.22})$$

leads to

$$\delta_\epsilon\mathcal{L} = 0 = \sum_i \left( \left[ \frac{\partial\mathcal{L}}{\partial\phi_i} - \partial^\mu \left( \frac{\partial\mathcal{L}}{\partial(\partial^\mu\phi_i)} \right) \right] \delta_\epsilon\phi_i + \partial^\mu \left[ \frac{\partial\mathcal{L}}{\partial(\partial^\mu\phi_i)} \delta_\epsilon\phi_i \right] \right) \quad (\text{A.23})$$

If the fields satisfy Euler-Lagrange equations of motion

$$\frac{\partial\mathcal{L}}{\partial\phi_i} - \partial^\mu \left[ \frac{\partial\mathcal{L}}{\partial(\partial^\mu\phi_i)} \right] = 0 \quad (\text{A.24})$$

the first term in eq.A.23 is zero, therefore system have conserved current

$$\mathcal{J}_\mu \equiv \sum_i \frac{\partial\mathcal{L}}{\partial(\partial^\mu\phi_i)} \delta_\epsilon\phi_i \quad \text{and} \quad \partial^\mu\mathcal{J}_\mu = 0 \quad (\text{A.25})$$

That allowed to construct a conserved charge

$$\mathcal{Q} \equiv \int d^3x \mathcal{J}^0 \quad (\text{A.26})$$

In this way logical direction from symmetries to conservation laws thus selection rules observed in the nature correspond to the dynamical symmetries of the Lagrangian.

### A.0.6 Goldstone theorem

When an exact continuous global symmetry is spontaneously broken, i.e. it is not a symmetry of the physical vacuum, the theory contains one massless scalar particle for each broken generator of the original symmetry group. Let us consider a Lagrangian of  $N_G$  real scalar fields  $\phi$ , belonging to a  $N_G$  dimensional vector  $\Phi$ ,

$$\mathcal{L} = \frac{1}{2}\partial_\mu\Phi\partial^\mu\Phi - V(\Phi) \quad (\text{A.27})$$

Suppose that  $G$  is a continuous group that lets the Lagrangian invariant and that  $\Phi$  transforms like

$$\delta\Phi = -i\alpha^a T^a \Phi \quad (\text{A.28})$$

Since the potential is invariant under  $G$ , we have

$$\delta V(\Phi) = \frac{\partial V(\Phi)}{\partial\phi_i} \delta\phi_i = -i \frac{\partial V(\Phi)}{\partial\phi_i} \alpha^a (T^a)_{ij} \phi_j = 0 \quad (\text{A.29})$$

Gauge parameters  $\alpha^a$  are arbitrary (and nonzero), and we have  $N_G$  equations

$$\frac{\partial V(\Phi)}{\partial\phi_i} \alpha^a (T^a)_{ij} \phi_j = 0 \quad (\text{A.30})$$

for  $a = 1, \dots, N_G$ . Taking another derivative of eq.A.30, we obtain

$$\frac{\partial^2 V(\Phi)}{\partial\phi_k \partial\phi_i} (T^a)_{ij} \phi_j + \frac{\partial V(\Phi)}{\partial\phi_i} (T^a)_{ik} = 0 \quad (\text{A.31})$$

If we evaluate this result at the vacuum state  $\Phi = \Phi_0$ , which minimizes the potential, we get

$$\left. \frac{\partial^2 V(\Phi)}{\partial\phi_k \partial\phi_i} \right|_{\Phi=\Phi_0} (T^a)_{ij} \phi_j^0 = 0 \quad (\text{A.32})$$

or in terms of mass matrix,

$$M_{ki}^2 (T^a)_{ij} \phi_j^0 = 0 \quad (\text{A.33})$$

If, after we choose a ground state, sub-group  $g$  of  $G$ , with dimension  $n_g$ , remains symmetry of the vacuum, then for each generator of  $g$

$$(T^a)_{ij} \phi_j^0 = 0 \quad \text{for } a = 1, \dots, n_g < N_G \quad (\text{A.34})$$

while for the  $(N_G - n_g)$  generators that break the symmetry,

$$(T^a)_{ij} \phi_j^0 \neq 0 \quad \text{for } a = n_g + 1, \dots, N_G \quad (\text{A.35})$$

Taking into account eq.A.33 it is clear that there are  $(N_G - n_g)$  zero eigenvalues of the mass matrix i.e. massless Goldstone bosons.

## Appendix B

# Pflow factorization

This chapter contains results for  $e^+e^-Z, W^+W^-, t\bar{t}$  at center of mass energy 500GeV in tables B.1,B.2,B.3 and 1TeV in tables B.4,B.5,B.6. Generation of events is done by Pythia with following flags:

$$\begin{aligned} MSTJ(22) &= 3 \\ PARJ(72) &= 300.0D0 \end{aligned} \tag{B.1}$$

that are forcing decay of all unstable particles to the sphere with radius 300mm around IP. As already mentioned only hadronic decay channels were considered by turning of leptonic decay channels by setting  $MDME(i,1) = 0$  ; where  $i = \{206, 207, 208\}$  for W , and  $i = \{182, \dots, 187\}$  for Z. Initial state radiation is turned off with:

$$\begin{aligned} MSTP(61) &= 0 \\ MSTP(11) &= 0 \end{aligned} \tag{B.2}$$

Exclusive  $t\bar{t}$  production is regulated with opening or closing chnannels  $\gamma \rightarrow t\bar{t}$  (mdme(167,1)) and  $Z \rightarrow t\bar{t}$  (mdme(167,1)). Generated subprocesses are Z production msub(1) and W pair produciton msub(25). Conditions under which results in the table are extracted are explained in 5.1.3. For 1TeV effect of mass assignment is shown combined.

<i>Effect</i>	$\sigma[GeV]_{separate}$	$\sigma[GeV]_{joined}$	$\sigma[GeV]_{total} (\%/\sqrt{E})$	$\sigma\% \text{ of total}$
$E_\nu$	0.75	0.75	0.75 (3.35)	2.44
$\theta^\circ < 5$	1.80	1.95	1.95 (8.72)	14.03
$P_t < 0.36GeV$	1.96	2.76	2.76 (12.36)	16.63
$\sigma_{HCAL}$	3.04	3.04	4.11 (18.38)	40.01
$\sigma_{ECAL}$	2.20	3.75	4.66 (20.84)	20.95
$M_{neutral}$	1.03	3.89	4.77 (21.35)	4.59
$M_{charged}$	0.56	3.94	4.81 (21.49)	1.36

Table B.1: Contributions to the width of reconstructed mass distribution from different sources for  $q\bar{q}$  events at 500GeV. Column joined means that PFA and non PFA contributions were summed sequentially. Total means that all the contributions were summed. In last colum partial contribution of each effect to the total width is expressed in percent.

<i>Effect</i>	$\sigma[\text{GeV}]_{\text{separate}}$	$\sigma[\text{GeV}]_{\text{joined}}$	$\sigma[\text{GeV}]_{\text{total}} (\%/\sqrt{E})$	$\sigma\%$ of total
$E_\nu$	0.70	0.70	0.70 ( 3.1)	1.50
$\theta^\circ < 5$	2.73	2.82	2.82 (12.6)	22.8
$P_t < 0.36\text{GeV}$	1.36	3.13	3.13 (14.0)	5.65
$\sigma_{\text{HCAL}}$	4.10	4.10	5.16 (23.1)	51.4
$\sigma_{\text{ECAL}}$	2.17	4.64	5.60 (25.0)	14.4
$M_{\text{neutral}}$	1.02	4.75	5.69 (25.4)	3.18
$M_{\text{charged}}$	0.60	4.79	5.72 (25.6)	1.10

Table B.2: Contributions to the width of reconstructed mass distribution from different sources for  $W^+W^-$  events at 500GeV. Column joined means that PFA and non PFA contributions were summed sequentially. Total means that all the contributions were summed. In last column partial contribution of each effect to the total width is expressed in percent.

<i>Effect</i>	$\sigma[\text{GeV}]_{\text{separate}}$	$\sigma[\text{GeV}]_{\text{joined}}$	$\sigma[\text{GeV}]_{\text{total}} (\%/\sqrt{E})$	$\sigma\%$ of total
$E_\nu$	1.37	1.37	1.37 ( 6.13)	6.65
$\theta^\circ < 5$	1.48	2.02	2.02 (9.02)	7.77
$P_t < 0.36\text{GeV}$	2.23	3.01	3.01 (13.45)	17.76
$\sigma_{\text{HCAL}}$	3.93	3.93	4.95 (22.13)	54.79
$\sigma_{\text{ECAL}}$	1.40	4.17	5.14 (23.00)	6.95
$M_{\text{neutral}}$	1.12	4.32	5.26 (23.53)	4.45
$M_{\text{charged}}$	0.70	4.38	5.31 (23.73)	1.74

Table B.3: Contributions to the width of reconstructed mass distribution from different sources for  $t\bar{t}$  events at 500GeV. Column joined means that PFA and non PFA contributions were summed sequentially. Total means that all the contributions were summed. In last column partial contribution of each effect to the total width is expressed in percent.

<i>Effect</i>	$\sigma[\text{GeV}]_{\text{separate}}$	$\sigma[\text{GeV}]_{\text{joined}}$	$\sigma[\text{GeV}]_{\text{total}} (\%/\sqrt{E})$	$\sigma\%$ of total
$E_\nu$	1.92	1.92	1.92 (6.07)	7.03
$\theta^\circ < 5$	0.98	2.16	2.16 (9.13)	1.83
$P_t < 0.36\text{GeV}$	2.18	3.07	3.07 (9.70)	9.07
$\sigma_{\text{ECAL}}$	2.31	2.31	3.84 (12.14)	10.18
$\sigma_{\text{HCAL}}$	5.91	3.35	7.05 (22.29)	66.63
$M_{\text{ch+neutr.}}$	1.68	6.56	7.24 (22.91)	5.38

Table B.4: Contributions to the width of reconstructed mass distribution from different sources for  $q\bar{q}$  events at 1TeV. Column joined means that PFA and non PFA contributions were summed sequentially. Total means that all the contributions were summed. In last column partial contribution of each effect to the total width is expressed in percent.

<i>Effect</i>	$\sigma[\text{GeV}]_{\text{separate}}$	$\sigma[\text{GeV}]_{\text{joined}}$	$\sigma[\text{GeV}]_{\text{total}} (\%/\sqrt{E})$	$\sigma\%$ of total
$E_\nu$	1.93	1.93	1.93 (6.10)	5.41
$\theta^\circ < 5$	4.14	4.57	4.57 (14.44)	24.88
$P_t < 0.36\text{GeV}$	2.50	5.21	5.21 (16.48)	9.07
$\sigma_{\text{ECAL}}$	1.84	1.84	5.53 (17.47)	4.91
$\sigma_{\text{HCAL}}$	5.82	3.03	8.03 (25.38)	49.17
$M_{\text{ch+neutr.}}$	2.10	6.46	8.30 (26.23)	6.40

Table B.5: Contributions to the width of reconstructed mass distribution from different sources for  $W^+W^-$  events at 1TeV. Column joined means that PFA and non PFA contributions were summed sequentially. Total means that all the contributions were summed. In last column partial contribution of each effect to the total width is expressed in percent.

<i>Effect</i>	$\sigma[\text{GeV}]_{\text{separate}}$	$\sigma[\text{GeV}]_{\text{joined}}$	$\sigma[\text{GeV}]_{\text{total}} (\%/\sqrt{E})$	$\sigma\%$ of total
$E_\nu$	4.17	4.17	4.17 (13.19)	21.18
$\theta^\circ < 5$	3.13	5.21	5.21 (16.49)	11.94
$P_t < 0.36\text{GeV}$	3.81	6.46	6.46 (20.43)	17.68
$\sigma_{\text{ECAL}}$	1.97	1.97	6.75 (21.36)	4.73
$\sigma_{\text{HCAL}}$	5.87	3.12	8.95 (28.30)	41.98
$M_{\text{ch+neutr.}}$	1.41	6.56	9.06 (28.65)	2.42

Table B.6: Contributions to the width of reconstructed mass distribution from different sources for  $t\bar{t}$  events at 1TeV. Column joined means that PFA and non PFA contributions were summed sequentially. Total means that all the contributions were summed. In last column partial contribution of each effect to the total width is expressed in percent.

## Appendix C

# Summary of the formulae for photon shower parameterization

### C.1 Homogeneous media

#### C.1.1 Average longitudinal profiles

$$T_{hom} = \ln y - 0.858 \quad (\text{C.1})$$

$$\alpha_{hom} = 0.21 + (0.492 + 2.38/Z) \ln y \quad (\text{C.2})$$

#### C.1.2 Average radial profiles

$$R_{C,hom}(\tau) = z_1 + z_2 \tau \quad (\text{C.3})$$

$$R_{T,hom}(\tau) = k_1 \left( \exp(k_3(\tau - k_2)) + \exp(k_4(\tau - k_2)) \right) \quad (\text{C.4})$$

$$p_{hom}(\tau) = p_1 \exp \left( \frac{p_2 - \tau}{p_3} - \exp \left( \frac{p_2 - \tau}{p_3} \right) \right) \quad (\text{C.5})$$

$$\begin{aligned} z_1 &= 0.0251 + 0.00319 \ln E \\ z_2 &= 0.1162 - 0.000381Z \\ k_1 &= 0.659 - 0.00309Z \\ k_2 &= 0.645 \\ k_3 &= -2.59 \\ k_4 &= 0.3585 + 0.0421 \ln E \\ p_1 &= 0.401 - 0.00094Z \\ p_2 &= 0.401 + 0.00187Z \\ p_3 &= 1.313 - 0.0686 \ln E \end{aligned} \quad (\text{C.6})$$

## C.2 Sampling calorimeter

### C.2.1 Material and geometry parameters

$$\begin{aligned}
\omega_i &= \frac{\rho_i d_i}{\sum_j \rho_j d_j} \\
Z_{eff} &= \sum_i \omega_i Z_i \\
A_{eff} &= \sum_i \omega_i A_i \\
\frac{1}{X_{0,eff}} &= \sum_i \frac{\omega_i}{X_{0,i}} \\
\frac{1}{R_{M,eff}} &= \frac{1}{E_s} \sum_i \frac{\omega_i E_{c,i}}{X_{0,i}} \quad (E_s = 21.2 \text{ MeV}) \\
E_{c,eff} &= X_{0,eff} \sum_i \frac{\omega_i E_{c,i}}{X_{0,i}} \\
F_S &= \frac{X_{0,eff}}{d_a + d_p} \\
\hat{e} &= \frac{1}{1 + 0.0007(Z_p - Z_a)}
\end{aligned} \tag{C.7}$$

### C.2.2 Average longitudinal profiles

$$T_{sam} = T_{hom} - 0.59F_S^{-1} - 0.53(1 - \hat{e}) \tag{C.8}$$

$$\alpha_{sam} = \alpha_{hom} - 0.444F_S^{-1} \tag{C.9}$$

### C.2.3 Average radial profiles

$$R_{C,sam} = R_{C,hom} - 0.0203(1 - \hat{e}) + 0.00397F_S^{-1} \exp(-\tau) \tag{C.10}$$

$$R_{T,sam} = R_{T,hom} - 0.14(1 - \hat{e}) - 0.495F_S^{-1} \exp(-\tau) \tag{C.11}$$

$$p_{sam} = p_{hom} + (1 + \hat{e})(0.348 - 0.642F_S^{-1} \exp(-(\tau - 1)^2)) \tag{C.12}$$

# Bibliography

- [1] M.Battaglia, The International Linear Collider, hep-ex:0705.3997v1 , 28.05.2007
- [2] Parameters Subcommittee of the International Linear Collider Steering Committee, Parameters for the Linear Collider 30.09.2003.
- [3] Parameters Subcommittee of the International Linear Collider Steering Committee, Parameters for the Linear Collider, 20.11.2006.
- [4] ITRP Recommendation, September 2004.  
[http://www.fnal.gov/directorate/icfa/ITRP\\_Report\\_Final.pdf](http://www.fnal.gov/directorate/icfa/ITRP_Report_Final.pdf)
- [5] ILC Global Desing Effort and World Wide Study, “International Linear Collider Reference Design Report”, August 2007.
- [6] T.Behnke et al.“TESLA: The superconducting electron positron linear collider with an integrated X-ray laser laboratory. Technical design report. Part 4. A Detector for TESLA”,DESY-01-011
- [7] T.Behnke, G.Blair, K.Mönig and M.Pohl, BRAHMS Version 1.00 a Monte Carlo Program for Detector at a 800GeV Linar Collider (1998),  
<http://www.hep.ph.rhbnc.ac.uk/blair/detsim/brahms.html>
- [8] Detector Outline Document for Large Detector Concept, final version, july 2006. Prepared by the LDC group for the Reference Design Report of the International Linear Collider.  
<http://www.ilcldc.org/>
- [9] MOKKA: a GEANT4 based full detector simulation for the ILDC.  
<http://polwww.in2p3.fr/MOKKA>
- [10] The SiD concept group, T.Abe at al. SiD Detector Outline Document  
<http://hepuchicago.edu/oreglia/documents/dod>
- [11] GLD Concept Study Group, “GLD Detector Outline Document” arXiv:physics/0607154
- [12] F.Sauli, “GEM: A new concept for electron amplification in gas detectors”, Nuclear Instruments and Methods A 386, p531 1997.
- [13] Y.Giomataris, P.Rebourgaerd, J.P.Robert and G.Charpak, “MICROMEAS: A high-granularity position-sensitive gasous detector for high particle-flux environments, Nuclear Instruments and Methods A 376 (1996) 29.
- [14] T.Behnke et al. Track Reconstruction Efficency, LC note LC-DET 2007-029.
- [15] Jean-Claud Brient,Advantages and drawbacks for Silicon based ECAL, Snowmass 2005

- 
- [16] P.Krstonosic, Track to DOD detector, presented at ECFA software and Physics simulation meeting 16.08.06
- [17] M.Piccolo private communication.
- [18] A.Stahl,K.Büßer, LC-DET-2004-034.
- [19] H.Vidou, presentation at LDC meeting , Vienna 2005.
- [20] ILC Global Design Effort and World Wide Study Groups, International Linear Collider Reference Design Report Volume 4 Detector, august 2007.
- [21] G.Kane, Modern Elementary Particle Physics, Addison-Wesley 1987.
- [22] W.E.Burcham M.Jobes, Nuclear and Particle Physics, Longman Scientific Technical 1994.
- [23] S.F.Novaes, Standard Model: An Introduction, hep-ph/0001283v1
- [24] W.Buchmüller, C.L. modeling, Field Theory and Standard Model, hep-ph609184v1
- [25] A.Pich, The Standard Model of Electroweak Interactions, hep-ph7054264v1
- [26] A. Salam , J.C. Ward , Phys.Lett. 13, 168 (1964)
- [27] <http://arxiv.org/pdf/physics/0503066>
- [28] J.Goldstone, Nuovo Cim. 19, 154 (1961)
- [29] Y.Nambu , Phys.Rev.Lett 4, 380(1962)
- [30] W. Pauli , Open Letter to all radioactive persons 1930, English translation, Physics Today 31, 27(1978)
- [31] W. Pauli , Septieme Consiel de Physique, Solvay (Gauthier-Villars Paris 1934) p.324
- [32] E.Fermi Z.Phys. 88,161(1934) , Nuovo Cim 11,1(1934)
- [33] G.Gamow and E.Teller Phys.Rev. 49, 895(1936)
- [34] B.Pontecorvo Phys.Rev. 72, 246(1947)
- [35] W. Heisenberg , Z.Physics 77, 1 (1932)
- [36] R. Utiyama , Phys. Rev. 101, 1597 (1956)
- [37] J.Schwinger, Ann. Phys. 2, 407 (1957)
- [38] R.P. Feynmann , M. Gell-Mann , Phys.Rev. 109, 193 (1958)
- [39] R.E. Marshak, E.C.G. Sudarshan, Phys.Rev 109, 1860 (1958)
- [40] J.J. Sakurai, Nuovo Cim. 7, 649 (1958)
- [41] S.A. Bludmann , Nuovo Cim. 9, 433 (1958)
- [42] J. Leite Lopes , Nucl. Phys. 8, 234 (1958)
- [43] S.L. Glashow , Nucl.Phys. 22, 579(1961)

- 
- [44] S.Weinberg , Phys.Rev.Lett. 19, 1264(1967)
- [45] A.Salam , “Elementary Particle Theory”,The Nobel Symposium no 8, Almqvist and Wiksell, Stockholm 1968, p367.
- [46] G.’t Hooft , Nucl. Phys. B33, 173 (1971) and B35 , 167 (1971)
- [47] C.S. Wu, E. Ambler, R.W. Haywood, D.D. Hoppes and R.P. Hudson, Phys. Rev. 105,1413(1957)
- [48] M. Goldhaber, L. Grodzins and A.W. Sunayr, Phys. Rev. 109, 1015(1958)
- [49] R.L. Garwin, L.M. Lederman and M. Weinrich, Phys.Rev. 105, 1415(1957)
- [50] M.T. Burgy, V.E. Krohn, T.B. Novey, G.R. Ringo and V.A. Telegdi, Phys. Rev. 110, 1214(1958)
- [51] S.S. Gerstein and Ya.B. Zel’dovitch, Soviet Phys JETP 2, 579 (1956)
- [52] C.P Burgess and D. London, Phys.Rev. D 48, 4337(1993)
- [53] E.S. Abers and B.W.Lee, Phys.Rep. 9, 1(1973)
- [54] W. Kilian , Electroweak Symmetry Breaking The Bottom-Up Approach, Springer, 2003.
- [55] A. Dobado, A.Gomez-Nicola, A.L.Maroto and J.R.Pelaez, Effective Lagrangians for Standard Model, Springer 1997.
- [56] P.W. Higgs, Phys. Lett. 12, 132(1964)
- [57] F.Englert and R.Brout, Phys.Rev.Lett 13, 321(1964)
- [58] G.S. Guralnik, C.R.Hagen and T.W.B.Kibble, Phys.Rev.Lett 13, 585(1964)
- [59] G.Moortgat-Pick et. al, The role of polarized positrons and electrons in revealing fundamental interactions at the Linear Collider, DESY 05-059
- [60] S.Wolfram , Mathematica book, Cambridge University press
- [61] W.Kilian, WHIZARD 1.26,A generic Monte Carlo integration and event generation package for multi-particle processes,LC-TOOL-2001-039 ,2001
- [62] T.Ohl, O’Mega: An Optimizing Matrix Element Generator, Proceedings of the Workshop on Advanced Computing and Analysis Technics in Physics Research, Fermilab, October 2000, IKDA 2000/30, hep-ph/0011243
- [63] M.Pohl, H.J.Schreiber, SIMDET V4.,A parametric Monte Carlo for a TESLA Detector, DESY 02-061,May 2002
- [64] F.James, MINUIT Function Minimization and Error Analysis, Version 94.1, CERN Program Library Long Writeup D506
- [65] M.Duda, Studien zur Systematik der W-Massen-Bestimmung, diplomarbeit, RWTH Aachen, December 2003
- [66] J.P. Ochoa Ricoux, Optimal Pairing algorithm for 4 and 5 jet events at lep. L3 Note 2786, 31.10.2002

- [67] S.Moretti,L.Lönnblad, T.Sjöstrand , New and Old Jet Clustering Algorithms for Electron-Positron Events hep-ph 9804296v1
- [68] S.M.X. Hansen, D.J.Jackson, R.Hawkings and C.J.S.Damerell, Flavour Tagging Studies for the TESLA Linear Collider, LC-PHSM-2001-024, 2001 <http://www.desy.de/~lcnotes>
- [69] T.Kuhl private communicaiton
- [70] D.J.Jackson, A topological vertex reconstruction algorithm for hadronic jets, SLAC-PUB-7215, December 1996
- [71] T. Sjöstrand, P. Eden, C. Friberg, L. Lonnblad, G. Miu, S. Mrenna and E. Norrbin,PYTHIA V6.221, Computer Physics Commun. 135 (2001) 238
- [72] E.Kouznetsova A.Drugakov private communicaiton.
- [73] W.Menges, A sudy of charged current triple gauge couplings at TESLA, LC-PHSM-2001-022
- [74] J.Sekaric, Studies of Gauge Boson Production with a  $\gamma\gamma$ -Collider at TESLA, DESY-THESES-2005-042
- [75] Lucas Tailor ,”Perfromance of the L3 Detector” L3Note 2132, july 1997
- [76] O.Adriani et al.”Hadron Calorimetry in L3” , Nuclear Instruments and Methods in Physics Research A 302 , 53=62 (1991)
- [77] Satoshi Mihara and Satoru Yamashita, “MT 3.00 a new algorithm to calculate energy flow base on MT package”, OPAL TN575 november 1998
- [78] V.Morgunov, Calorimeter Energy Calibration usign the energy conservation law. LCWS 2006.
- [79] C.Castanier, P.Gay, P.Lutz and J.Orloff. Higgs selfcoupling measurement in e+e- collisions at center-of-mass energy of 500GeV. hep-ex/0101028, 2001.
- [80] T.Barklow, Higgs Self Coupling Errors Versus Jet Energy Resolution,presented at Silicon Detector Workshow October 26-28, 2006. [http://www.slac.stanford.edu/~timb/sid/slac\\_oct\\_2006/hhz.pdf](http://www.slac.stanford.edu/~timb/sid/slac_oct_2006/hhz.pdf)
- [81] T.Barklow, Physics Impact of Detector Performance,presented at LCWS , 2005 <http://www-conf.slac.stanford.edu/lcws05/program/talk/18mar2005.ppt>
- [82] J.C.Brient, Measurement of the Higgs decay into  $WW^*$  at future e+e- linear colliders. LC-PHSM-2004-002 <http://www.desy.de/~lcnotes> .
- [83] M.Kobel, R.Chierici, S.Rosati. Strong electroweak symmetry breaking signals in WW scattering at TESLA. LC-PHSM-2001-038 <http://www.desy.de/~lcnotes> .
- [84] A.Raspereza, LCWS2006 Workshop, march 2006
- [85] S.Magill,S.Kuhlman , LC HCAL Absorber (SS vs W) and P-Flow Performance (Scintillator vs RPC) Comparisons, LCWS05,17 March 2005 [http://www-conf.slac.stanford.edu/lcsim05/lcws05\\_talks/050321/Magill.pdf](http://www-conf.slac.stanford.edu/lcsim05/lcws05_talks/050321/Magill.pdf)

- 
- [86] S.Yamamoto, Status of PFA study Jet Energy Resolution Studies using Cheated PFA, GLD meeting , 25 May 2005 <http://ilcphys.kek.jp/meeting/lcdds/archives/2005-05-25/20050525GLDmeeting.pdf>
- [87] R.Casell, Angular dependence of digital RPC HCAL response to neutral hadrons, 13.10.2005
- [88] TESLA TDR, part IV , page IV-71
- [89] F.Gaede, T.Behnke, N.Graf and T.Johnson “LCIO- Persitensy framework for linear collider simulation studies”, LC-TOOL-2003-053 or arXiv:physics/0306114v1
- [90] P.M.S. Blackett and G.P.S Occhianlini, Proc.R.Soc. A 139, 609 (1933)
- [91] P.M.S. Blackett, G.P.S Occhianlini and J.Chadwick Proc.R.Soc. A 144, 235 (1933)
- [92] J.H.Bhabha and W.Heitler, Proc.R.Soc. A 159, 432 (1936)
- [93] J.F.Carlson and J.R. Oppenheimer, Phys.Rev. 51, 220 (1936)
- [94] B.Rossi and K.Greisen, Rev.Mod.Phys. 13, 240 (1941)
- [95] I.Tamm and S.Belenky, Phys.Rev. 70, 660 (1946)
- [96] W.R. Leo, Techniques for Nuclear and Particle Physics Experiments, Springer, New York
- [97] W.M.Yoo,et al. Reivew of Particle Physics (chapter Passage of particles through matter), Journal of Physics G33, 1 (2006)
- [98] C.Leroy and P.G. Rancoita, Rep.Prog.Phys. 63, 505 (2000)
- [99] Y.S.Tsai Rev.Mod.Phys. 46, 815 (1974)
- [100] R.Wigmans nad M.T.Zeyrek, NIM A485, 385(2002)
- [101] R.L.Ford W.R.Nelson The EGS code system: computer program for the MOnTe calro simulation of electromagnetic cascade showers (version 3) , SLAC Report SLAC-210, 1978.
- [102] W.R.Nelson, H.Hiriyama and D.W.O Rogers, The EGS4 code system, SLAC-265 1985.
- [103] H.Hirayama et al. The EGS5 Code System, Stanford Linear Accelerator Center Report SLAC-R-730, 2005
- [104] W.R. Nelson, C. Field Comparison of EGS5 simulaitons with experiment NIM A 572, 1083 (2007)
- [105] B.Rossi, High Energy Particles, Prentice Hall inc. 1952
- [106] M.J.Berger and S.M.Seltzer, “Tables of Energy Losses and Ranges of Electrons and Positrons”, NASA Report ,NASA-SP-2012, 1964
- [107] E.Longo nad I.Sestili, NIM 128, 283(1975)
- [108] W.R.Nelson, T.M.Jenkins, R.C.McCall and J.K.Cobb, Phys.Rev. 149, 201(1966)
- [109] G.Bathow et al., Nucl. Phys. B20, 592 (1970)

- 
- [110] Walter R. Nelson, Theodore M. Jenkins, Richard C. McCall, and Joseph K. Cobb ,  
“Electron-Induced Cascade Showers in Copper and Lead at 1 GeV”, Phys. Rev. 149, 201  
- 208 (1966)
- [111] G. Bathow et al.,”Measurement of the longitudinal and lateral development of electro-  
magnetic cascades in lead, copper and aluminum at 6GeV”, Nuclear Physics B 20 , 592  
(1970)
- [112] G.Ferri et al. (SICAPO Collaboration), NIM A 273,
- [113] G. Grindhammer and S.Peters, “The Parametrized Simulation of Electromagnetic  
Shower in Homogeneous and Sampling Calorimeters” , arXiv:hep-ex/0001020v1
- [114] J.Weng, E.Barberio and A.Waugh, “Fast shower parametrization for electromagnetic  
cascades”, November 2005.
- [115] D.Mount and S.Arya, ANN: Approximate Nearest Neighbors (library) v 1.1 ,  
<http://www.cs.umd.edu/~mount/ANN>
- [116] M.Thomson, Progress with Particle Flow Calorimetry, arXiv: physics.ins-det 0607261v1  
and 0709.1360v1
- [117] PandoraPFA , <http://www.hep.by.cam.ac.uk/~thomson/pandoraPFA>
- [118] Mathematica4 and Mathematica5 , <http://www.wolfram.com>
- [119] Y.Pei, Photon Identificaiton usign a Neural Network , L3 note 1564, 1994
- [120] G.W.Wilson, Updates on Photon ID using a Longitudianl H-Matrix, 03.04.2007
- [121] G.W.Wilson, Impact of  $\pi^0$  Reconstruction on PFA and Neutral hadron TOF possibili-  
ties. LCWS07
- [122] D.Buskulic at al. Performance of the ALEPH detector at LEP, Nuclear Instruments and  
Methods in Physics Research A 360, 481-506 (1995)
- [123] P.Abreu at al. Performance of the DELPHI detector , Nuclear Instruments and Methods  
in Physics Research A 378, 57-100 (1996)